geotechnics

MDPI

Review

Shear Strength Criteria for Clean Rock Joints: Representation and Comparison of Different Failure Criteria

Mahsa Mahdavirad [1,*], Mahdiyeh Seifaddini [1], Ali Saeidi [1,*], Jean-François Noël [2], Mahdi Salimi [3] and Meghdad Payan [4]

[1] Department of Applied Sciences, Université du Québec à Chicoutimi, Saguenay, QC G7H 2B1, Canada
[2] Sécurité des Barrages et Infrastructures, Hydro-Québec, Montréal, QC H2L 4P5, Canada
[3] Department of Civil Engineering, Faculty of Engineering, University of Guilan, Rasht 4199613776, Iran
[4] UGent Geotechnical Institute (UGGI), Department of Civil Engineering, Ghent University, Technologiepark 68, 9052 Ghent, Belgium
* Correspondence: mahsa.mahdavirad1@uqac.ca (M.M.); asaeidi@uqac.ca (A.S.)

Abstract

Shear strength along clean rock joints is fundamental to the design and safety of slopes, underground excavations, and dam foundations. However, predictions can vary considerably because available shear-strength criteria rely on different assumptions regarding roughness, dilation, scale effects, boundary conditions, and parameter determination. This review first synthesizes the main factors controlling peak shear strength, including joint characteristics, stress state, loading and boundary conditions, and hydrological effects. It then examines the principal parameters used to characterize joint roughness and the main methods available for their measurement and estimation. Building on this foundation, the reviewed shear-strength criteria are organized into seven conceptual families, including linear frictional models, 2D asperity- and dilation-based models, empirical JRC–JCS criteria, constitutive joint models, 3D morphology-based criteria, transitional/degradation-based models, and machine-learning/data-driven approaches. The review is complemented by an applied case study based on direct-shear testing from the Romaine-IV hydroelectric project. The dataset includes 20 specimens tested under multiple normal-stress stages and represents anorthositic and gabbroic rocks with varying degrees of weathering and alteration. The Mohr–Coulomb, Patton, and Barton–Bandis criteria are compared with the measured shear-strength envelopes to examine their behaviour under a common project setting. Particular attention is given to differences in parameter requirements and to the influence of JCS on the Barton–Bandis predictions. The sensitivity analysis highlights the importance of selecting JCS values that are consistent with the actual condition of the joint wall, especially where weathering or mineralogical alteration is present. The case study is intended as a site-specific engineering comparison rather than a general ranking of the three criteria. More broadly, the review shows that the practical applicability of a shear-strength criterion depends not only on its theoretical formulation, but also on the availability, quality, and consistency of the parameters required for its implementation. The proposed classification framework and applied comparison provide practical guidance for criterion selection while identifying areas where improved parameter characterization, standardized testing, and broader multi-site validation are still needed.

Keywords: shear strength criteria; joint roughness; scale effects; Romaine-IV hydropower; 3D surface morphology; roughness anisotropy

Check for updates

Academic Editor: Xin Huang

Received: 28 July 2026
Revised: 10 September 2026
Accepted: 30 September 2026
Published: 2 November 2026

Copyright: © 2026 by the authors. Licensee MDPI, Basel, Switzerland. This article is an open access article distributed under the terms and conditions of the Creative Commons Attribution (CC BY) license.

1. Introduction

Rock masses are inherently discontinuous. Joints, fractures, bedding planes, and faults often govern deformation and failure in slopes, tunnels, caverns, and dam foundations because they provide preferential planes for sliding and separation. Therefore, estimating shear strength along discontinuities remains a core requirement in rock engineering design and risk assessment [1,2].

Despite decades of research, predicting joint shear strength is not straightforward. Measured peak resistance depends not only on the intact rock strength, but also on discontinuity-specific mechanisms such as asperity interlocking and dilation, progressive damage of asperities, and changes in real contact area during shearing. These mechanisms are strongly influenced by the stress path and boundary condition (e.g., constant normal load (CNL) versus constrained normal displacement), making the apparent shear-strength envelope sensitive to the test setup as well as the joint morphology [3,4].

A central difficulty is that the controlling parameters are multi-factor and scale-dependent [5,6]. The effective parameters commonly reported to influence peak shear strength include joint roughness, surface matching, discontinuity size/scale, infilling or alteration products, stress state, boundary/loading conditions such as normal stress level [1,2,7], normal stiffness or constraint, shear rate, and cyclic or progressive loading and hydrological conditions that alter effective stress and modify frictional and damage processes. Because different criteria encode different subsets of these effects (explicitly or implicitly), two models applied to the same joint can yield materially different predictions, even when calibrated to the same dataset.

Among these factors, roughness and quantification occupy a particularly influential role because roughness controls dilation, peak friction mobilization, and the evolution of contact during shear. Classical engineering practice has long relied on the joint roughness coefficient (JRC) concept introduced by Barton and Choubey and further developed within the JRC–joint wall compressive strength (JCS) framework [5,8]. In parallel, many studies sought objective alternatives to subjective chart matching, including 2D profile statistics (e.g., Z_2 and related measures) [9] and later 3D morphology descriptors intended to capture anisotropy and the directional nature of shearing. Examples include morphology-based approaches that link strength to distributions of apparent dip, contact ratios, or asperity geometry [10,11]. More recent contributions have continued to refine multi-scale and stress-dependent roughness concepts and embed them into strength prediction, reflecting the expanding availability of high-resolution surface measurements [12–14]. Recent investigations have further expanded this landscape by considering environmental factors such as thermal treatment [15] and by employing numerical modeling to capture rate-dependent and stress-dependent behavior at the microscale [16], illustrating the broadening scope of joint shear research.

The diversity of roughness descriptors connects directly to the diversity of shear-strength criteria. Commonly used formulations can be grouped into several conceptual families. These include linear frictional envelopes (Mohr–Coulomb-type); asperity/dilation-based bilinear descriptions [17], empirical JRC–JCS models [5,7,8] with scale and parameter adaptations, mechanics- or energy-informed frameworks that explicitly represent interlocking and progressive damage [18,19], and modern morphology-explicit or data-driven/hybrid models that aim to leverage 3D surface data and multi-parameter inference [10,11,13,20]. Each family provides a different balance between interpretability, parameter demands, and portability between laboratory and field scales.

Several review and perspective papers have synthesized important subsets of the joint-shear literature, but typically with a component-specific scope. For example, broad discussions of discontinuity shear behavior and practical challenges are provided by Barton and Hencher and Richards [21,22], while boundary-condition-specific syntheses focus on constant normal stiffness (CNS) and its implications for dilation and peak strength [23]. Other reviews concentrate on parameter selection and calibration issues for widely used empirical criteria [24], the comparative performance of classical formulations on selected test datasets [25,26], and the expanding toolbox of 2D/3D roughness descriptors and measurement approaches [27]. More recently, direct shear testing practice, especially multi-stage procedures and boundary-condition effects, has been critically examined to highlight how test protocols can influence the interpretation and transferability of shear parameters [28].

Despite these contributions, two practical gaps remain persistent. First, prior reviews rarely treat roughness as an explicit translation problem. In other words, they do not explain how a roughness quantity obtained from a specific measurement workflow (e.g., profile-based statistics, areal 3D scanning, fractal/multi-scale descriptors, or field photogrammetry/LiDAR) can be mapped consistently into the parameter requirements of different criterion families. Second, comparative discussions are commonly qualitative or rely on heterogeneous datasets and assumptions, which limits their value for engineering selection and benchmarking. Reviewers also explicitly expect clearer positioning against earlier reviews and stronger, more current coverage (e.g., 3D characterization and data-driven models).

Accordingly, the present review is designed as a critical, state-of-the-art synthesis with an applied benchmark, structured in two linked parts. The first part synthesizes the effective parameters controlling peak shear strength, and then provides a focused, measurement-oriented review of roughness descriptors and their principal estimation routes. The second part classifies shear-strength criteria into conceptual families, emphasizing assumptions, data requirements, and domains of applicability. The synthesis is then complemented by an applied case study using the Romaine-IV direct-shear database, in which the Mohr–Coulomb, Patton, and Barton–Bandis criteria are compared with the measured shear-strength envelopes under a common project setting.

2. Review Methodology and Classification Framework

This paper is a critical narrative review supported by an applied benchmark case study (Figure 1). The review focuses on the peak shear strength of clean, unfilled rock joints, primarily under CNL. Rather than a PRISMA-type systematic review, the literature corpus was built using an iterative, criteria- and parameter-driven approach aligned with the goals of the paper. These goals were to synthesize controlling parameters and how they are measured, and then to classify criteria families and evaluate their assumptions and use cases.

The process began from foundational criteria and historically dominant models (e.g., Mohr–Coulomb, Patton, Barton–Bandis, Ladanyi–Archambault) and major review papers already recognized in the field. The reference set was then expanded by backward and forward snowballing, which means screening reference lists and citing papers, within each topic block such as roughness quantification, scale effect, boundary condition/CNL, hydro-mechanical effects, and modern extensions like 3D morphology and data-driven methods.

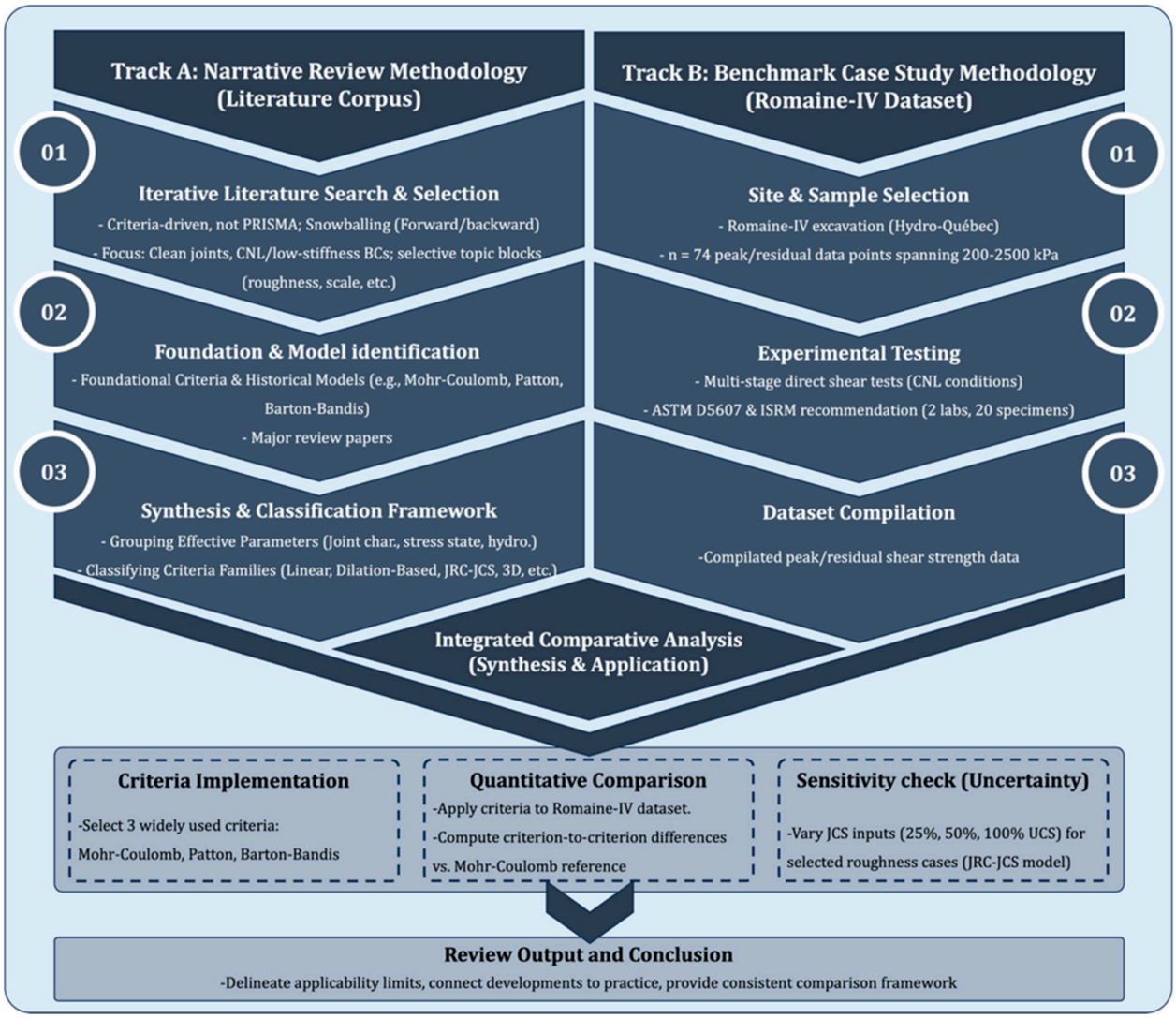

Figure 1. Adopted methodology for the review, integrating an iterative narrative literature synthesis (Track A: snowballing, criteria-driven selection, and classification of seven criterion families) with a quantitative benchmark using the Romaine–IV direct-shear database (Track B: 20 specimens tested under multiple normal-stress stages under CNL conditions) for comparison of the Mohr–Coulomb, Patton, and Barton–Bandis criteria, including a sensitivity assessment of JCS.

3. Controlling Factors and Measurement of Joint Shear Strength

The shear strength of rock joints, a key parameter controlling failure along discontinuities, is governed by a set of interacting mechanical and environmental factors [29–36]. These include joint surface roughness and matching, joint-wall strength, size and persistence of the discontinuity, infilling materials, normal stress level and boundary conditions, and hydrogeological effects such as pore pressure, lubrication, and weathering (Figure 2). Most shear-strength criteria can be interpreted as different ways of combining these factors into a constitutive envelope. In this review, the primary focus is on the peak shear strength of clean, unfilled rock joints under CNL or low-stiffness boundary conditions. Infilled joints, high-stiffness (CNS) boundaries and strongly time-dependent phenomena are briefly discussed to delimit the scope and to highlight where existing criteria become less reliable.

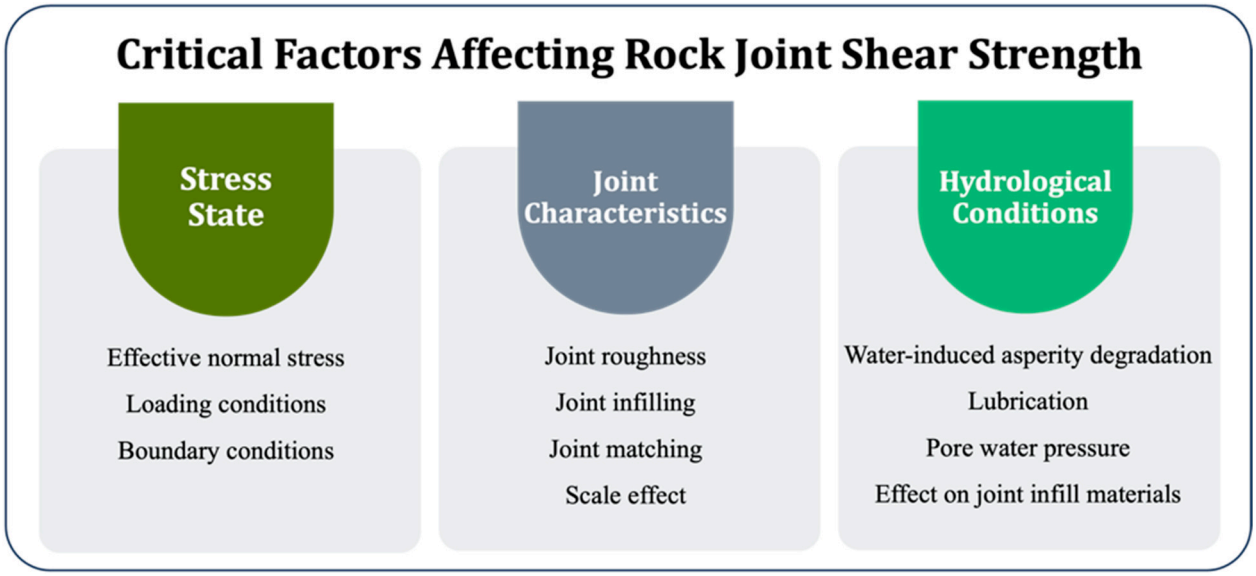

Figure 2. Factors affecting the shear strength of rock discontinuities, organized into three main categories of stress state, joint characteristics, and hydrological conditions, which together control the mechanical interlock and frictional resistance along the joint surface.

3.1. Joint Characteristics

Joint characteristics are central to evaluating the shear strength of rock discontinuities, as they define the mechanical interlock and the resultant resistance to shear forces. Among these, joint roughness plays a primary role by promoting asperity interlocking; higher roughness typically enhances shear strength due to the need to overcome surface irregularities. However, roughness effects are highly sensitive to the orientation and morphology of asperities, underscoring the importance of detailed characterization in predictive modeling [10,37–42]. Joint matching, or the degree of alignment between opposing joint surfaces, also influences shear strength by determining the effective contact area. Misalignment in joint faces can reduce interfacial contact, which compromises shear resistance, while well-matched joints allow for optimal surface engagement and increased resistance to displacement [13,43].

The scale effect further complicates assessments, as larger joint surfaces tend to encompass greater heterogeneities, often leading to reduced shear strength. Laboratory-scale tests often fail to capture this variability, necessitating scaling adjustments when applying lab results to field conditions [5,6,14,44,45]. In addition to these factors, joint infilling significantly alters shear behavior by reducing rock-to-rock contact and enabling sliding along the infilled plane. Materials such as clay or silt infill in joints replace high-strength rock contact with weaker interfaces that can considerably diminish shear resistance. This effect is particularly problematic under saturated conditions, where infilling material may become even more compressible and further lower the joint's load-bearing capacity [46–49]. The degree of weathering is another crucial factor, as chemical and mechanical weathering processes smooth and degrade joint asperities over time, progressively reducing shear resistance [50]. The mineralogical composition of the rock mass is another critical parameter that affects mechanical properties, with various studies highlighting the significant influence of mineralogy on shear strength [51–53].

The friction angle of joint surfaces represents an intrinsic measure of resistance to shear under normal loading conditions. Higher friction angles indicate increased shear resistance, reflecting the inherent properties of the joint material in resisting movement. However, friction angle alone does not adequately capture the full shear response. It is

most accurately interpreted in conjunction with other factors, such as roughness, infilling, and weathering, which collectively shape the joint's shear behavior. In fact, these joint characteristics, including roughness, matching, scale, infilling, weathering, and friction angle, are not isolated but interdependent, each contributing uniquely to the overall shear strength of rock discontinuities. The following sections offer an in-depth analysis of the critical parameters discussed here, each of which plays a significant role in determining shear strength.

3.1.1. Joint Roughness

According to the International Society for Rock Mechanics [54], joint roughness is the geometric measure of surface waviness and unevenness relative to the mean plane and significantly influences the shear strength of rock discontinuities. Researchers have developed a variety of approaches to quantify and classify this roughness, which can be broadly categorized into empirical, statistical, and fractal-based approaches as well as contact or non-contact measurement techniques. One of the earliest and most widely recognized empirical methods for quantifying joint roughness was developed by Barton and Choubey [7]. They introduced the JRC, an empirical scale from 0 to 20 that classifies joint surfaces based on visual comparison with standardized profiles. This method remains widely used due to its simplicity and practicality, though it has been criticized for subjectivity [9,55–58]. Assigning JRC values relies on the observer's experience, which can yield inconsistent results across different studies. Despite this limitation, the JRC continues to provide a baseline for field applications, particularly when rapid roughness assessment is required.

In contrast to empirical methods, statistical approaches offer more quantitative means of evaluating surface roughness. Myers [59] was a pioneer in this area, proposing several profile parameters (Z_1–Z_4) to characterize roughness. Myers' Z_1 parameter (root mean square height) calculates the average deviation of surface heights from the mean plane (Equation (1) in Table 1). Z_1 (RMS height) is directly used as an indicator of surface roughness amplitude. Surfaces with higher Z_1 values typically exhibit greater shear resistance due to increased asperity interlocking. Although Z_1 is simple and widely used, distinct surfaces can have the same RMS value, limiting its uniqueness. Z_2 (RMS slope) measures the average steepness of surface asperities (Equation (2) in Table 1). Z_2 does not differentiate curvature or wavelength. It directly impacts shear strength, as steeper asperities increase frictional resistance during shear displacement. Z_3 (RMS curvature) assesses asperity sharpness through curvature; a related equation (Equation (3) in Table 1). This parameter captures fine-scale texture but is sensitive to noise and measurement resolution. It helps differentiate surfaces with similar Z_1 and Z_2 but distinct fine-scale asperity geometry. It has limited direct use in shear strength prediction, but is valuable for understanding wear and damage evolution during shear displacement. Z_4 (slope length difference) quantifies asymmetry between lengths of upward and downward slopes, indicating anisotropic frictional behavior (Equation (4) in Table 1). This parameter is useful when anisotropy significantly influences fluid flow or directional shear strength. It is applied in traditional shear strength criteria less frequently but is informative for special applications (e.g., evaluating directional roughness anisotropy). The Z_1–Z_4 parameters are visualized in Figure 3.

Tse and Cruden [9] introduced quantitative profile parameters for engineering use, notably reemphasizing Z_2 (root mean square slope) to estimate the JRC. They found a strong correlation between statistical slope measures and the empirical JRC of standard profiles. Their equation relating Z_2 to JRC (Equation (5) in Table 1) helped bridge statistical characterization with Barton's empirical criterion.

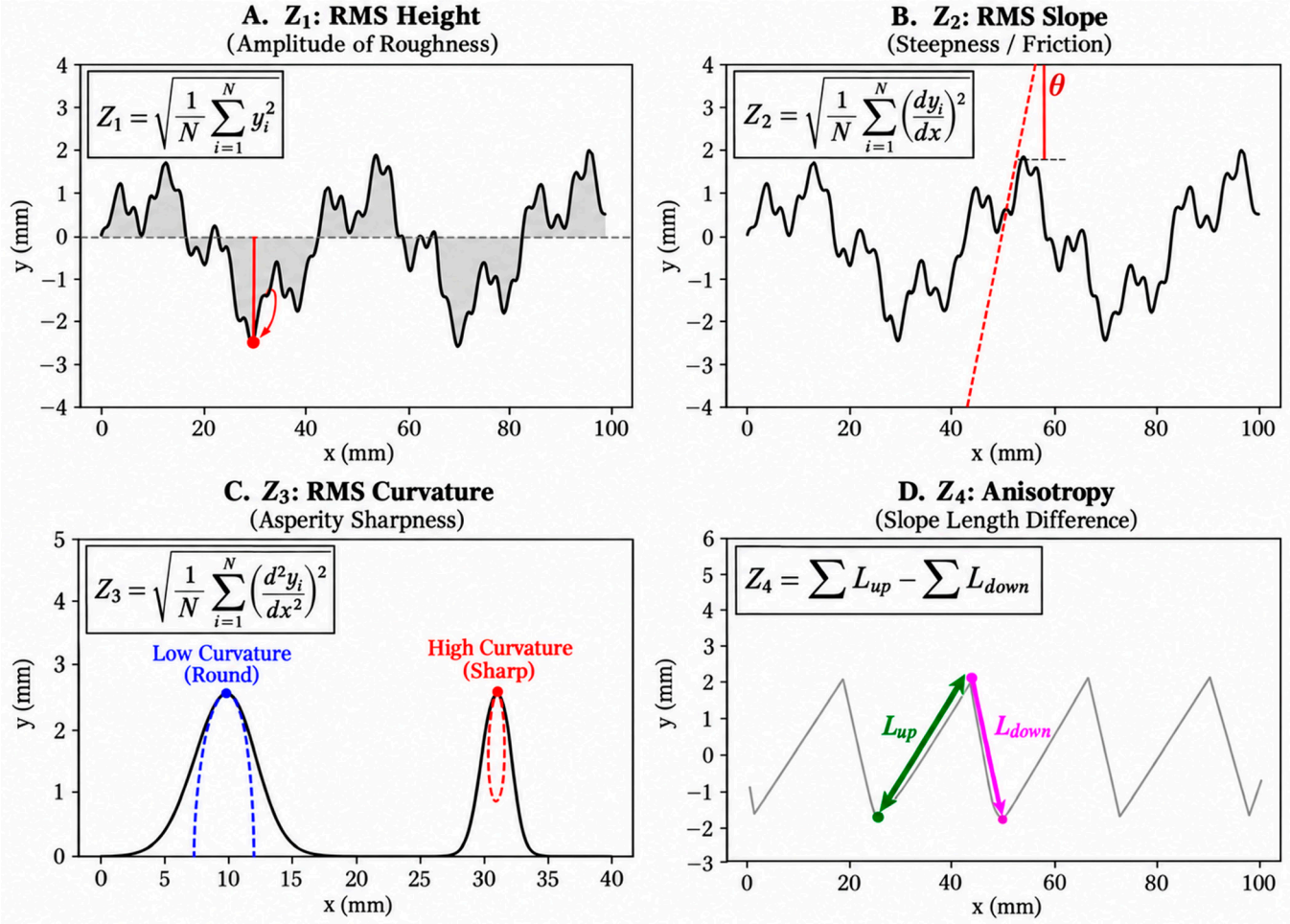

Figure 3. Schematic illustration of Myers' statistical roughness parameters: (**A**) Z_1 (RMS height) quantifies the amplitude of surface irregularities, (**B**) Z_2 (RMS slope) measures the average steepness of asperities and strongly correlates with shear strength, (**C**) Z_3 (RMS curvature) captures fine-scale asperity sharpness sensitive to wear, and (**D**) Z_4 (slope length difference) quantifies directional anisotropy, providing an objective alternative to subjective JRC estimation.

Beyond simple indices, autocorrelation functions (ACFs) and power spectral density (PSD) analyses have been used to statistically characterize roughness [60]. The ACF describes how surface height values are correlated with themselves over a given lag distance, providing insight into the spatial continuity of asperities. Wu and Ali [60] introduced the use of the ACF for joint profiles, treating the surface as a stochastic process and computing correlation lengths to represent the roughness structure. The PSD, essentially the Fourier transform of the autocorrelation, reveals the frequency content of the surface topography. Their study demonstrated that the PSD could be used to identify dominant waviness wavelengths and the distribution of roughness energy across scales (e.g., distinguishing surfaces with predominantly short-wavelength roughness from those with long undulations). Together, ACF and PSD provide a frequency-domain complement to spatial domain metrics because the ACF captures how quickly a surface's height variations decay with distance (related to the surface's correlation length), while the PSD quantifies roughness as a function of wavelength. Modern studies continue to use these functions for a deeper statistical representation of roughness.

Later, Riss et al. [61] utilized geostatistical analysis (e.g., variograms) to quantitatively describe joint surface morphology (Figure 4). They modeled the spatial structure of asperity heights, enabling a stochastic simulation of surface profiles. This work provided the groundwork for reconstructing and analyzing rough surfaces beyond simple profiles. They integrated image analysis with statistical characterization to study sheared joint surfaces. By converting surface scans to binary images, they examined asperity damage distribution during shear, which quantified roughness degradation and anisotropy in shear and contributed to the statistical understanding of joint morphology evolution.

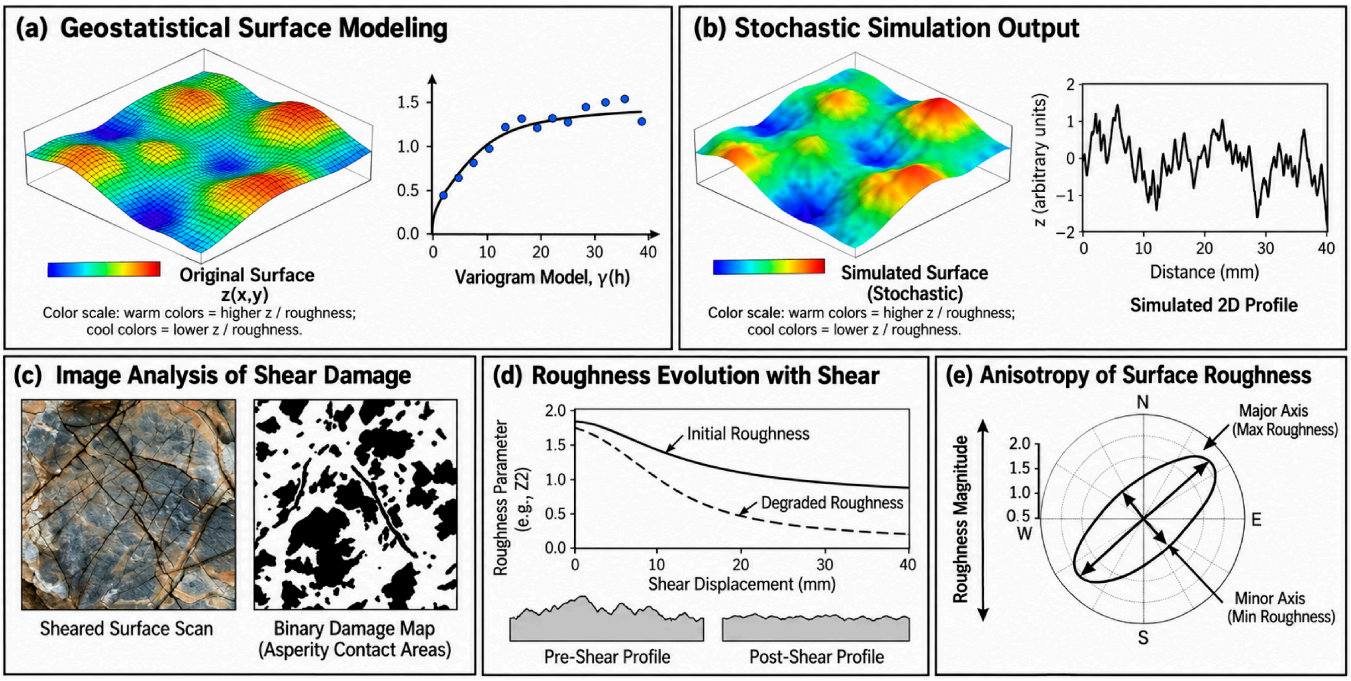

Figure 4. Geostatistical and image-analysis workflow for stochastic joint-surface reconstruction and characterization of shear-induced roughness degradation and anisotropy: (**a**) geostatistical surface modeling, (**b**) stochastic simulation output, (**c**) image analysis of shear damage, (**d**) roughness evolution with shear, and (**e**) anisotropy of surface roughness (adapted from Abbas et al. [53]).

Marache et al. [62] applied full geostatistical modeling to a rock fracture surface. They used variograms to characterize the spatial roughness and then statistically reconstructed the 3D fracture surface topography, which allowed for numerical shear tests on the simulated surfaces. They demonstrated that statistical and geostatistical methods could capture scale-dependent roughness features and their impact on shear strength.

Building on these statistical measures, Sayles and Thomas [63] introduced the structure function (SF), an autocorrelation-based method that evaluates the relationship between adjacent surface points (Figure 5). The SF method provides a more comprehensive understanding of surface variability by quantifying how surface heights change over a given distance. A key limitation of this approach is its sensitivity to large-scale surface changes, which can obscure finer roughness details.

Advancements in technology have also enabled the development of non-contact methods for measuring joint roughness. Laser profilometry, for instance, offers high-resolution surface data without physical contact and has gained widespread use due to its ability to capture fine surface details often missed by contact-based techniques like mechanical stylus profilometry. This method is particularly effective when high precision is required, for example, in characterizing highly irregular or damaged rock joints.

Kulatilake et al. further advanced the field by incorporating fractal analysis into joint roughness studies [64]. They demonstrated that rock surfaces exhibit self-affine properties, meaning that their roughness characteristics change with observation scale. The fractal dimension (D), a key parameter in this approach, quantifies the complexity of a surface by measuring how much detail appears as the scale of observation changes [65]. Higher fractal dimensions indicate more complex surface geometries. This fractal-based research provided a significant advance in understanding the multi-scale nature of roughness, allowing for a more accurate modeling of rock joint behavior. Tatone and Grasselli [10] later refined this approach by introducing a model that relates the JRC to the maximum apparent dip angle (θ^*_{max}) of surface asperities. Their method uses the dip angle and a roughness parameter (C) derived from a regression analysis to provide a more detailed characterization of joint surfaces, addressing some of the limitations of earlier empirical models, particularly regarding accuracy and reproducibility.

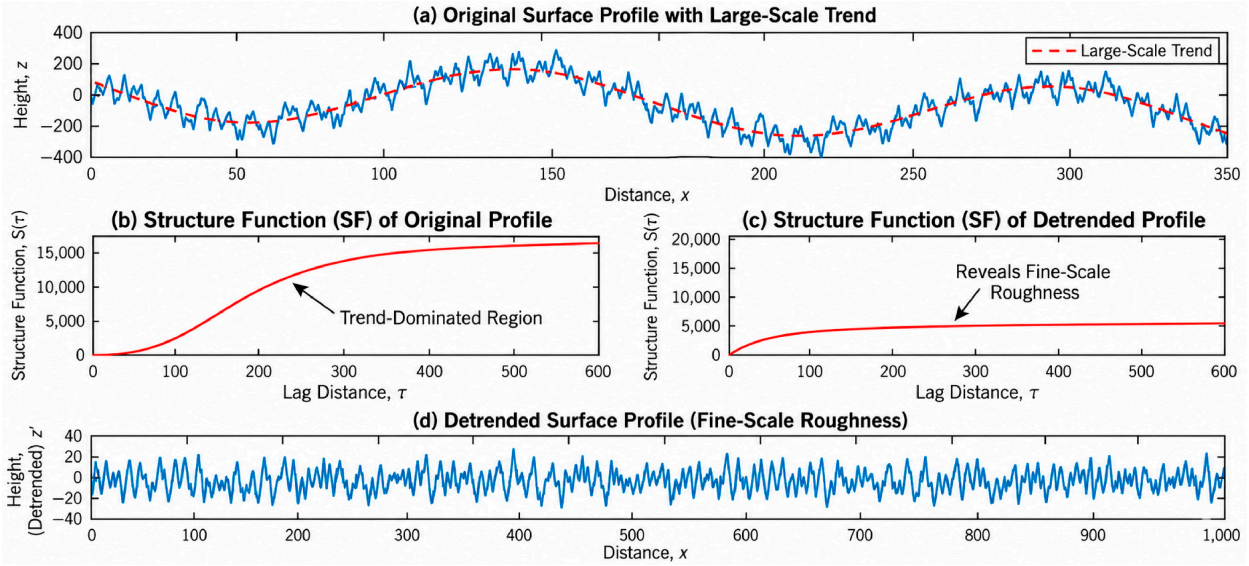

Figure 5. Example of laser profilometry roughness processing: removal of the large-scale trend and structure-function analysis to isolate fine-scale joint roughness.

Fractal-based methods, as explored by Jiang et al. [66], offer the most robust approach for characterizing roughness at different scales. Methods such as the projective covering method (PCM) calculate fractal dimensions for three-dimensional surfaces, providing detailed insights into surface morphology. While these methods provide a high level of detail, they are computationally intensive and require precise surface measurements, limiting their use in large-scale field studies. Ban et al. [67] later developed a three-dimensional roughness parameter system comprising two distinct measures, one statistical and one fractal, based on the concept of equivalent asperity height differences. In this system, a statistical parameter (AHD_0) is defined as the average equivalent height difference of surface asperities at a 1 mm scale, and a fractal parameter (D_{AHD}) represents the surface's fractal dimension. Together, these capture asperity height amplitude and scale-dependent roughness complexity to better characterize the joint's contribution to shear strength. This approach has proven effective in describing surface anisotropy, though it remains constrained by the availability of high-resolution surface data. Despite this limitation, such comprehensive roughness characterization helps address the complexity and variability inherent in rock surfaces and provides a range of methods suited to different scales and applications. These methods and equations are summarized in Table 1.

Table 1. Summary of joint roughness quantification methods.

Category	Reference	Method	Description	Equation		Advantages	Limitations
Empirical	Barton et al. [7]	JRC	Visual comparison of surfaces	—		Widely used; simple	Subjective, limited to visual matching
Statistical	Myers [59]	RMS Height (Z_1)	Root mean square of asperity height	$Z_1 = \sqrt{\frac{1}{L}\int_0^L [y(x)]^2 dx}$ $y(x)$: vertical height deviations of the profile from the mean reference plane L: the total length of the measured profile	(1)	Easy calculation, direct height measurement	May not differentiate similar profiles
		RMS Slope (Z_2)	Measures the mean square value of the slope	$Z_2 = \sqrt{\frac{1}{L}\int_0^L \left(\frac{dy}{dx}\right)^2 dx}$ $\frac{dy}{dx}$: first derivative of the profile	(2)	Strong correlation with JRC	Ignores curvature effects
		RMS Curvature (Z_3)	Root mean square curvature of asperities	$Z_3 = \sqrt{\frac{1}{L}\int_0^L \left(\frac{d^2y}{dx^2}\right)^2 dx}$ $\frac{d^2y}{dx^2}$: Second derivative of the profile	(3)	Captures finescale roughness	Sensitive to noise and resolution
		Slope Length Difference (Z_4)	Quantifies anisotropy by slope length asymmetry	$Z_4 = \frac{\sum (\Delta x)_p - \sum (\Delta x)_n}{L}$ $(\Delta x)_p$: length of upward (positive) sloped profile segments $(\Delta x)_n$: the length of downward (negative) sloped profile segments	(4)	Useful for directional analysis	Less direct use in shear strength predictions
	Tse and Cruden [9]	Correlation between Z_2 and JRC		$JRC = a + b \cdot log\, z_2$ a, b: empirical constants	(5)	Objective, reduces subjectivity	Requires calibration from data
	Sayles et al. [63]	Structure Function (SF)	Quantifies roughness via slope variation	$SF = \frac{1}{L}\sum (z_i - z_{i+1})^2/(x_{i+1} - x_i)$ z: surface coordinates L: profile length	(6)	Objective slope analysis	Sensitive to the sampling interval
	El-Soudani [68]	Roughness Profile Index (RP)	The ratio of profile length to the horizontal distance	$RP = \frac{\sum\left[(x_{i+1} - x_i)^2 + (z_{i+1} - z_i)^2\right]}{L}$ x, z: Coordinates L: profile length	(7)	Analyzes anisotropy	Limited to two-dimensional profiles

Table 1. *Cont.*

Category	Reference	Method	Description	Equation		Advantages	Limitations
Statistical	Tatone & Grasselli [69]	Mean Positive Inclination Angle (θ_P^+)	The mean angle of profile slopes	$\theta_P^+ = tan^{-1}\left(\frac{1}{M_x^+}\sum\left(\frac{\Delta z}{\Delta x}\right)\right)$ $\Delta z, \Delta x$: height distance	(8)	Captures direction-specific roughness	It does not account for the amplitude
	Grasselli & Egger [41]	Maximum Apparent Dip Angle θ^*	Anisotropic roughness measure incorporating potential contact area	$A_{\theta*} = A_0\left(\frac{\theta_{max}-\theta^*}{\theta_{max}}\right)^C$ θ_{max}: max dip angle A_0: the maximum contact area ratio	(9)	Accounts for contact area and dip angle Produces a scale-independent 3D roughness descriptor	It may not capture complex asperity details Requires high-resolution 3D surface data and calibration;
	Xia et al. [70]	Root Mean Square (RMS)	Represents deviation from the mean profile height	$RMS = \sqrt{\frac{1}{M}\sum z_i^2}$ M: number of data points z_i: height values from mean profile	(10)	Simple amplitude measure	Limited for rougher, non-linear surfaces
	Homand et al. [71]	Surface Roughness Coefficient (RS)	The ratio of actual to the nominal area of rough surface	$RS = \frac{A_t}{A_n}$ A_t: actual surface area A_n: nominal surface area	(11)	3D measure; indicates surface detail	Less suitable for two-dimensional surfaces
Fractal	Um; Kulatilake et al. [72,73]	Fractal Dimension (D)	Measures the self-affinity of rock profiles	Varies by method, variogram, or spectral method $D_f = \frac{log(N(L))}{log(L)}$ L: Profile length	(12)	Suitable for scale-invariant roughness	Complex; dependent on input parameters
	Belem et al. [42]	Modified 3D Divider Method	Extension of the divider method to three-dimensional surfaces	Varies by application		Provides 3D roughness detail	Difficult to implement on large surfaces

3.1.2. Joint Matching

Rock joints form at various stages and under differing conditions, leading to alterations that affect the geometric and geomechanical properties of the fractured rock mass. These processes result in joint surfaces with distinct profiles on each side, often causing mismatching between the surfaces. It is common for joints to exhibit similar roughness levels but misalignment due to alterations and dislocations over time. Research indicates that the peak shear strength of rock joints is influenced by surface roughness and the degree of matching (Figure 6) between joint surfaces. Mismatching can arise from factors such as vibration from nearby blasting, excavation, or seismic activity [13].

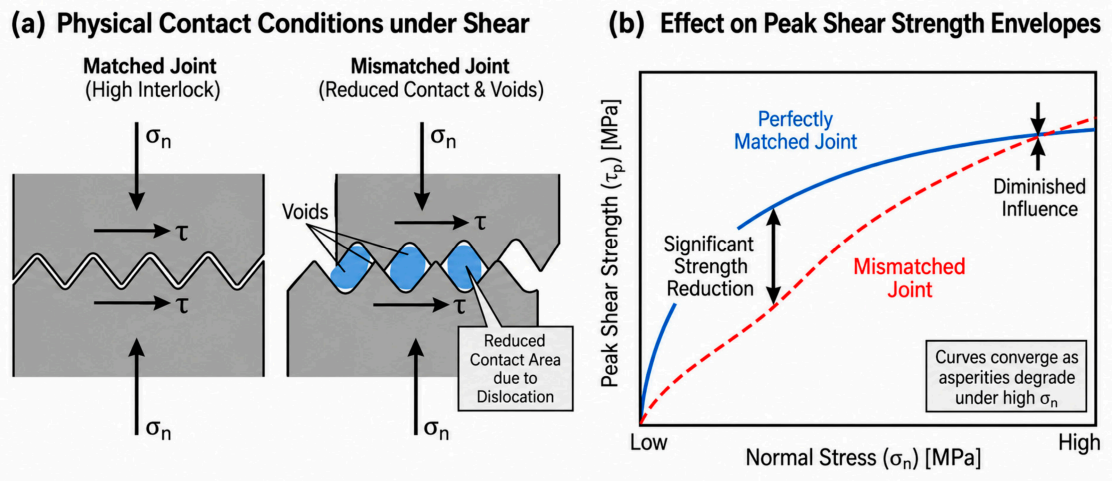

Figure 6. Effect of joint surface matching on physical contact conditions and peak shear strength envelopes, highlighting reduced interlock and strength for mismatched joints.

To quantify joint alteration, Zhao introduced the joint matching coefficient (JMC) as a roughness-independent geometric parameter to describe joint mismatching. Zhao also proposed a modified criterion for the JCS and JRC relationship, incorporating JMC in what became the JRC–JMC criterion [43]. Additionally, Oh and Kim examined the impact of joint openings on the shear behavior of rock joints, particularly when joint alterations significantly affect shear strength [74]. Their studies, conducted around underground openings and on irregular-sided blocks and rock wedges, highlighted the influence of joint mismatching on shear strength. However, the proposed methods for quantifying joint surface profiles to better understand shear behavior based on modified JRC values still face limitations, particularly the inherent constraints associated with JRC [55,75]. Consequently, the practical determination of JMC remains challenging for establishing an effective JRC–JMC criterion.

Tang and Wong [13] expanded on this by developing a shear failure criterion that accounts for mismatched rock joints, incorporating three-dimensional roughness and joint misalignment. They prepared replicas of naturally matching rock joints with varied morphologies using mixtures of plaster, sand, and water in different ratios. By imposing horizontal dislocations of varying magnitudes between the blocks, they modeled mismatching conditions and observed the effects. Their findings indicate that as normal stress increases, the influence of dislocation diminishes, suggesting that joint mismatching plays a more significant role under lower normal stresses.

3.1.3. Scale Effect

Neglecting the scale effect can lead to significant inaccuracies in estimating the field shear strength of rock joints. Laboratory tests often provide shear strength results based on small-scale joint samples, which may not adequately reflect the behavior of larger natural

joints found in situ. In particular, larger natural joints tend to exhibit complexities not captured in pristine lab specimens. These complexities include multi-scale surface irregularities with smaller asperities nested within broader undulations [76], open joint segments (apertures) that can become filled with weaker gouge material, and weathered surface layers, all of which can reduce shear resistance [77]. For these reasons, to accurately assess the field response of rock joints under shear stress, it is essential to consider both small-scale roughness obtained from laboratory data and large-scale waviness observed through geological studies (Figure 7). This approach allows for a comprehensive understanding of dilation and shear strength characteristics at different scales [78].

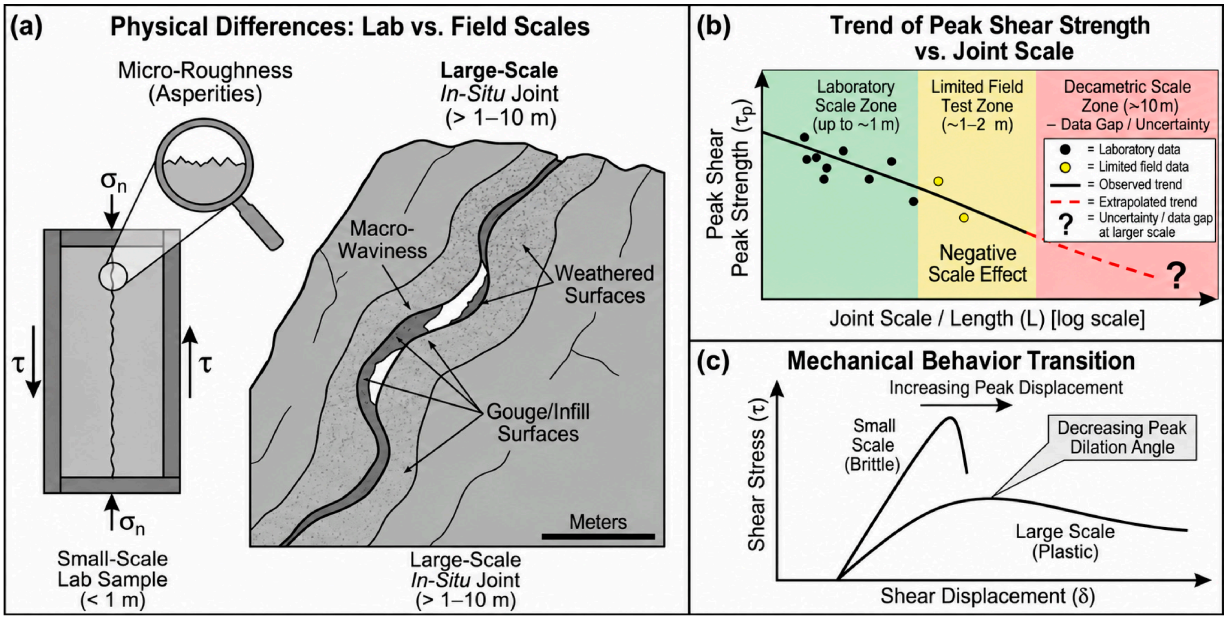

Figure 7. Conceptual illustration of joint scale effects, contrasting lab- and field-scale roughness/conditions and showing the typical negative scale effect on peak shear strength and the brittle-to-plastic transition with increasing joint size.

Geological processes, such as tectonic shifts, faulting, and sediment deposition, create surface roughness that significantly influences shear behavior across various joint sizes. These processes not only produce pronounced undulations and roughness on joint surfaces (often manifesting as asperities at multiple scales) but also contribute to variable joint conditions like infilling and weathering over time. Consequently, the geomechanical properties measured in laboratory settings may require adjustment to account for scale differences on joint surfaces.

Table 2 summarizes the research studies that have explored the influence of scale on the shear strength of rock masses. The table lists the sizes of both in situ and laboratory samples, the rock types tested, and the corresponding shear strength values. The findings consistently demonstrate that as joint size increases, both peak shear strength and joint roughness tend to decrease, an observation known as the negative scale effect. However, some studies suggest the existence of a positive scale effect or even a negligible scale effect, indicating that the relationship between joint size and shear strength may vary under certain conditions. As the joint length grows, peak shear displacement tends to increase gradually, signaling a shift in deformation behavior. Additionally, there is a noticeable decrease in the peak dilation angle, reflecting reduced joint expansion during shear. Therefore, the scale dependence of rock joint mechanical behavior remains uncertain and is a potential future research direction.

The stress–strain relationship often transitions from a brittle to a plastic behavior pattern on the shear stress–shear displacement curve, indicating a change in the failure mechanism. Finally, joint roughness tends to increase, which can influence interlocking and overall joint surface stability [6].

Table 2. Summary of the studies on joint shear strength scale effects, highlighting sample sizes, methodologies, key findings, observed scale effects, and limitations.

Researcher	Sample Size (Laboratory)	Sample Size (In Situ)	Methodology	Key Findings	Scale-Effect	Limitations
Barton et al. [3]	36–40 cm	Up to 5 m	In situ and laboratory direct shear tests on sandstone, limestone, and siltstone samples of varying sizes.	Negative scale effect with a decrease in shear strength and transition from brittle to plastic behavior at larger scales.	Negative	Lab samples may overestimate the effects of large joints and may not fully reflect field behavior.
Tse et al. [9]	50 mm–100 cm	Up to 10 m	Laboratory and field tests on sandstone and limestone samples of varying scales.	Observed that shear strength can increase with scale due to the development of additional asperity interlocks.	Positive	Limited to certain rock types; larger samples are required for more generalized conclusions.
Zhang et al. [79]	Up to 300 mm	Up to 5 m	Utilized numerical models to analyze the shear behavior of rock joints with various roughness scales.	A positive scale effect was noted due to increased contact area between rough joint surfaces at larger scales.	Positive	The numerical model requires field validation and is limited to specific roughness patterns.
Borri-Brunetto et al. [80]	Various scales	N/A *	Experimental shear tests on various scales of natural rock joints	The confirmed scale effect was a reduction in shear strength at larger scales, with variations in peak shear displacement.	Negative	Experimental limitations with large rock samples confined to specific rock types.
Fardin et al. [81]	100–1000 mm	1000 mm	3D laser scanning and fractal analysis on large-scale rock joint replicas.	Surface roughness and fractal parameters exhibit scale dependence; values stabilize beyond a stationarity threshold.	None	The stationarity threshold limits the application scope and lacks large-scale empirical validation.
Lee et al. [82]	Various sizes	N/A	Conducted shear tests on synthetic joints and natural joints under various loading conditions.	In certain conditions, a positive scale effect was found, attributable to the mobilization of additional frictional resistance at larger scales.	Positive	Results are limited to specific joint types and may not generalize to all rock types.
Grasselli et al. [41]	Various scales	N/A	Surface roughness-based shear strength model using 3D surface parameters for rock joints.	Developed a constitutive law for scale-dependent shear strength based on quantified roughness; aligns well with field data on small to medium scales.	Negative	Model scaling to very large joints requires empirical validation, limited by rock sample size.
Bahaaddini et al. [6]	Various sizes	N/A	Numerical simulations using particle flow code (PFC2D) on joints of varying sizes.	A negative scale effect was observed, with peak shear strength and stiffness decreasing as joint length increased.	Negative	The model does not account for all physical irregularities and limited real-world validation.
Oh et al. [45]	Various sizes	N/A	A constitutive model incorporating small-scale roughness and large-scale waviness based on laboratory data.	The degradation model based on plastic work shows a scale-dependent reduction in peak shear stress and displacement.	Negative	Complex model parameters, primarily lab-based validation.

Table 2. *Cont.*

Researcher	Sample Size (Laboratory)	Sample Size (In Situ)	Methodology	Key Findings	Scale-Effect	Limitations
Li et al. [78]	400 mm	N/A	Fractal model for large-scale joints with fractal descriptors for different scales.	Fractal descriptors for critical waviness and unevenness correlate well with reduced shear stress at larger scales.	Negative	The fractal model lacks empirical field validation; it is difficult to scale from lab measurements to field applications.
Mouzannar et al. [83]	Various scales	N/A	Experimental study on concrete-rock interfaces considering morphology and scale.	Scale effect observed; roughness and surface morphology significantly impact shear strength.	Negative	Field validation needed; limited to specific surface conditions.

* N/A: Not available.

The studies summarized in Table 2 reveal that experimental assessments of joint shear strength have primarily been constrained to laboratory scales, typically up to approximately one meter. The largest laboratory direct shear tests reported joint surface areas of around 1 m^2 (~9600 cm^2), with linear dimensions generally within the range of 0.5–1 m. In situ field tests are even rarer, with a few experiments involving joint lengths of up to approximately 1–2 m under controlled conditions. Consequently, the existing empirical data predominantly reflect this upper boundary of feasible laboratory and field-testing scales.

At larger scales, particularly at decametric scales (tens of meters), direct experimental verification of joint shear strength behavior remains notably absent due to practical and logistical limitations. Thus, any scale-dependent behaviors identified at meter scales must be extrapolated, significantly increasing uncertainty. At these larger scales, characteristics such as long-wavelength waviness, joint segmentation, and intact rock heterogeneity between persistent asperities may dominate, potentially altering shear strength behavior substantially. Existing empirical models and criteria lack validation for discontinuities extending beyond approximately 10 m, highlighting a critical knowledge gap. This limitation emphasizes caution when applying current shear strength relationships to very large joints and underscores the need for further experimental or numerical research to characterize and confirm shear behaviors at decametric and larger scales.

3.1.4. Joint Infilling

All materials existing between the walls of the joints are referred to as joint filling. The infilling includes in situ weathered materials, external materials, and fault zone materials (gouge) either deposited or intruded between the joint surfaces [54]. An infilled rock joint is likely to be the weakest plane in a rock mass. The presence of infill material within the joint significantly reduces the friction of the discontinuity boundaries by reducing rock-to-rock contact of the joint walls. The thicker the infill, the lower the shear strength of the rock joint. Once the infill reaches a critical thickness, the infill material governs the overall shear strength, and the rock joint (rock) wall plays no significant role. Several models have been proposed to predict the peak shear strength of soil-infilled joints, considering the ratio of infill thickness (t) to the height of the joint wall asperity (a). CNS models provide a more realistic picture of the soil-infilled joint behavior in the field.

From a mechanistic point of view, despite the high complexity of natural joints and their fillings, the problem can be reduced to four basic cases of discontinuities including clean without filling or coating, coated joints, joints with clay-like infilling, and joints with sand-like infilling. In unfilled joints, the roughness and compressive strength of the joint walls are all important, while in the case of filled joints, the physical and mineralogical properties of the material separating the joint walls are of primary concern. It is a common practice

to assume that the shear strength of an infilled joint is equal to that of the infill material. However, this assumption can often lead to either underestimation or overestimation of joint strength. Several parameters may influence the shear strength of filled joints, among which some important aspects, such as the scale effects, pore pressure drainage and consolidation ratio, still need to be better understood. The most pronounced effect of the presence of an infill material is the reduction in friction along the discontinuity boundaries due to reduced rock-to-rock contact of the joint walls. Shear strength is also influenced by the infill material's nature and the characteristics of the wall-filling interfaces. Rock joints filled with fine materials are likely to be the weakest elements in a rock mass due to the low frictional properties of the infill. For example, joints filled with wet, clayey materials often have very low shear resistances, making them the weakest planes available for the initiation of sliding.

3.2. Stress State

The stress state is governed by the magnitude of normal stress, the boundary condition under which the joint deforms (e.g., CNL or CNS), and the loading condition applied (monotonic or cyclic shear) [1,8,17]. Importantly, hydrogeological conditions—such as pore water pressure and saturation—directly influence the effective stress and modify joint behavior [84–86]. These components together define the stress environment that controls peak shear strength, dilation potential, failure mechanisms, and the long-term stability of discontinuities in rock masses.

3.2.1. Effective Normal Stress

Effective normal stress refers to normal stress (σ_n) acting normally on the joint surfaces [87]. It is a critical factor governing the shear strength of rock discontinuities. Several studies have confirmed that higher normal (effective) stress generally leads to a greater peak shear strength of joints [88,89]. In practice, an increase in normal stress causes more intimate contact between the rough joint surfaces, mobilizing higher frictional resistance and greater asperity interlocking. Essentially, a larger normal load enhances the true contact area and frictional resistance along the joint, thereby requiring a higher shear force to initiate sliding [89].

Moreover, normal stress influences the dilatancy behavior of the joint during shear. Higher normal stress tends to constrain joint dilatancy by clamping the surfaces together more tightly. When dilation is restricted by a heavy normal load, the shearing process must do additional work against this load, which effectively increases the shear strength mobilized [90]. In contrast, under lower normal stress, the joint can dilate more freely as the surfaces slide, contributing less frictional resistance. For example, with low normal load, a rock joint may slide by climbing over its undulations (accompanied by significant dilation), whereas at higher normal load, the dilation is much smaller, and shear occurs through asperity abrasion or breakage [76]. Consequently, the shear strength is higher under high normal stress because the joint cannot easily dilate and instead must overcome both friction and the breakage of interlocked asperities.

At low normal, rock joints often exhibit strain weakening or brittle behavior with a sharp drop in shear stress after the peak due to the sudden failure of surface asperities and the low tensile strength of the rock material comprising those asperities [91]. In this low-confinement regime, once the peak shear strength is reached, the weak rock asperities snap off abruptly, causing a rapid loss of resistance. Rock is much weaker in tension, about one-tenth of its compressive strength than in compression, so asperity tips can crack and shear off under relatively small shear displacements once their normal stress is high [89,91]. Under higher normal stress (greater confinement), however, the failure of asperities becomes more gradual and constrained. The increased confinement prevents instantaneous brittle failure

and promotes a more ductile sliding or grinding of asperities, resulting in a smaller post-peak drop in strength. Thus, increased normal confinement tends to induce more stable (ductile) sliding behavior in the joint, whereas low confinement leads to sudden brittle failure. The net effect is that normal stress (especially effective normal stress in presence of water) directly controls the shear strength through frictional interlocking, dilatancy suppression, and asperity damage.

3.2.2. Loading Condition and Boundary Conditions

Laboratory shear tests on rock joints are typically run under CNL conditions, where the applied normal stress is held fixed and the joint is free to dilate during shear. In the field, however, the normal stress on a joint may not remain constant because surrounding rock or support structures can impose stiffness that resists joint opening, as illustrated in Figure 8. This corresponds to a CNS boundary condition, where any joint dilation is constrained by an increase in normal stress from the confining medium. Many real scenarios (e.g., a wedged block in a slot, an underground excavation's wall, or a rock-socketed pile) exhibit CNS behavior, since the joint's expansion is limited by the stiffness of adjacent rock or support elements.

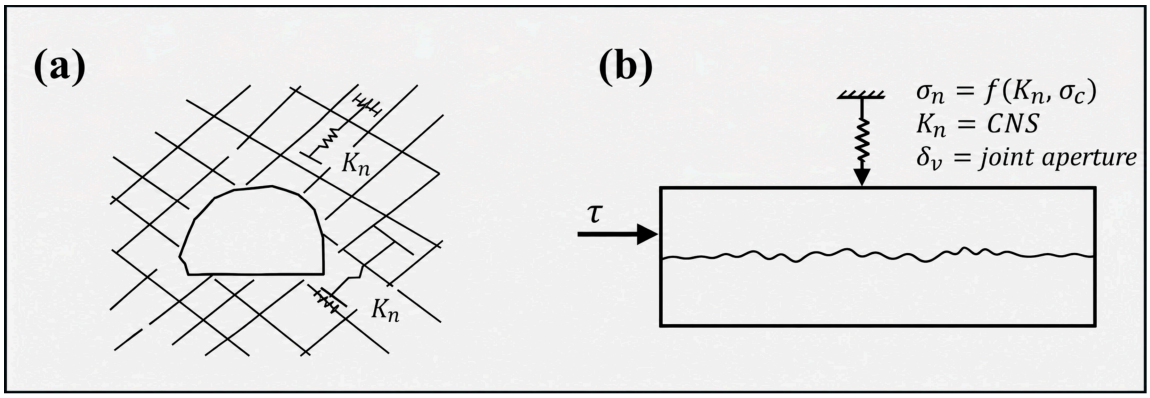

Figure 8. Joint behavior in the roof or walls of an underground excavation. (**a**) Underground excavation in jointed rock. (**b**) Equivalent two- dimensional model for joint on the top of roof (adapted from Thirukumaran and Indraratna [23]).

The choice of CNL versus CNS has important effects on joint shear strength and deformation. Under CNS conditions, the joint cannot dilate freely, so as shear progresses, any attempted opening of the walls causes the normal stress to rise because the stiff boundary pushes back. This leads to a higher mobilized normal force at peak, which often produces a higher peak shear strength compared to the equivalent CNL test. For example, Skinas et al. [91] observed that for identical rock joint specimens, the peak shear stress achieved under CNS was greater than under CNL, precisely because the normal load increased during shear in the CNS case. At the same time, dilation was markedly suppressed in the CNS tests. Indraratna et al. [92] explain that this effect results from the joint being jammed by rising normal stress as it tries to dilate, so the rough asperities mobilize more frictional resistance but undergo less opening. One consequence is that the shear strength envelope (shear vs. normal stress relationship) becomes more curved under CNS conditions. In particular, rougher joints show more pronounced curvature of the failure envelope when normal stress is allowed to build up during shear. In contrast, under CNL, the failure envelope tends to be more or less curved over typical stress ranges, since the normal force is constant by design. Boundary condition also affects the deformation at peak strength. CNL tests generally reach peak strength at a smaller shear displacement, whereas CNS tests require larger shear displacement to reach peak because the increasing normal stress continuously

strengthens the joint as it shears. For instance, Indraratna et al. [93] showed with sawtooth joint specimens that the peak shear stress in a CNL test occurred at significantly lower displacement than in a CNS test on the same joint profile. In summary, a stiff normal boundary tends to elevate peak shear strength and limit dilation, but causes the joint to require more shear movement to fully mobilize resistance, while a free normal boundary (CNL/CSL) allows larger dilative deformation but with a lower peak strength for the same initial normal stress.

Another important loading condition distinction is between monotonic loading and cyclic loading. Monotonic shear is typically used to determine peak and residual strength under a single loading event. In contrast, cyclic loading is critical for understanding the fatigue and degradation of joints under repeated stress such as seismic vibrations or machine-induced cycles. Experimental evidence shows that cyclic loading can both strengthen and weaken a rock joint, depending on the number of cycles and amplitude. During the initial cycles, a joint may undergo closure and seating of asperities as micro-irregularities are compressed or sheared off, causing the joint surfaces to fit more closely. This contraction under a low number of pre-peak cycles can actually increase the real contact area and slightly raise the peak shear strength in subsequent loading. Fathi et al. [93] observed this effect in tests on unweathered granite joints. A few cycles at 30–50% of the ultimate load caused steep asperities to come into better contact, resulting in a modest increase in the peak shear parameters compared to a purely monotonic test. With continued cycling, however, damage accumulates on the joint surface. Additional cycles tend to grind down second-order asperities and induce wear, leading to a net degradation of shear strength. In the tests by Fathi et al. [93], after a larger number of cycles, the joint's peak shear strength began to slowly decrease as asperity degradation overtook the initial friction gain. More generally, cyclic shear loads that approach the failure level cause progressive fatigue of the joint, with micro-cracks propagating and asperity interlock diminishing with each cycle. Empirically, cyclic loading with even moderate stress amplitude can significantly reduce the peak shear strength of a joint relative to a single static loading to failure. This reduction is attributed to the incomplete re-mobilization of all asperities in each cycle and the cumulative damage from micro-fracturing and smoothing of the interface as cycling continues. In other words, the joint does not fully recover its shear resistance between cycles, so the effective strength drops over time. Eventually, under enough cycles, the peak strength may fall to the level of the steady-state residual strength. Notably, however, the residual shear strength itself is often less sensitive to pre-peak cyclic history. Fathi et al. [93] reported that whether a joint had 5 or 1000 small pre-failure cycles made little difference to the ultimate residual strength attained after large displacements. The primary effect of cyclic loading is thus on the peak and pre-peak behavior, with faster stiffness loss and lower peak shear stress compared to monotonic loading in the long run. In design terms, joints subjected to repeated or oscillatory loads may fail at lower shear stresses than predicted by monotonic tests and exhibit hysteresis and stiffness degradation that must be accounted for in any cyclic shear strength criteria.

3.3. Hydrogeological Conditions

Hydrogeological conditions critically affect the shear strength of rock joints through multiple interrelated mechanisms including pore water pressure, lubrication effects, asperity degradation, and changes to infill material behavior. First, pore water pressure directly reduces effective normal stress ($\sigma'_n = \sigma_n - u$), thereby lowering frictional resistance along the joint surfaces. Elevated pore pressure, especially under rapid or undrained conditions (e.g., heavy rainfall, rapid reservoir changes), significantly diminishes joint shear strength by reducing effective confinement. This transient pore pressure often leads to instability and

slope failures, highlighting the importance of dynamic groundwater conditions in stability analysis [94,95].

Second, water acts as a lubricant, reducing the friction coefficient and the basic friction angle of rock joints. Experimental studies consistently demonstrate substantial reductions in friction angle and intrinsic friction when joints transition from dry to saturated conditions. The magnitude of this weakening varies with surface roughness and mineralogical characteristics, as highly rough joints experience notable decreases in shear strength due to diminished asperity interlocking.

Third, sustained water exposure accelerates both the mechanical and chemical degradation of joint asperities. Mechanically, water intrusion promotes micro-crack propagation, reduces fracture toughness, and enhances asperity breakdown during shearing. Chemically, dissolution processes and stress-corrosion cracking progressively deteriorate asperities over time, leading to long-term weakening of joint shear strength. Furthermore, repeated cycles of wetting and drying amplify these degradation processes, cumulatively reducing shear strength.

Fourth, joint infill materials are particularly sensitive to water content. Under saturated conditions, infill materials, especially clays, lose inter-particle cohesion and friction, substantially lowering shear strength. Conversely, partially saturated infills can temporarily enhance shear resistance through matric suction. However, in undrained conditions, saturated infills generate excess pore pressures, further decreasing joint strength and potentially triggering rapid shear failures, a common scenario in landslides and tunnel instabilities.

Finally, over extended periods, water influences rock joints through subcritical crack growth and creep processes, leading to gradual strength degradation even under constant loading conditions. Creep experiments show accelerated deformation and earlier failure of saturated joints compared to dry ones, highlighting how long-term hydrogeological exposure can dramatically shorten the lifespan and compromise the stability of rock engineering structures.

Beyond the simple reduction in effective normal stress, the spatial distribution of pore pressure along a joint surface can significantly influence the local stress state and, consequently, the shear strength. In rough or infilled joints, the contact area is typically heterogeneous, with some portions of the surface being in intimate rock-to-rock contact while others remain open or filled with gouge. This morphological variability creates hydraulic pathways that can lead to non-uniform pore pressure distributions, particularly under transient conditions such as rapid reservoir drawdown or intense rainfall infiltration. In zones of high contact stress, the local effective normal stress may be substantially higher than the average value, potentially suppressing dilation and promoting asperity damage, whereas in open or poorly contacted regions, pore pressure may remain high and reduce frictional resistance. The interaction between pore pressure heterogeneity and the local normal stress field is further complicated by the boundary conditions under which the joint deforms. Under drained conditions, pore pressures may equilibrate relatively quickly, whereas under undrained or partially drained conditions, local excess pore pressures can develop, leading to time-dependent strength degradation. These effects are particularly relevant for infilled joints, where the infill material may have low permeability and high compressibility, resulting in delayed pore pressure dissipation and progressive weakening of the interface. A comprehensive treatment of pore pressure effects thus requires consideration of both the average effective stress and the spatial variability of hydraulic and mechanical conditions across the joint surface.

4. Evolution of Shear Strength Criteria for Clean Joints

To organize the extensive body of shear-strength criteria for clean rock joints, this section adopts a chronological–mechanistic classification that groups models by their governing

assumptions and the type of roughness/contact information they require. The framework starts with classical linear friction formulations, then progresses to 2D dilation–asperity concepts and empirical JRC–JCS relationships, followed by constitutive joint models that embed nonlinearity and progressive yielding. Recent developments are captured through 3D morphology-based criteria that explicitly represent surface geometry, wall-strength contrast, matching/contact state, and scale dependence, with transitional and degradation-based models that account for shear-induced damage and roughness evolution. Finally, emerging machine-learning and data-driven approaches are summarized as complementary tools for prediction when high-resolution surface/monitoring data are available.

4.1. Linear Friction Models

The simplest representation of shear strength is the linear Mohr–Coulomb criterion [96–98]. In its basic form, shear strength τ is related to normal stress by Equation (13):

$$\tau = c + \sigma_n \tan\varphi \quad (13)$$

where φ is the friction angle of the rock surface, which is a material property related to surface hardness, mineralogy, and morphology. It is often measured by sliding one rock block on another and corresponds to the slope of the failure envelope. The parameter c is the cohesion, representing shear resistance at zero normal stress. For clean, unbonded joints, cohesion is effectively zero.

For rock joints, parameters for the Mohr–Coulomb criterion are typically determined from direct shear test results. In reality, shear strength does not increase indefinitely linearly with normal stress. Instead, the contribution of roughness diminishes at high normal stress as asperities crush or shear off. Thus, while simple, the model tends to under-predict shear strength at low normal stress. Later, Newland and Alley [99] later highlighted that shear strength in granular materials depends not only on the intrinsic frictional properties, but also on the average deviation of particle displacements relative to the applied shear direction. By conceptualizing the sliding surface as a plane with interlocked sawtooth irregularities, they formulated Equation (14), which laid the groundwork for subsequent shear strength models:

$$\tau = \sigma_n \tan(\varphi_b + i) \quad (14)$$

where φ_b is the basic friction angle, representing the friction angle of intact rock without any asperity and the inherent frictional resistance of the rock surface. i is a geometric angle representing the average inclination of asperities relative to the shear plane. This angle contributes to shear strength by causing dilation as the joint surfaces ride up over each other.

In summary, the linear friction models provide the simplest and most transparent representation of joint shear strength, requiring only the friction angle, and in some cases, a basic geometric term. Their primary advantage is their simplicity and the fact that all parameters can be obtained from routine laboratory tests. However, they do not explicitly account for roughness-induced dilation, scale effects, or progressive asperity degradation, which limits their accuracy for rough joints, particularly under low normal stress where dilation is significant. These models are best suited for preliminary design or for smooth, planar discontinuities where roughness effects are negligible.

4.2. 2d Dilation and Asperity Models

Patton experimented with sawtooth-shaped rock specimens and observed that shear resistance depends on the interaction of joint wall friction and asperity dilation (vertical displacement). He considered two different asperity behaviors, namely sliding and shearing (Equation (15)). Sliding occurs along the intact asperity when effective normal stresses are low, and in this condition, dilation equals to the angle of sawtooth joints ($d = \tan i$).

Beyond a certain level of normal stress, intact asperities are sheared off, resulting in zero dilation. Patton introduced the residual frication angle and an apparent cohesion that does not exist physically. Thus, choosing the appropriate equation depends on the magnitude of the effective normal stress (Figure 9):

$$\begin{cases} \tau = \sigma_n \tan(\phi_b + i) & \textit{For low normal stress} \\ \tau = \sigma_n \tan\phi_r + c_a & \textit{For high normal stress} \end{cases} \quad (15)$$

where c_a is the apparent cohesion due to asperities, representing the shear strength intercept that may appear if the high-normal-stress line is extrapolated. Patton's model is essentially an adaptation of the Mohr–Coulomb criterion to include joint roughness. In reality, the transition from dilation to asperity failure is gradual, rather than abrupt, because real joint surfaces have asperities of varying sizes and strengths that progressively break with increasing σ_n. Patton's model assumes uniform asperity angle and regular spacing, which are oversimplifications for natural joints. Furthermore, after asperities are sheared off under high normal stress, the resulting wear debris can act as a lubricant, reducing interlocking between joint surfaces and causing the shear strength to fall below the level predicted by the basic friction angle, often referred to as the pure friction line. This degradation mechanism, which reflects progressive surface smoothing and reduced frictional resistance, is not captured by Patton's simplified two-line model.

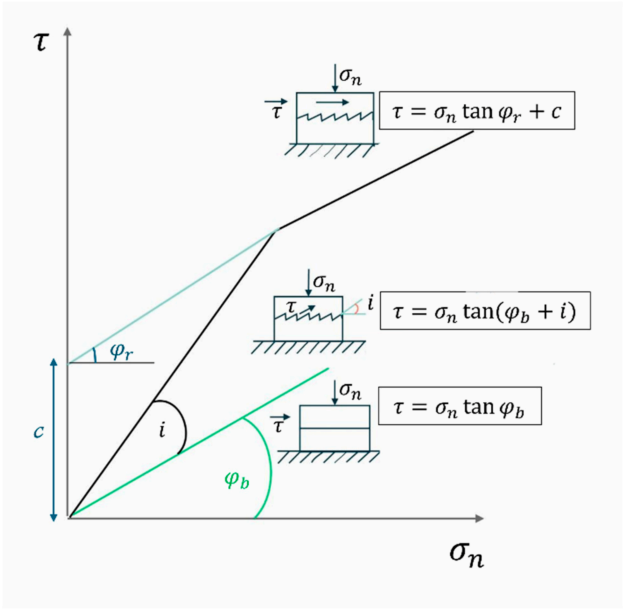

Figure 9. Bilinear envelope for multiple inclined surfaces (adapted from [17]).

Subsequent models retain Patton's basic concept but replace the sharp kink by the continuous degradation of asperity-induced dilation as normal stress or displacement increases.

Schneider modified Patton's criterion by making the mobilized dilation angle a decaying function of normal stress [100]. He proposed that the effective asperity angle i_{mob} decreases exponentially as σ_n increases according to $i_{mob} = i_0 e^{-\beta\sigma_n}$. The initial asperity angle, denoted as i_0, characterizes the inclination of sawtooth-shaped or irregular asperities on a rock joint. It is most commonly obtained through high-resolution profilometry or 3D laser scanning of the joint surface. The resulting surface profile is analyzed using geometric fitting or Fourier analysis to extract average inclination angles. For simplified sawtooth joints, direct geometric measurement is sufficient, whereas natural joints may require extracting inclination from digital elevation models (DEMs). β is a constant controlling the decay rate. Physically, the parameter β captures how quickly asperity-induced dilation is lost under pressure or sliding. In practice, β can be determined by calibrating the model

against laboratory shear tests on the joint surface, matching measured reductions in dilation angle or peak strength with increasing normal load. It can be related to surface morphology and material brittleness (e.g., rougher or more brittle joints tend to exhibit larger β). The final criterion proposed by Schneider is expressed as Equation (16):

$$\tau = \sigma_n \tan\left[\varphi_b + i_0 e^{-\beta\sigma_n}\right] \tag{16}$$

Schneider also introduced a more geometrically detailed version of the peak shear strength (Equation (17)):

$$\tau = \sigma_n \cdot \tan\left(\varphi_r + \tan^{-1}\left(\frac{\Delta h_0 e^{-k\sigma_n}}{\Delta s}\right)\right) \tag{17}$$

where φ_r is the residual friction angle, which can be obtained after significant shearing has occurred. Δh_0 is the initial asperity height, Δs is the asperity base length, and k is the exponential decay constant for asperity height. The ratio ($\frac{\Delta h_0 e^{-k\sigma_n}}{\Delta s}$) represents a mobilized dilation slope. In practice, k is calibrated by combining surface profiling to determine initial and post-shear asperity heights with incremental shear tests. A larger k denotes faster asperity removal (brittle behaviour), while a smaller k corresponds to gradual wear (more ductile behaviour). The degradation of asperity height often follows an exponential trend ($\frac{A}{A_0} = e^{-k\Delta u}$), where A_0 and A are the initial and post-shear asperity heights and Δu is shear displacement.

In contrast to the preceding formulations, which describe asperity degradation primarily through evolution laws for friction or dilation angles, Ladanyi and Archambault proposed a more explicitly mechanics-based criterion in which the shear resistance of a joint with triangular asperities is derived from force and energy considerations. Their model decomposes the total shear force into work against the normal force due to dilation, friction along the dilating surfaces (dilatancy friction), basic friction that would act in the absence of dilation, and resistance associated with shearing through asperities. On this basis, and using Rowe's stress–dilatancy framework, they introduced the *sheared area ratio* a_s, defined as the fraction of the joint area over which asperities are sheared off rather than sliding. At low normal stress, $a_s = 0$, and the response is governed entirely by sliding with dilation; at high normal stress, $a_s \to 1$, and asperities are fully destroyed. The resulting shear strength can be written in the generic form of Equation (18):

$$\tau = (1 - a_s)\, \sigma_n \tan(\varphi_b + i_{\text{mob}}) + a_s\, \tau_i \tag{18}$$

where i_{mob} is the mobilised dilation angle, and τ_i is the shear strength of the intact asperity material, related to its cohesion c_i and friction angle φ_i. The first term represents sliding with dilation over intact asperities, whereas the second term represents shearing through asperities. The sheared area ratio is further expressed as a function of normal stress and an *interlocking factor* η, which measures how well opposing asperities fit together:

$$\eta = 1 - \frac{\Delta x}{\Delta L} \tag{19}$$

where Δx is the shear displacement and ΔL is the asperity length in the shear direction. Although physically transparent, the model requires several geometric and material parameters that are difficult to determine for irregular natural joints, and its direct application generally necessitates simplification or extensive calibration.

To obtain a more tractable form suitable for engineering calculations, Saeb [19] proposed a simplified modification of the Ladanyi–Archambault model, focusing on stress–dilatancy relations and replacing the total shear force by the force required for sliding over asperities. Their peak shear strength criterion is written as Equation (20):

$$\tau_p = \sigma_n \tan[(\varphi_b + i_p)(1 - a_s)] + a_s S_r \tag{20}$$

where i_p is the peak dilation angle, a_s is the sheared area ratio, and $(1 - a_s)$ is the fraction of the joint area over which dilation is mobilised. S_r denotes the asperity shear strength, commonly approximated as the intact rock shear strength. Both a_s and i_p are expressed as functions of the applied normal stress through power laws, as shown in Equations (21) and (22):

$$a_s = 1 - (1 - \frac{\sigma_n}{\sigma_T^n})^{k_1} \tag{21}$$

$$\tan i_p = (1 - \frac{\sigma_n}{\sigma_T^n})^{k_2} \tan i_0 \tag{22}$$

where σ_T^n is the transitional normal stress beyond which no further dilatancy occurs, and k_1,k_2 are empirical exponents (often taken as 1.5 and 4.0 based on limited experimental data). Although the Saeb criterion can provide acceptable estimates of peak shear strength, it retains several important limitations. It is derived for idealised sawtooth profiles, σ_T^n, k_1 and k_2 must be obtained by back-analysis, and the asperity shear strength is often overestimated by assuming it equals the intact rock strength. A more physically consistent expression for the transitional shear stress σ_T^S, incorporating both cohesion and friction of the asperity material, is given by Equation (23):

$$\sigma_T^S = c + \sigma_T^n \tan \varphi_b \tag{23}$$

which explicitly recognises that asperity failure involves shearing of a rough cohesive–frictional material rather than a purely frictional interface.

In summary, the 2D dilation and asperity models introduced the critical concept that shear strength is not solely a function of friction, but also of the geometric interlocking of asperities and its progressive loss with increasing normal stress or shear displacement. The Patton model provided the first bilinear representation of this behavior, distinguishing between sliding and shearing regimes. Subsequent models by Schneider, Ladanyi-Archambault, and Saeb improved upon Patton by replacing the abrupt transition with continuous degradation functions, incorporating stress-dependent dilation, and explicitly partitioning the joint surface into sliding and sheared areas. These models offer greater physical realism than linear friction models and can capture the nonlinearity of the failure envelope. Their main limitations are the reliance on idealized asperity geometries, the difficulty of determining key parameters (e.g., transitional stress, sheared-area ratio) for natural joints, and the absence of explicit 3D morphology representation. They remain most suitable for joints with regular or well-defined surface geometries, such as sawtooth profiles or regularly undulating surfaces.

4.3. Empirical JRC–JCS Criteria (Barton–Bandis)

Barton introduced an empirical non-linear criterion for continuous joints using field-measured joint properties. Based on extensive direct shear tests on natural joints, he showed that normal stress level and joint roughness strongly influence failure mode. The original Barton criterion is written as Equation (24) [101]:

$$\tau = \sigma_n \tan (\phi_b + JRC \log_{10} (\frac{JCS}{\sigma_n})) \tag{24}$$

where JRC is the joint roughness coefficient (commonly varying between 0 and 20 and estimated by comparing joint profiles with standard JRC charts, and JCS is the joint wall compressive strength, determined from Schmidt hammer rebound tests or uniaxial compression tests on small specimens of the wall rock. In practice, JRC and JCS can be obtained from field and laboratory measurements without performing shear tests on each joint.

Barton and Choubey later developed the Barton first non-linear strength criterion for rock joints based on their direct shear test results for 130 samples of variably weathered rock joints, leading to Equation (25) [7]:

$$\tau = \sigma_n \tan\left(\phi_r + JRC \log_{10}\left(\frac{JCS}{\sigma_n}\right)\right) \quad (25)$$

where ϕ_r is the residual friction angle of the joint walls, essentially the basic friction angle measured on a smooth saw-cut surface. They suggested Equation (26) to obtain the residual friction angle:

$$\phi_r = (\phi_b - 20) + 20(r/R) \quad (26)$$

where r is the actual joint roughness at sample scale and R is a reference roughness profile. At small scales ($r \approx R$), roughness is fully mobilized and $\varphi_r \approx \varphi_b$; at larger scales ($r < R$), effective roughness is reduced and ϕ_r decreases accordingly.

The Barton–Bandis criterion has been widely adopted in rock engineering practice and is among the most frequently cited joint shear strength models [11,41,102–104]. It offers a practical way to incorporate field measurements, including roughness profiles through JRC and hardness tests through JCS, into peak shear strength prediction, and it implicitly accounts for scale and weathering effects via these indices. Nevertheless, a number of studies have pointed out important limitations. Because the original formulation was calibrated mainly on well-mated joints, it can overestimate shear strength for mismatched or poorly mated surfaces where the real contact area is significantly reduced [43,104]. Estimation of JRC is largely subjective, typically relying on visual comparison with standard charts, and may fail to capture complex or heterogeneous surface morphologies [13,43]. The functional form is also valid only within a restricted stress range: when σ_n approaches or exceeds JCS, the criterion may produce nonphysical predictions, whereas behaviour at very low σ_n remains poorly constrained due to limited experimental data [41]. In addition, the model predicts only peak strength and does not explicitly describe dilation or post-peak stress–displacement response, which limits its use as a constitutive law in numerical analyses. Finally, JRC is inherently direction-dependent, since roughness steps and striations vary with the direction of shearing. This directional character is not a limitation per se, but rather an indication that JRC must be estimated in conjunction with the joint orientation and along the kinematical line of sliding-shearing, rather than being treated as a single orientation-independent scalar [102].

Zhao proposed the JRC–JMC criterion as a modification of Equation (25) to reduce the overestimation of shear strength for poorly matched joints, leading to Equation (27) [43]:

$$\tau = \sigma_n \tan\left(\phi_r + JRC \cdot JMC \log_{10}\left(\frac{JCS}{\sigma_n}\right)\right) \quad (27)$$

where JMC is a joint matching coefficient ($0 < JMC \leq 1$) that quantifies how well the two surfaces fit. JMC is measured from contact mapping or profile comparison; when $JMC = 1$, the original Barton model is recovered. A minimum JMC of 0.3 is recommended to reflect that even poorly mated joints can mobilize some roughness. However, these criteria still compress complex, anisotropic, and scale-dependent surface topography into one or two scalar parameters, and do not explicitly distinguish between different orders of roughness or contrasts in wall strength. With the advent of high-resolution 3D surface scanning and more advanced image-processing techniques, a new generation of criteria has therefore focused on directly exploiting full 3D morphology, incorporating scale effects, and more recently, accounting for wall-strength contrast and multi-order roughness. These developments are examined in the following section.

In summary, the JRC–JCS family represents the most widely used empirical approach in engineering practice, primarily because it relies on field-measurable indices (JRC and JCS)

and explicitly incorporates both surface roughness and wall strength in a single nonlinear envelope. The original Barton and Barton–Choubey criteria provided a practical framework that remains a standard in rock engineering. Subsequent modifications, such as Zhao's JRC–JMC criterion and He et al.'s displacement-dependent degradation model, extended the original formulation to account for joint mismatch and progressive roughness loss during shearing, respectively. The main advantages of this family are its simplicity, its basis on extensive experimental databases, and its direct applicability using field tools such as Schmidt hammer and profile comparators. However, the estimation of JRC remains subjective unless supported by objective 3D measurements, and the criteria do not explicitly distinguish between different roughness scales or account for anisotropy beyond a single directional estimate. They also do not represent the full stress–displacement response, focusing primarily on peak strength. These models are most reliable when JRC and JCS are determined from site-specific calibration rather than from generic charts.

4.4. Constitutive Joint Models

While Schneider expressed the loss of dilation as a function of normal stress, Plesha [105] adopted a similar degradation concept but formulated it within a plasticity framework and linked it directly to shear displacement. In his model, the mobilized dilation angle is assumed to decay exponentially with accumulated shear displacement δ, following $i(\delta) = i_0 \exp(-\beta\delta)$. Substituting this evolution law into a Mohr–Coulomb-type expression gives the mobilized shear strength as Equation (28):

$$\tau = \sigma_n \tan(\varphi_b + i(\delta)) = \sigma_n \tan(\varphi_b + i_0 \exp(-\beta\delta)) \quad (28)$$

At small displacements, $i(\delta) \approx i_0$ and the envelope approaches a Patton-type peak strength. As δ increases, $i(\delta)$ progressively decays and the response tends towards a purely frictional state governed by φ_b, thereby reproducing the transition from dilative peak to residual conditions in a continuous manner. In practice, i_0 and β are obtained by fitting Equation (30) to measured shear stress–displacement curves from direct shear tests on a given joint surface. Because the degradation law is embedded in the yield function, the model can be implemented as a constitutive relation in numerical codes and is capable of reproducing both pre-peak hardening due to dilation and post-peak softening caused by asperity degradation, rather than merely predicting a single peak strength.

In a similar spirit to Plesha's displacement-based degradation of dilation, Cundall proposed the continuously yielding joint (CYJ) model as a constitutive extension of Patton's concept for implementation in distinct- and finite-element codes [106]. In this formulation, asperity degradation is represented through an evolution law for the mobilized friction angle φ_m, which is treated as a state variable that decays with accumulated plastic shear displacement u_s^p:

$$\varphi_m = (\varphi_m^{(i)} - \varphi_r) \exp(-\frac{u_s^p}{R}) + \varphi_r \quad (29)$$

The shear strength criterion at any stage of shearing is then expressed as Equation (30):

$$\tau = \sigma_n \tan[(\varphi_m^{(i)} - \varphi_r) \exp(-\frac{u_s^p}{R}) + \varphi_r] \quad (30)$$

where $\varphi_m^{(i)}$ is the initial friction angle, including the contribution of asperity-induced dilation, and R is a characteristic displacement that controls the rate of asperity wear. For small u_s^p, the full asperity effect is mobilised and $\varphi_m \approx \varphi_m^{(i)}$. As plastic shear displacement accumulates, φ_m decays progressively towards φ_r, and the associated dilation angle decreases in a consistent manner. The CYJ model therefore reproduces a smooth transition from peak to residual strength, as well as hysteresis and progressive damage under cyclic loading, and is widely used as a practical joint law in numerical rock-mechanics simulations.

These criteria delineate a coherent progression from linear frictional behaviour to two-dimensional descriptions in which dilation, asperity shearing, and roughness degradation are represented through explicit geometric angles, stress–dilatancy relations, and evolution laws. These models have been instrumental in clarifying the mechanical roles of basic friction, dilation, and asperity failure, and they provide closed-form or constitutive relations that can be implemented in numerical analyses. At the same time, their reliance on idealized sawtooth profiles, a limited set of angular parameters, and empirically calibrated degradation functions restricts their ability to represent the multi-scale, anisotropic, and imperfectly matched nature of natural rock joints. Many parameters cannot be measured directly on real surfaces. These limitations motivated subsequent approaches in which roughness and joint-wall strength are characterized by measurable indices or full 3D surface descriptors rather than assumed profiles, as discussed in the next sections.

In summary, constitutive joint models represent a significant step forward from peak-strength-only criteria by embedding degradation and dilation evolution directly into a plasticity or state-variable framework that can reproduce the entire shear stress–displacement response, including pre-peak hardening, peak, post-peak softening, and residual strength. The Plesha model introduced a displacement-based degradation of dilation, while the Cundall continuously yielding joint model defined a smooth decay of mobilized friction with plastic shear displacement, making both suitable for numerical implementation in distinct-element and finite-element codes. The later model by Gui et al. further linked degradation explicitly to measured 3D surface damage and contact evolution, providing a direct connection between morphology and constitutive behavior. The main advantages of these models are their ability to simulate progressive failure and cyclic loading, and their compatibility with numerical analysis. Their limitations include the need for extensive calibration data, the difficulty of determining state-variable parameters for natural joints, and the fact that they do not offer a closed-form peak-strength expression for hand calculations. These models are best suited for advanced numerical analyses where the full stress–displacement path is required.

4.5. 3d Morphology-Based Models (Identical Wall Strength)

4.5.1. Identical Wall Strength

The development of high-resolution 3D surface scanning and numerical modelling has enabled a new class of joint shear strength criteria in which roughness is represented by quantified three-dimensional descriptors rather than a single scalar index such as JRC. These models aim to capture directional roughness, matching condition and multiscale geometry, and to embed these features in semi-empirical or mechanics-based peak shear strength formulations.

A seminal 3D morphology-based criterion was proposed by Grasselli, who used laser scanning to discretize joint surfaces into small triangular facets and to characterise each facet by its dip and azimuth with respect to a prescribed shear direction [11]. For a given shear direction, each facet is associated with an apparent dip angle θ^*, defined as the component of its slope in the shear direction. A value of $\theta^* = 0$ corresponds to a facet parallel to the shear plane, whereas large θ^* values identify steep asperities opposing the shear direction and thus are capable of providing strong mechanical interlocking. In this framework, the joint surface is described by the maximum apparent dip θ^*_{max} and by the cumulative area A_θ of facets with $\theta^* > \theta$, normalised by the total joint area A_0. Using these descriptors, Grasselli proposed the empirical peak shear strength criterion in Equation (31):

$$\tau = \sigma_n \tan[\varphi_b + (\frac{\theta_{\max}}{C})^{1.18\cos\alpha}]\{1 + \exp[-\frac{\theta_{\max}}{9A_0C}\frac{\sigma_n}{\sigma_t}]\} \quad (31)$$

where φ_b is the basic friction angle, C is a roughness parameter related to the distribution of apparent dip angles, α is a geometric factor, σ_n is the normal stress, A_0 is the total potential contact area, and σ_t is the tensile strength of the joint-wall rock. Microscopic observations of sheared joints indicated that asperity failure is dominated by tensile cracking rather than purely compressive crushing, which motivated the use of σ_t to normalise the normal stress in the exponential term. In this way, the criterion attempts to combine normal stress, joint-wall tensile strength, and 3D surface morphology in a single expression for peak shear strength.

Although the Grasselli criterion represented a major step towards using full 3D topography in joint shear strength modelling and has been shown to fit the original database of 37 natural and synthetic joints reasonably well, several important limitations have been identified. First, Equation (32) is essentially empirical and lacks a rigorous mechanical derivation. The functional forms and exponents are obtained by statistical fitting rather than from explicit energy or force balance. Second, the model does not explicitly separate the contributions of dilation and asperity shear-off, which limits its usefulness for constitutive modelling and for analysing post-peak behaviour. Third, it does not strictly satisfy basic physical boundary conditions. For example, as $\sigma_n \to 0$, the derivative $d\tau_p/d\sigma_n$ tends to $2\tan\left[\varphi_b + \left(\theta_{\max}/C\right)^{1.18\cos\beta}\right]$ instead of the commonly accepted $\tan\left[\varphi_b + \left(\theta_{\max}/C\right)^{1.18\cos\beta}\right]$. Additionally, for smooth planar joints ($\theta_{\max} = 0$), Equation (31) reduces to $\tau_p = 2\sigma_n \tan\varphi_b$ rather than $\tau_p = \sigma_n \tan\varphi_b$, indicating that the formulation is not appropriate for planar discontinuities. Finally, because C cannot be zero, the model cannot be directly applied to idealised sawtooth joints or to other limiting geometries.

Despite these shortcomings, Grasselli's work provided a crucial conceptual and methodological foundation. It demonstrated that peak strength can be related directly to measurable 3D surface statistics and highlighted the central role of the tensile failure of steep asperities. Most subsequent 3D criteria either refine this empirical structure or seek to overcome its limitations by introducing more consistent dilatancy laws, scale dependence, joint-wall strength contrast, and multi-order roughness descriptors.

Building directly on Grasselli's formulation, Cottrell proposed a modified 3D morphology-based shear strength criterion in which the roughness parameter C is shifted to $C + 1$ and the exponent on the apparent dip term is generalised to an empirical parameter B [107]. The peak shear strength is expressed as Equation (32):

$$\tau = \sigma_n \tan\left[\varphi_b + \left(\frac{\theta_{\max}}{C+1}\right)^{B}\right]\left\{1 + \exp\left[-\frac{\theta_{\max}}{C+1}\,\frac{\sigma_n}{9A_0\sigma_t}\right]\right\}. \quad (32)$$

Here, $\theta_{\max}$ is the maximum apparent dip, A_0 is the total potential contact area, σ_t is the joint-wall tensile strength, and B is an empirical fitting parameter, initially taken as a constant $B = 1.15$. Subsequent applications showed that assuming a constant B leads to systematic overestimation of the peak shear strength for some surfaces, in some cases by nearly a factor of two, particularly for smoother joints where the model tends towards $\tau_p \approx 2\sigma_n \tan\varphi_b$ instead of the correct $\tau_p = \sigma_n \tan\varphi_b$ limit for planar discontinuities. Moreover, Cottrell's calibration relied primarily on tensile (artificial) joints, whose sharp roughness and strong interlocking tend to produce higher strengths than natural joints, further contributing to overestimation.

To alleviate the sensitivity of the Cottrell criterion to measurement resolution, Tatone and Grasselli re-examined the exponent B by varying the point spacing l of the surface measurements from 0.044 to 4 mm and carrying out six shear tests on joint replica samples of identical size. Their analysis showed that B decreases weakly with increasing point spacing

relative to specimen length L, and they proposed the following resolution-dependent relation as Equation (33):

$$B = 1.69\left(\frac{l}{L}\right)^{0.057} \tag{33}$$

This modification improves consistency between predictions and tests by recognising that apparent roughness depends on how finely the surface is sampled. However, the revised criterion still inherits the planar-joint inconsistency in the smooth limit and remains biased by the predominance of tensile joints in the calibration database. The model therefore provides a useful empirical refinement of Grasselli's structure, but it does not fully resolve the fundamental issues identified for Equation (31).

In parallel, Tang et al. [108] proposed a new peak shear strength model that retains a Mohr–Coulomb form while incorporating 3D roughness descriptors and tensile strength. Based on 130 experimental shear tests reported in the literature on induced discontinuities in six rock types and on fracture replica samples, they expressed peak shear strength as Equation (34):

$$\tau = \sigma_n \tan\left(\varphi_b + 9\, l^{0.1}\, \frac{A_0\theta_{\max}}{1+C}\, \frac{\sigma_t/\sigma_n}{1+\sigma_t/\sigma_n}\right), \tag{34}$$

where l is the point spacing of the surface measurements, $A_0\theta_{\max}/(1+C)$ is a combined 3D roughness descriptor, and σ_t is the tensile strength. This formulation is attractive because it embeds modern 3D morphology metrics into a linear Mohr–Coulomb envelope, which is convenient for practical design and numerical implementation. However, when assessed against the compiled database, the Tang et al. [108] criterion was found to overestimate peak shear strength by roughly 40% on average. This discrepancy is attributed primarily to two factors. First, many of the underlying datasets involve tensile (artificial) joints that are systematically rougher and stronger than natural joints, biasing the regression. Second, the model includes the sampling interval l but not the actual joint dimensions, so it captures one aspect of scale (measurement resolution) without representing geometric scale effects associated with joint length and waviness. Thus, while the Tang et al. [108] model is notable for explicitly linking a large 3D data compilation to a Mohr–Coulomb-type expression, which practitioners often favour for its simplicity, the magnitude of the overestimation indicates that joint behaviour remains intrinsically nonlinear and that a single linear approximation, even enriched with 3D morphology terms, has fundamental limitations.

Xia et al. [70] proposed a three-dimensional roughness-based peak shear strength criterion formulated explicitly in Mohr–Coulomb form. The peak shear stress is written as Equation (35):

$$\tau_p = \sigma_n \tan(\varphi_b + \delta_{n,peak}) \tag{35}$$

where σ_n is the normal stress, φ_b is the basic friction angle obtained from direct shear tests on flat replicas, and $\delta_{n,peak}$ is the peak dilatancy angle. To remove the subjectivity of JRC and to use a fully 3D roughness description, $\delta_{n,\mathrm{peak}}$ is expressed as a rational function of quantified surface parameters derived from Grasselli and Egger's morphology indices. Discretizing the joint surface into triangular facets yields several parameter: the normalized area A_0 corresponding to $h_{\max} = 0$, the maximum apparent dip $h_{\max}$ in the shear direction, the roughness parameter C describing the distribution of apparent dips, and the uniaxial tensile strength σ_t. The proposed dilatancy function is expressed as Equation (36):

$$\delta_{n,peak} = \frac{4A_0}{h^*_{max}(C+1)}\left[1 + exp\left(-\frac{1}{9A_0}h^*_{max}(C+1)\frac{\sigma_n}{\sigma_t}\right)\right] \tag{36}$$

This equation links the evolution of dilatancy to both normal stress and quantified 3D roughness. Substituting this dilatancy expression into the Mohr–Coulomb framework gives the final peak shear strength criterion as Equation (37):

$$\tau_p = \sigma_n \tan\left[\varphi_b + \frac{4A_0}{h^*_{max}(C+1)}\left[1 + exp\left(-\frac{1}{9A_0}h^*_{max}(C+1)\frac{\sigma_n}{\sigma_t}\right)\right]\right] \quad (37)$$

This functional form is constructed to satisfy physically meaningful boundary conditions for the dilatancy angle. As $\sigma_n \to 0$, $\delta_{n,\text{peak}}$ tends to the initial dilatancy angle whereas as σ_n approaches a critical stress, $\delta_{n,\text{peak}}$ approaches a critical dilatancy angle. When the surface becomes perfectly smooth ($h_{\max} = 0$), the roughness term vanishes, and the criterion correctly reduces to $\tau_{\text{peak}} = \sigma_n \tan\phi_b$. In this way, the Xia et al. [70] model maintains an intuitive Mohr–Coulomb structure, incorporates fully quantified 3D roughness and tensile strength, and mathematically corrects the smooth-joint and formulation limitations of earlier Grasselli-type criteria.

Beyond geometrically similar joints with identical wall strengths, subsequent 3D morphology-based criteria have focused on two key issues of the scale dependence of roughness descriptors and shear strength, and interfaces where the two joint walls have markedly different strengths. The following contributions address these aspects within Grasselli-type and Patton/Barton-type frameworks.

Jang and Jang [109] addressed both the nonlinearity of the τ–σ_n relation and the subjectivity of JRC for unfilled joints under the CNL conditions. Using 20 replica joints cast in three plaster types, they showed that peak shear stresses are well-described by a power-law relation in Equation (38):

$$\tau_p = A\ \sigma_n^B \quad (38)$$

where A and B are empirical coefficients that were subsequently given clear physical meaning.

To replace JRC with an objective roughness descriptor, they introduced a directional 1D roughness measure based on the RMS slope computed only over asperities opposing the shear direction. The RMS first derivative evaluated for positive gradients is denoted as Z_2^+ and was found to correlate strongly with the power-law coefficient $A (R^2 > 0.94)$. A corresponding joint roughness angle is then defined as Equation (39):

$$\varphi_J = \tan^{-1}\left(Z_2^+\right) \quad (39)$$

which is dimensionally similar to JRC-derived roughness angles and can be interpreted as an estimate of the dilation angle.

Following Barton's idea that the total friction angle at peak can be decomposed into basic friction, roughness-induced dilation, and a shear-off component, Jang and Jang defined the total friction angle at $\sigma_n = 1$ MPa as Equation (40):

$$\varphi_A = \varphi_b + \varphi_J + \varphi_{sn}, \quad (40)$$

where φ_b is the basic friction angle of a planar joint, φ_J is the new objective roughness angle, and φ_{sn} represents the additional contribution from the shearing of asperities. The resulting shear strength criterion can be written compactly as Equation (41):

$$\tau_p = \sigma_n^B\ \tan\left(\varphi_b + \varphi_J + \varphi_{sn}\right), \quad (41)$$

with $\varphi_J = \tan^{-1}\left(Z_2^+\right)$ obtained from 1D surface profiles parallel to the shear direction and φ_{sn} calibrated from test data as a function of roughness and joint-wall strength. The proposed equation reproduces nonlinear failure envelopes with less than 10% deviation from the measured peak shear stresses, whereas the JRC–JCS criterion with measured φ_b can deviate

by more than 35% for the same dataset. The criterion is recommended for unfilled replica joints under CNL with $\sigma_n \lesssim 4$ MPa, total friction angles $\varphi_A < 80°$, and a reduction factor $0.72 < B < 0.92$, and requires further validation for natural rock joints.

Later, Kumar and Verma [110] investigated the anisotropic shear behaviour of rough rock joints by performing 144 CNL direct shear tests on three joint replica surfaces (JR1–JR3) sheared in twelve directions (every 30° from 0° to 330°) under normal stresses $\sigma_n = 0.25$–1.5 MPa. The replicas were cast in a cement–sand–water mixture with uniaxial compressive strength $\sigma_c \approx 40.8$ MPa, tensile strength $\sigma_t \approx 4.36$ MPa, and basic friction angle $\varphi_b \approx 35.8°$. Surface geometry was measured using a 3D non-contact profiler and processed for each shear direction to obtain two directional roughness indices of the maximum asperity angle $\theta_{\max}$ and the average asperity angle θ_A. The tests revealed pronounced anisotropy, with peak shear strength maximised when shearing against steep asperities (large $\theta_{\max}$, θ_A) and becoming more isotropic as σ_n increased. The peak shear strength is expressed as Equation (42):

$$\tau_p = \sigma_n \tan \varphi_j \tag{42}$$

where the peak friction angle φ_j is decomposed into a basic friction term and two roughness-related components, as expressed in Equation (43):

$$\varphi_j = \varphi_b + d_{na}(\sigma_n/\sigma_c, \theta_A) + S_p(\sigma_n/\sigma_c, \theta_{\max}). \tag{43}$$

Here, d_{na} denotes the actual peak dilation angle and S_p is the shear-off contribution. The dilation angle d_n is first obtained from the shear path relative to the joint mean plane and then corrected for the mean-plane inclination α, giving $d_{na} = d_n \pm \alpha$. Experimental data show that d_{na} decreases exponentially with increasing stress ratio σ_n/σ_c; an exponential function is calibrated by taking θ_A as the upper bound as $\sigma_n/\sigma_c \to 0$. The shear-off component S_n was back-calculated from a Barton-type decomposition $\varphi_j = \varphi_b + d_{na} + S_n$ and found to follow a power-law dependence on σ_n/σ_c. By correlating the power-law parameters with $\theta_{\max}$, a predictive function $S_p(\sigma_n/\sigma_c, \theta_{\max})$ is obtained. The resulting anisotropic criterion is shown in Equation (44):

$$\tau_p = \sigma_n \tan[\varphi_b + d_{na}(\sigma_n/\sigma_c, \theta_A) + S_p(\sigma_n/\sigma_c, \theta_{\max})] \tag{44}$$

Equation (45) explicitly separates dilation, governed mainly by the directional average asperity angle θ_A, from shear-off, governed by the directional maximum asperity angle $\theta_{\max}$. At low σ_n/σ_c the dilation term dominates, whereas at higher σ_n/σ_c, the shear-off term becomes increasingly important. The model predicts peak strength with mean square error decreasing from about 14% at $\sigma_n = 0.25$ MPa to about 5% at $\sigma_n = 1$ MPa, and correctly reduces to the basic friction law $\tau_p = \sigma_n \tan\varphi_b$ when $\theta_A = 0$, meaning for smooth planar joints. Companion expressions were also proposed for the peak shear displacement d_p and shear stiffness K_{ss}, with d_p proportional to $\theta_{\max}$ and inversely proportional to φ_j and $K_{ss} \approx \tau_p/d_p$, both independent of JRC.

Building on this explicit separation of directional dilation and asperity shear-off, and the demonstration that anisotropy diminishes as confinement increases, subsequent work further probed the underlying failure mechanism of the controlling asperities and reformulated Patton-type expressions by tying the evolution of dilatancy to tensile cracking and to objective, shear-direction-dependent roughness metrics, as exemplified by Zhang et al. [111]. Their study is based on CNL direct shear tests on artificial tensile joints replicated from three sandstone joints (groups JA, JB, JC), tested under normal stresses $\sigma_n = 0.5$–3 MPa. Microscopic examination of the sheared surfaces showed that damage is concentrated in steep asperities facing the shear direction and is governed predominantly by tensile cracking, accompanied by local crushing and rotation, rather than purely by compressive failure. The

mass of detached fragments was observed to increase with both σ_n and joint roughness, underscoring the importance of tensile strength σ_t and shear-direction-dependent roughness in controlling the failure mechanism.

To capture anisotropy in a simple yet objective way, Zhang et al. [111] introduced two directional profile-based metrics. The first is a revised RMS asperity angle $\tan^{-1}(Z_{2r})$, where Z_{2r} is computed from slopes of the asperities that face the shear direction (positive gradients only). The second is a maximum contact coefficient C_m, defined as the ratio between the cumulative length of active asperities along the profile and the projected profile length L_0. Both $\tan^{-1}(Z_{2r})$ and C_m change when the joint is sheared in opposite directions (0° versus 180°), thereby capturing directional roughness effects that are invisible to scalar JRC.

The core of the model is a new expression for the peak dilatancy angle i_p. Test data showed that i_p decreases with increasing σ_n and depends on the normalised tensile strength σ_t/σ_n. A negative-exponential function was proposed that satisfies the boundary conditions $i_p \to i_0$ as $\sigma_n \to 0$ and $i_p \to 0$ as $\sigma_n \to \infty$. In the final formulation, both the initial dilatancy i_0 and the decay parameter are expressed in terms of $\tan^{-1}(Z_{2r})$ and C_m in Equation (45):

$$i_p = f(\tan^{-1}(Z_{2r}), C_m, \sigma_n/\sigma_t) \tag{45}$$

The peak shear strength is written in Patton-type form as Equation (46):

$$\tau_p = \sigma_n \tan(\varphi_b + i_p) = \sigma_n \tan[\varphi_b + f(\tan^{-1}(Z_{2r}), C_m, \sigma_n/\sigma_t)] \tag{46}$$

where φ_b is the basic friction angle of the planar joint. Substituting the dilatancy model into this framework yields a nonlinear, direction-dependent failure envelope. The criterion reproduces the experimental data with an average error of about 6% and outperforms other criteria [7,82,100,112] for the same joints, primarily because it relies on objective, direction-sensitive roughness descriptors rather than subjective JRC. It is applicable to fresh, mated, unfilled joints under CNL conditions where asperity damage is dominated by tensile failure.

To extend beyond these quasi-static, direction-dependent studies, later work shifted toward Barton-type frameworks that can more directly accommodate engineering-scale effects (joint length and undulation amplitude) and additional loading-path dependencies such as shear-rate sensitivity, as developed by Zheng et al. [113]. Their model was calibrated against a series of servo-controlled direct shear tests on granite discontinuities with regular sawtooth first-order roughness and superimposed second-order random roughness, tested at different specimen lengths and low shear rates in a shear box with an internal length up to 1 m.

The starting point is a modified Barton–Bandis expression in which the peak shear strength is written as Equation (47):

$$\tau_p = \sigma_n \tan[\varphi_b + JRC_n (\frac{V_0}{V})^M \log_{10}(\frac{JCS_n}{\sigma_n})] \tag{47}$$

where σ_n is the applied normal stress, φ_b is the basic friction angle of a planar discontinuity, V is the imposed shear rate, V_0 is a reference rate (taken as 1 mm/s), M is a rate-sensitivity exponent, and JRC_n, JCS_n are size-dependent roughness and joint-wall strength indices at the actual discontinuity length L_n. The scale effect is introduced by relating JRC_n and JCS_n to reference values JRC_0 and JCS_0, defined at a standard profile length L_0 and undulation amplitude h_0. Using empirical relationships derived from Barton's standard profiles, the normalized indices are expressed as Equations (48) and (49):

$$JCS_n = JCS_0 (\frac{L_n}{L_0})^{-0.03\ JRC_0} \tag{48}$$

$$JRC_n = JRC_0\left(\frac{L_n/h_n}{L_0/h_0}\right)^{-0.02\ JRC_0}, \tag{49}$$

where JRC_0 is back-calculated from the undulation angle $\beta_{100\%}$ of the sawtooth profile using Barton's original correlation, $L_0 = 100$ mm, and h_0 is the maximum undulation amplitude of the reference profiles. In this formulation, increasing joint length and/or decreasing relative undulation amplitude systematically reduces JRC_n and JCS_n, consistent with the experimentally observed tendency for larger discontinuities to exhibit lower apparent roughness and weaker average joint-wall strength. To represent the rate effect in a transparent manner, Zheng et al. [113] recast the criterion in terms of a rate-dependent friction angle φ_v. Rearranging the peak-strength expression yields Equation (50) and consequently Equation (51):

$$\arctan\left(\frac{\tau_p}{\sigma_n}\right) - JRC_n \log_{10}\left(\frac{JCS_n}{\sigma_n}\right) = M \log_{10}\left(\frac{1}{V}\right) + \varphi_b \tag{50}$$

$$\varphi_v = M \log_{10}\left(\frac{1}{V}\right) + \varphi_b \tag{51}$$

Here, φ_v can be interpreted as the mobilised friction angle at a given shear rate; it increases approximately linearly with $\log_{10}(1/V)$, and the exponent M quantifies the degree of rate strengthening. A larger M corresponds to a stronger increase in peak shear strength as the shear rate decreases. In practice, φ_v is first obtained from the experimental τ_p–σ_n data via the left-hand side of the rearranged equation, and then regressed against $\log_{10}(1/V)$ to determine M and φ_b.

The experimental programme encompassed granite discontinuities with lengths between 200 and 1000 mm, undulation amplitudes of approximately 3–23 mm, and shear rates from quasi-static to 1 mm/s under normal stresses of 100 and 200 kPa. The results indicate that for a given geometry and normal stress, peak shear strength increases as shear rate decreases, with a pronounced rate effect up to about 0.2 mm/s and a weaker effect at higher rates. For a given rate, specimens with larger undulation amplitudes (higher JRC_n) systematically exhibit higher peak strength. At larger specimen lengths ($\approx$1 m), the size effect substantially reduces JCS_n and moderates the rate strengthening compared with shorter specimens. Microscopic observations show that at these relatively low normal stresses, asperity degradation is governed mainly by abrasive wear and micro-fragmentation along first- and second-order irregularities, consistent with a friction–dilation mechanism rather than gross compressive crushing.

Overall, the Zhang et al. [113] criterion can be regarded as a scale- and rate-augmented Barton-type model in which 3D morphology is condensed into length- and amplitude-dependent indices JRC_n and JCS_n, and low shear-rate strengthening is captured through a simple logarithmic rate term embedded in a rate-dependent friction angle φ_v. Validation against the granite test data demonstrates good agreement for low shear rates (up to $\approx$1 mm/s) and low normal stresses, with systematic improvement over classical static JRC–JCS formulations that neglect size and rate effects. The model remains constrained by its calibration on regular sawtooth granite joints under modest σ_n and by its reliance on Barton's standard profiles through JRC_0 and JCS_0; nevertheless, it provides a useful intermediate step between purely static 3D morphology criteria and fully dynamic constitutive laws.

Zheng et al. [113] improved classical JRC–JCS practice by adding size and shear-rate effects, but still treated the joint walls as effectively mated, so the roughness contribution is not explicitly reduced when contact is lost due to dislocation/mismatching. Tang and Wong [13] filled this gap by introducing a joint contact-state coefficient that scales the roughness term as a function of 3D morphology and normalized offset, enabling peak strength to be predicted when mismatch progressively degrades interlocking. They extended an earlier 3D roughness-based criterion for perfectly matching joints to explicitly capture the influence

of dislocation (mismatching) along the shear direction. Replica joints were prepared from five natural granite surfaces and cast in three different plaster mixes (Groups A, B, C) to vary compressive and tensile strength and basic friction. Surface morphology was quantified using the Tatone and Grasselli [10] 3D descriptor, and mismatching was simulated by imposing a horizontal offset d along the shear direction, up to a normalised dislocation $j = d/L \leq 0.05$, where L is the specimen length. CNL direct shear tests for $\sigma_n \approx 0.2{-}3$ MPa showed a systematic reduction in peak shear strength with increasing dislocation, with the effect diminishing as normal stress increased. The starting point is their basis criterion for perfectly matching joints, written as Equation (52):

$$\tau_p^{\text{match}} = \sigma_n \tan \varphi_b + G(A_0, \theta_{\max}, C, \sigma_n/\tau_t) \tag{52}$$

where φ_b is the basic friction angle, τ_t is a tensile-strength scale, and $G(\cdot)$ is a roughness-dependent term expressed in terms of 3D parameters A_0, $\theta_{\max}$, C, and σ_n/τ_t. To extend this to mismatched joints, they introduced a joint contact state coefficient JCC(R_{3D},j) that scales the roughness contribution as a function of both 3D roughness and normalised dislocation, as shown in Equation (53):

$$\tau_p^{\text{unmatch}} = \sigma_n \tan \varphi_b + \text{JCC}(R_{3D}, j)\ G(A_0, \theta_{\max}, C, \sigma_n/\tau_t), \tag{53}$$

where R_{3D} denotes the selected 3D roughness metric and $j = d/L$. The JCC is defined via a simple hyperbolic function calibrated against the test data. It equals 1 for perfectly mated joints and decreases rapidly with increasing dislocation when the surface is rough while remaining close to 1 for relatively smooth joints. The functional form contains no arbitrary fitting constants. For example, the constant 8 appearing in the denominator of the hyperbola is chosen to be consistent with the peak dilation predicted by the underlying matching-joint criterion. The final form predicts peak strength of un-matching joints with a reported coefficient of determination $R^2 \approx 0.92$, and provides a physically interpretable link between 3D roughness, degree of mismatch, and the degradation of shear strength.

Tang et al. [24] complemented this by proposing a more general hyperbolic CNL envelope in which peak strength is governed directly by 3D morphology and tensile-strength–normalised stress, improving portability across rock types and measurement resolutions.

They proposed a general empirical criterion for the peak shear strength of fresh, unfilled joints under CNL conditions, emphasising that 3D roughness metrics are more appropriate than 2D profiles or scalar JRC, and that rock tensile strength σ_t is the key material parameter controlling asperity damage at low normal stress, rather than JCS or σ_c. Using an extensive database of more than 130 direct shear tests on different rock types, they showed that the additional friction angle $\varphi_a = d_n + s_n$ (dilation plus sheared component) is best represented as a hyperbolic function of normal stress.

Employing a 3D roughness metric that accounts for asperity shape and potential contact area, and normalising stress by τ_t (a tensile-strength scale), they expressed the failure envelope in the generic form of Equation (54):

$$\tau_p = \tau_t\, F(R_{3D}, \sigma_n/\tau_t) \tag{54}$$

where F is a hyperbolic function of the normalised normal stress and the 3D roughness descriptor R_{3D}. This envelope can be re-written in a Mohr–Coulomb-like form as Equation (55):

$$\tau_p = c_t(R_{3D}, \sigma_n/\tau_t) + \sigma_n \tan\varphi_t(R_{3D}, \sigma_n/\tau_t), \tag{55}$$

where the apparent cohesion c_t and tangent friction angle φ_t are derived analytically from the hyperbolic relation. Sensitivity analyses indicate that rougher joints yield larger c_t and φ_t; both φ_t and the sheared component s_n decrease towards φ_b as σ_n increases; and the shear-off component reaches a maximum near $\sigma_n \approx \tau_t$ and decreases beyond this point.

A key contribution of Tang et al. [24] is explicit treatment of the sampling effect. As the sampling interval l increases, computed roughness decreases. To generalise the criterion to different measurement resolutions, they introduced a sampling coefficient m, linked to l via a power law, and incorporated it into the 3D roughness term. The generalised criterion yields average prediction errors of about 15–18% over the database and is applicable to rock types with σ_c/σ_t in the range 7–25. In this sense, the model provides a bridge between earlier Grasselli-type envelopes and more recent hyperbolic, tensile-strength-normalised formulations.

Subsequent work, such as the dilation-evolution model of Ding and Li [114], further developed this direction by refining how the mobilized dilation angle evolves with stress and displacement. The degradation and transitional-stress models discussed above explicitly link peak shear strength to the evolution of dilation and/or mobilised roughness, but they do not yet embed a full 3D description of joint morphology in the strength law. Ding and Li [114] addressed this gap by proposing a peak shear strength criterion for rock joints under CNL that combines Grasselli-type 3D surface descriptors with a mechanically interpretable evolution law for the peak dilation angle. Their stated aim was to obtain an integrated criterion that represents joint roughness through measurable 3D parameters, describes how this roughness is progressively mobilised and degraded with increasing normal stress, and retains a Mohr–Coulomb-type structure suitable for engineering use.

Starting from Grasselli's framework, the joint surface is discretised into triangular facets and characterised by the apparent dip angle θ* of each facet in the shear direction. Rather than collapsing this information into a single scalar roughness index, Ding and Li [114] used the distribution of θ* to define a 3D roughness measure representative of *first-order* morphology along the shear direction. In parallel, they adopted the sheared-area concept of Saeb [19], in which the joint area is partitioned into a dilating (sliding) part and a sheared-off part, and the peak dilation angle is expressed as a function of normal stress and surface geometry. On the basis of direct shear tests on 3D-scanned rough joints, they observed an approximately linear decrease in a mobilised roughness parameter with increasing σ_n, indicating that the effective steepness of the engaged facets reduces in a systematic way as normal stress grows.

Ding and Li [114] then formulated a dilation-evolution law in which the peak dilation angle i_p is written as a bounded function of the normalised normal stress (e.g., $\frac{\sigma_n}{\sigma_c}$ or $\frac{\sigma_n}{\sigma_T}$) and of the mobilised 3D roughness index. The function is constructed to satisfy the physically required limits: $i_p \to i_0$ (a roughness-controlled upper bound derived from the θ* distribution) as $\sigma_n \to 0$, and $i_p \to 0$ as σ_n approaches a transitional stress at which asperities are fully sheared off. In other words, the non-linearity of the τ–σ_n envelope is entirely embedded in the stress dependence of i_p, while the 3D roughness parameters enter through i_0 and the mobilisation law.

Substituting this dilation function into a Mohr–Coulomb-type expression leads to a peak shear strength criterion of Patton form, which can be written generically as Equation (56):

$$\tau_p = \sigma_n \tan[\phi_b + i_p(\sigma_n, R_{3D})] \quad (56)$$

where ϕ_b is the basic friction angle of a planar joint and R_{3D} is a roughness descriptor derived from the apparent-dip distribution (and implicitly scale-dependent through sampling length and facet size). In contrast to Grasselli's original empirical fit, the new criterion was built so that the contribution of roughness is explicitly tied to a 3D morphological measure, the evolution of peak dilation with stress follows an interpretable degradation law, and the resulting shear strength envelope respects Mohr–Coulomb-type behaviour in the appropriate limits (smooth joint; fully degraded roughness). Calibration against direct shear tests on laboratory joints showed that the model captures both the non-linear τ–σ_n

response and the observed reduction in dilation with increasing σ_n more consistently than previous 3D criteria based solely on θ* or JRC-like indices.

Within the overall framework of this review, Ding and Li's contribution can therefore be seen as a bridge between 3D morphology-based criteria and the degradation/transitional-stress family. 3D roughness is described through apparent-dip statistics in the spirit of Grasselli, while the stress-dependent mobilisation and loss of roughness are treated through a dilation-evolution law similar in spirit to Saeb [19] and Li et al. [12]. This makes the criterion particularly attractive for applications where both scale-dependent 3D surface geometry and progressive dilation loss with increasing normal stress must be represented in a single, mechanically interpretable peak strength formulation.

Although Ding and Li [114] integrated 3D morphology with a stress-dependent dilation evolution law, their formulation does not explicitly quantify how the governing roughness descriptors (and thus peak strength) vary systematically with specimen size and measurement resolution. This limitation motivated subsequent scale-dependent 3D criteria, such as that of Azinfar et al. [14], which embed the joint length and sampling spacing directly into the roughness term within a Mohr–Coulomb framework. They selected three natural joints with distinct geometries and produced artificial replicas from these surfaces. Direct shear tests were performed on specimens of different sizes, while the joint surfaces were characterised using 3D scanning. Instead of relying on a single roughness index, they combined several parameters to represent both first-order waviness and second-order unevenness, namely Grasselli's $\theta_{max}/(C+1)$, the root mean square height (RMS) and the centre-line average (CLA) of the surface profile.

On this basis, Azinfar et al. [14] proposed a peak shear strength criterion that retains a Mohr–Coulomb form but uses a composite 3D roughness–scale function inside the friction angle, as shown in Equation (57):

$$\tau_p = \sigma_n \tan\left[\varphi_b + 7\left(\frac{\text{CLA}\ \theta_{max}}{\text{RMS}\ (C+1)}\frac{L}{l}\right)^{0.2}\frac{\sigma_t/\sigma_n}{7(\sigma_t/\sigma_n)^5(\text{CLA/RMS})^{0.6}+(\sigma_t/\sigma_n)}\right] \quad (57)$$

where $\theta_{max}/(C+1)$ is Grasselli's roughness parameter, RMS and CLA are the second- and first-order height descriptors of the surface, σ_t is the Brazilian tensile strength of the rock, l is the measurement point spacing (resolution) and L is the joint length (geometric scale). Symbols φ_b, σ_n, σ_t, and C are used as in previous sections.

The criterion is conceptually attractive because it maintains the familiar Mohr–Coulomb structure, embeds multiple 3D descriptors to separate waviness and small-scale roughness, and introduces scale explicitly through the ratio L/l. From a practical standpoint, all required roughness parameters can be obtained from a single 3D scan, so in principle, the shear strength at different scales can be estimated once σ_t and the scanning resolution are known. However, the model was calibrated using only three joint geometries and a fixed measurement resolution, so further validation is needed to fully assess its robustness when both joint size and resolution vary and when a wider range of lithologies and surface morphologies are considered.

4.5.2. 3d Wall-Strength Contrast Models

While the above criteria implicitly assume identical joint-wall materials, many engineering interfaces are formed between materials with markedly different strengths, such as hard–soft rock contacts or concrete–rock interfaces. Ghazvinian et al. [103] extended the mechanics-based family of Patton-type criteria to such different joint-wall compressive strength (DDJCS) systems. Using regular sawtooth joints cast between a high-strength concrete block and plaster mortars with different uniaxial compressive strengths, they showed that the peak behaviour of DDJCS differs systematically from that of joints with identical wall strengths, asperity failure is controlled by the weaker wall, and using a single JCS in

Barton's JRC–JCS criterion tends to misrepresent both peak dilation and peak strength in the medium normal-stress range.

To capture these observations, Ghazvinian et al. [103] first proposed an explicit dilation–normal stress relationship in which the UCS of the weaker wall, σ_c, appears as the normalising parameter. The peak dilation angle is expressed as a bounded rational function of σ_n normalised by σ_c, as shown in Equation (58):

$$i(\sigma_n) = i_0 \frac{(\sigma_c/\sigma_n)^a}{b + (\sigma_c/\sigma_n)^a} \tag{58}$$

where σ_c is the uniaxial compressive strength of the soft side, σ_n is the applied normal stress, i_0 is the steepest asperity angle on the joint surface, and a and b are regression parameters that control the intensity and rate of dilation decay with increasing stress. This function satisfies the physically meaningful limits $i \to i_0$ as $\sigma_n \to 0$ (sliding up intact asperities) and $i \to 0$ as $\sigma_n \to \infty$ (fully crushed asperities). By plotting measured peak dilation against σ_c/σ_n, they obtained a unique curve dependent only on surface topology and identified a strong power-law relation between a and b, allowing b to be expressed as $b = c\,a$, with c interpreted as an irregularity parameter linked to the distribution and spacing of steep asperities. Inserting this dilation law into Patton's expression leads to a peak shear strength criterion for DDJCS, as shown in Equation (59):

$$\tau_p = \sigma_n \tan\left[\varphi_b + i_0 \frac{(\sigma_c/\sigma_n)^a}{b + \left(\frac{\sigma_c}{\sigma_n}\right)^a}\right] \tag{59}$$

where φ_b is the basic friction angle of the soft wall or interface material. In this form, the surface topology is encapsulated in the three coefficients i_0, a(or a and c), which can be related to statistical roughness descriptors, and the controlling wall strength enters naturally through the ratio σ_c/σ_n. Validation against CNL tests on various DDJCS specimens showed that this criterion reproduces both the smooth decay of dilation with increasing normal stress and the measured peak shear strengths more accurately than Barton's JRC–JCS equation.

In a subsequent study combining the DDJCS test data with PFC3D simulations, Ghazvinian et al. [115] demonstrated that asperity failure is dominated by tensile cracking rather than compressive crushing. This finding has important implications for strength normalisation. Barton's JRC–JCS formulation, which normalises σ_n by the compressive strength JCS (or σ_c), systematically underestimated peak dilation and peak strength for DDJCS, with predictions around 80% of the measured values. To address this, Ghazvinian et al. [116] replaced the compressive-strength normalisation by the intact tensile strength σ_t of the weaker wall and derived a simplified Barton-type peak shear strength relation, as shown in Equation (60):

$$\tau_p = \sigma_n \tan\left[\varphi_b + a \frac{\sigma_t/\sigma_n}{1 + \sigma_t/\sigma_n}\right] \tag{60}$$

where a (here used as a dimensionless roughness coefficient) is fitted from data and σ_t is the tensile strength of the soft wall. This form recovers φ_b at very high normal stress or very low roughness and approaches the asperity angle as $\sigma_n \to 0$. The tensile-based criterion showed good agreement with the DDJCS experiments and was also validated against Grasselli's natural limestone and sandstone joint data for identical joint-wall strength cases over a wide range of σ_n/σ_c and σ_c/σ_t.

Taken together, the Ghazvinian et al. [115] models can be viewed as Patton/Barton-type criteria with rigorously defined, stress-dependent dilation functions and physically motivated normalisation by the strength of the weaker wall. They bridge classical bilinear concepts and modern dilation-evolution approaches and are particularly relevant for design problems involving concrete–rock contacts, hard–soft rock interfaces, and other DDJCS configurations where asperity degradation is governed by tensile failure of the soft wall.

Building on the tensile-failure insight of Ghazvinian et al. [115] for DDJCS interfaces and on the 3D roughness framework of Grasselli-type models, Tang et al. [116] proposed a three-dimensional peak shear strength criterion explicitly tailored to matched discontinuities with different joint-wall strengths (DDJSs). Most classical criteria (Patton, Ladanyi–Archambault, Barton–Bandis) were calibrated for discontinuities with identical joint-wall strengths (DIJSs) and generally tend to overestimate peak shear strength, whereas using those of the weaker wall underestimates it. To isolate the effect of wall-strength contrast from morphology, they prepared specimens in which the two joint walls shared an identical 3D geometry but different material properties. A reference rough joint surface was obtained and then replicated into pairs of rock (or mortar) materials with different tensile and compressive strengths, allowing the DIJS and DDJS configurations to be tested under comparable normal stresses. Direct shear tests under CNL were used to quantify how the peak shear strength and failure mode evolve as the strength contrast between the two walls increases.

Three ingredients underpin the proposed criterion. First, the joint surface morphology is characterized by a set of 3D roughness descriptors derived from high-resolution surface scanning, in the spirit of Grasselli-type facet statistics. These parameters quantify the distribution of steep, load-bearing asperities and their potential contact areas in the chosen shear direction. Second, a dimensionless joint-wall strength difference coefficient (JSC) is introduced to condense the compressive or tensile strengths of the two walls into a single index that measures how dissimilar the wall materials are. JSC → 0 corresponds to DIJS, while larger values indicate increasing contrast. Third, the peak shear strength is expressed in a normalized form that uses the tensile strength of the weaker wall as the governing material scale, reflecting the predominance of tensile cracking in asperity failure. In compact form, their final DDJS criterion can be written as a normalized relationship of the type as shown in Equation (61):

$$\frac{\tau_p}{\sigma_{t,\mathrm{weak}}} = F\left(R_{3\mathrm{D}}, \frac{\sigma_n}{\sigma_{t,\mathrm{weak}}}, \mathrm{JSC}\right) \tag{61}$$

where $R_{3\mathrm{D}}$ denotes the chosen 3D roughness metric (or combination of metrics), $\sigma_{t,\mathrm{weak}}$ is the tensile strength of the weaker wall, and $F(\cdot)$ is a hyperbolic-type function constructed to satisfy physically meaningful boundary conditions (smooth transition from rough-controlled to strength-controlled failure as σ_n increases and as JSC varies).

The normalized function is factorized into a term that captures the effect of wall-strength contrast and a roughness function $f(x)$ that embeds the 3D morphology. When JSC → 0, the model reduces to a DIJS-type 3D criterion similar to the earlier Xia–Tang form. As JSC increases, the contribution of the weaker wall becomes dominant, and the envelope progressively departs from the DIJS prediction. Model parameters are obtained by fitting to the DDJS experimental database, and the authors provide practical procedures for determining the 3D roughness metrics and computing JSC from laboratory tests on the two wall materials. Evaluation against a broad set of DIJS and DDJS data showed that the proposed criterion achieved relatively low average relative errors and smaller scatter than existing DIJS-based equations applied to DDJS, while preserving a Mohr–Coulomb-like structure that can be implemented in engineering calculations.

In summary, the 3D morphology-based criteria represent the most significant advance in recent decades, moving beyond subjective JRC estimates and idealized profiles to directly quantify joint surface geometry using high-resolution scans. The Grasselli-type framework, and its subsequent extensions by Cottrell, Tatone, Xia, Tang, and others, established that peak shear strength can be related to measurable 3D statistics such as apparent dip distributions, potential contact area, and tensile-strength-normalized stress. These models capture directional roughness anisotropy, scale effects through sampling resolution, and in more recent formulations, wall-strength contrast (DDJCS/DDJS) and joint mismatch (JCC). Their

primary advantage is objectivity and the ability to represent complex, anisotropic surfaces that cannot be described by a single scalar JRC. Their limitations include the requirement for high-resolution 3D scanning equipment, the need for specialized data processing, and the fact that many formulations remain empirical and require calibration against direct shear tests. Additionally, they are not yet standard in routine practice. These criteria are most valuable for research, for critical projects where high-quality surface data are available, and for validating simpler models.

4.6. Transitional and Degradation-Based Models

All of the above 3D criteria treat surface roughness as fixed for a given joint, even though asperities are progressively damaged during shear and the true contact area evolves. Gui et al. [117] addressed this limitation by developing an empirical constitutive model in which both basic friction and effective asperity angle evolve with normal stress and shear displacement, informed directly by repeated 3D scans of degrading surfaces. Replica joints were prepared from granite blocks (three rough surfaces J1–J3 and one planar surface J0) using a plaster mixture with $\varphi_b \approx 38^\circ$, $\sigma_c \approx 24.5$ MPa, and $\sigma_t \approx 1.26$ MPa. For each rough joint and normal stress level, direct shear tests were repeated and interrupted at different displacements (peak, 3 mm, 8 mm, 12 mm). Before and after each test, the surfaces were scanned with a 3D topography system, allowing the authors to quantify asperity height deviation $z_{\text{deviation}}$, joint aperture evolution and changes in contact area.

Tests on the planar joint showed that the basic friction angle decreases with increasing σ_n and can be described by Equation (62) to determine a variable basic friction angle, where a and b are empirical constants:

$$\varphi_b(\sigma_n) = a\log\sigma_n + b \tag{62}$$

Using the full 3D degradation information, a representative asperity angle was defined as equivalent effective asperity dipping angle d_e, which depends on both σ_n and shear displacement δ, capturing material removal, smoothing, and gouge accumulation along the sliding path. Joint aperture and real contact area were computed from aligned pre- and post-shear surfaces, linking mechanical response directly to evolving geometry. These components were combined into a shear-stress model of the following form, yielding Equation (63):

$$\tau(\sigma_n,\delta) = \sigma_n\tan[\varphi_b(\sigma_n) + d_e(\sigma_n,\delta)] \tag{63}$$

where both φ_b and d_e evolve with σ_n and degradation state. The model reproduces the multi-stage shear response (pre-peak hardening, peak, post-peak softening and residual) and explicitly links each stage to measured surface damage and contact evolution. As such, it provides a 3D morphology-based constitutive law that is particularly suited for the numerical modelling of jointed rock masses where progressive roughness degradation and aperture change are important. Together, the contributions by Tang and Wong [13], Tang et al. [24] and Gui et al. [117] illustrate a progression from static 3D morphology descriptors toward criteria and constitutive models that incorporate contact mismatch, sampling effects, and explicit roughness evolution, paving the way for the transitional-stress and degradation-focused models discussed in the next section.

With these advances establishing how 3D morphology, contact conditions, and progressive wear can be incorporated into peak-strength formulations, the next generation of models focuses on formalizing degradation through transitional-stress concepts, meaning enforcing physically meaningful limits on dilation loss and sheared-area evolution. This

approach is exemplified by Li et al.'s revision of the Saeb framework [12]. They introduced the dimensionless relative normal stress (Equation (64)):

$$\xi = \frac{\sigma_n}{\sigma_T^n} \tag{64}$$

where σ_T^n is the transitional normal stress at which asperity dilation vanishes, and the joint surface becomes fully sheared. The evolution of both the sheared-area ratio a_s and the peak dilation angle i_p is constrained between two limiting states. At $\sigma_n = 0$: $a_s = 0$, $i_p = i_0$ (all asperities participate in dilation, none are sheared off). At $\sigma_n = \sigma_T^n$: $a_s = 1$, $i_p = 0$ (all asperities are sheared off and no dilation occurs). To enforce these limits smoothly, they expressed the sheared-area ratio as a sinusoidal function of ξ, as shown in Equation (65):

$$a_s(\xi) = \sin(\frac{\pi}{2}\frac{\sigma_n}{\sigma_T^n}) \quad \text{or, equivalently, } a_s(\xi) = \frac{1-\cos(\pi\xi)}{2} \tag{65}$$

so that a_s increases monotonically from 0 to 1 as σ_n approaches σ_T^n. The associated peak dilation angle is linked to the initial asperity angle i_0 by Equation (66):

$$\tan i_p = [1 - a_s(\xi)]\tan i_0 \tag{66}$$

which guarantees that i_p decays smoothly from i_0 to 0 over the same stress interval. Substituting these expressions into the Saeb peak-strength equation yields a transitional-stress-controlled shear strength of the form shown in Equation (67):

$$\tau_p = \sigma_n \tan[(\varphi_b + i_p)(1 - a_s)] + a_s\,\tau_T \tag{67}$$

where φ_b is the basic friction angle and τ_T is the shear strength at the transitional state, commonly expressed in terms of cohesion c, σ_T^n, and φ_b. In this formulation, the first term represents frictional and dilatancy resistance over the unsheared portion $(1 - a_s)$ of the joint, whereas the second term accounts for the shear-off resistance over the sheared portion a_s.

A key advantage of Li et al.'s framework is that all input parameters are, at least in principle, measurable without performing direct shear tests on rough joints. The basic friction angle φ_b is determined from tilt or shear tests on smooth saw-cut specimens; the cohesion and compressive strength needed for τ_T follow from standard intact rock tests; and the initial asperity angle i_0 is obtained from 3D surface morphology, for example, using apparent-dip distributions or Grasselli-type parameters. The transitional normal stress σ_T^n is treated as a material parameter representing the stress level at which normal dilation ceases; Li et al. [12] suggested that it can be approximated from the uniaxial compressive strength (typically of order $0.2\,\sigma_c$) and then refined by limited calibration. Overall, the model decouples geometric roughness (through i_0 and 3D descriptors) from stress-controlled degradation (through ξ), and enforces a physically meaningful, continuous transition from a fully dilative regime to a pure sliding regime. Its main limitations are the assumption of a single effective roughness scale and a unique transitional stress, and the lack of explicit representation of environmental influences (e.g., humidity, loading stiffness, chemical weathering), all of which can significantly affect degradation in natural joints.

Whereas Li et al. [12] describe degradation as a stress-driven transition between dilation and shear-off, He et al. [118] focused on the displacement-controlled evolution of joint roughness within the JRC–JCS framework. They conducted 150 CNL direct shear tests on artificial joints manufactured with different initial roughness coefficients $JRC_{initial}$, joint wall compressive strengths (JCSs), and normal stresses σ_n. The results confirmed that the mobilized roughness decreased from its initial value toward a constant residual value as shear displacement δ increased, and that this degradation was more pronounced for higher $JRC_{initial}$, higher JCS, and higher σ_n.

On the basis of this database, He et al. [118] proposed a JRC degradation function $JRC(\delta)$ and interpreted the evolution in three stages. The first stage is an initial weakening stage associated with adjustment and minor wear. The second stage is a rapid weakening stage dominated by intense asperity damage and strength drop. The third stage is a constant (residual) stage where both morphology and strength stabilize. Mathematically, $JRC(\delta)$ is expressed by a smooth, S-shaped regression function that depends on $JRC_{initial}$, JCS, σ_n, and δ. In parallel, an empirical equation for the peak shear displacement δ_p is derived as a function of the same variables. These relations are then embedded into the classical Barton peak criterion by replacing the constant JRC with a mobilized value $JRC_{mobilized}(\delta)$, leading to Equation (68):

$$\tau(\delta) = \sigma_n \tan[\varphi_r + JRC_{mobilized}(\delta)\ \log_{10}(\frac{JCS}{\sigma_n})] \quad (68)$$

where φ_r is the residual friction angle. A piecewise formulation of $JRC_{mobilized}(\delta)$ is used for the three degradation stages, which allows the friction angle to decrease consistently with progressive surface damage. In this way, the Barton-type structure is preserved, but JRC becomes a state variable evolving with displacement, enabling the model to reproduce not only the peak strength, but also the full τ–δ response under CNL conditions.

From a practical standpoint, parameter determination remains anchored in standard measurements. $JRC_{initial}$ is obtained from 2D or 3D roughness indices (e.g., Z_2, JRC_{3D}). JCS comes from uniaxial or point-load tests, and σ_n is given by the boundary condition. φ_r is obtained from shear tests on smooth saw-cut joints. The coefficients controlling $JRC(\delta)$ and the δ_p equation are obtained by regression on the experimental database and can, in principle, be recalibrated for other rock types or joint morphologies. Comparisons with previously proposed constitutive models indicate that this degradation-driven JRC–JCS formulation reproduces measured shear stress–displacement curves more accurately and captures the influence of initial roughness and JCS on both peak and post-peak behaviour. Its main limitations are the strongly empirical nature of the regression, the reliance on artificial joints with idealized roughness, and the absence of explicit 3D morphological descriptors, even though the framework is conceptually compatible with modern 3D-based JRC evaluation. Taken together, Li et al.'s transitional-stress model and He et al.'s JRC-degradation formulation illustrate a broader trend towards criteria that couple shear strength with explicit laws for roughness and dilation evolution.

In summary, transitional and degradation-based models explicitly formalize the progressive loss of asperity contribution with increasing normal stress and shear displacement, ensuring physically meaningful limits on dilation and sheared-area evolution. The Li et al. transitional-stress model provides a continuous transition from a fully dilative regime to a pure sliding regime using a sinusoidal sheared-area function, with parameters that are, in principle, measurable without direct shear tests. The He et al. JRC-degradation model embeds an S-shaped evolution of JRC with displacement into the Barton framework, enabling reproduction of the full shear stress–displacement curve. These models bridge the gap between peak-strength criteria and fully constitutive laws. Their main advantages are their physical interpretability and their ability to capture stress-dependent and displacement-dependent degradation without requiring full 3D morphology data. Their limitations include the empirical nature of the degradation functions, the need for calibration, and the fact that they often rely on a single effective roughness scale, which may not represent multi-scale natural joints. These models are particularly suitable for engineering applications where progressive damage is relevant, such as cyclic loading or long-term stability assessments.

4.7. Machine-Learning and Data-Driven Models

Machine-learning and data-driven approaches have increasingly been explored for predicting the shear strength of rock joints. Unlike conventional empirical or semi-empirical criteria, these approaches do not necessarily prescribe the relationship between the controlling parameters and peak shear strength in advance. Instead, the relationship is inferred from experimental data using parameters such as normal stress, rock strength, joint size, roughness indices, and two- or three-dimensional surface-morphology descriptors.

These approaches range from relatively interpretable regression-based models to artificial neural networks and hybrid optimization–machine-learning methods (Figure 10). Their main advantage is the ability to represent nonlinear interactions among several mechanical and geometrical variables. However, their performance depends strongly on the size, quality, and representativeness of the training dataset, and black-box formulations generally provide less physical interpretability than conventional shear-strength criteria.

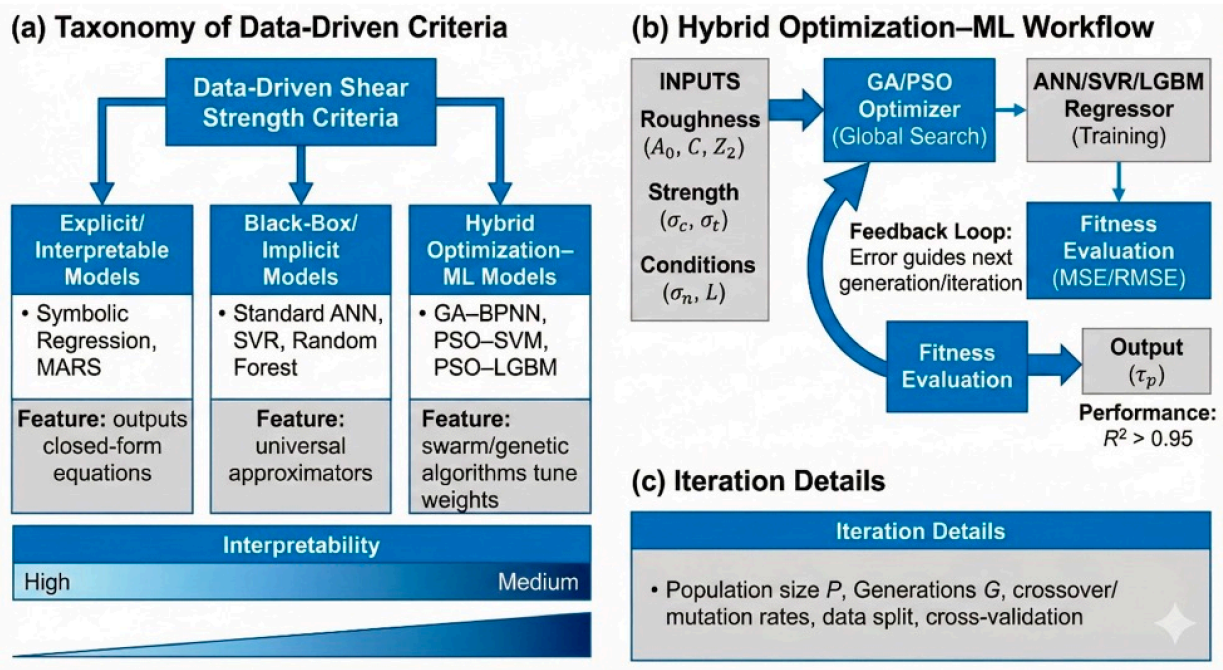

Figure 10. Schematic overview of data-driven approaches for rock-joint shear-strength prediction, including explicit, black-box, and hybrid optimization–machine-learning models.

4.7.1. Fathipour-Azar's Mars Model

A representative example of an explicit ML-based joint shear strength criterion is the multivariate adaptive regression splines (MARS) model proposed by Fathipour-Azar [119] for the peak shear strength prediction of rock joints. In MARS, the response is expressed as a sum of piecewise-linear hinge basis functions in the form of Equation (69):

$$h(x, t) = \max(0, x - t) \tag{69}$$

where t is a knot that partitions the input space into sub-domains with different linear behavior.

For rock joints, the dependent variable is typically taken as a dimensionless (normalized) peak shear strength S_p, while the predictors include both surface morphology and mechanical properties such as maximum potential contact area ratio A_0, a roughness parameter C (e.g., Grasselli-type coefficient), maximum apparent dip angle of asperities θ_{max}, normalized normal stress r_n, normalized uniaxial compressive strength r_c, and, optionally, normalized tensile strength r_t. Using an experimental database covering a wide range of

joint geometries, rock strengths and stress conditions, Fathipour-Azar [120] employed eight input variables (sampling interval, A_0, C, θ_{max} or h, basic friction angle, tensile strength, compressive strength, and σ_n) to train the model. The MARS procedure first constructs an over-complete set of candidate hinge functions $h(\cdot,\cdot)$ with different knot locations in each variable, then applies backward pruning with generalized cross-validation to obtain a parsimonious model that balances accuracy and complexity. A typical calibrated MARS-based criterion for the normalized peak shear strength can be written in the generic form of Equation (70):

$$S_p(\mathbf{x}) = a_0 + \sum_j a_j\, h\left(z_j, t_j\right) + \sum_k b_k\, z_{k,1}\, z_{k,2}\, h\left(z_{k,3}, t_{k,3}\right) \tag{70}$$

where a_0, a_j, b_k are regression coefficients, z_j are functions of the basic inputs (e.g., A_0, C, θ_{max}, r_n, r_c, r_t), and $h(\cdot,\cdot)$ is the hinge basis. In one reported form, the explicit expression reads, for example:

$$\begin{aligned} S_p(\mathbf{x}) = \; & 4.8 - 2.8\, h(A_0, 0.48) - 0.113\, h(C, 7.48) - 1.68\, h(\theta_{max}, 3) \\ & +1.33\, h(r_n, 3) - 0.0119\, h(r_c, 65) + 0.0100\, h(65 - r_c, 0) \\ & -0.00168\, C\, r_n\, h(65 - r_c, 0), \end{aligned}$$

where $r_n = \sigma_n/\sigma_c$, $r_c = \sigma_c/\sigma_{ref}$, $r_t = \sigma_t/\sigma_{ref}$ (in consistent units), and the constants are obtained from data-driven calibration.

The fixed knot values (e.g., $A_0 = 0.48$, $C = 7.48$, $r_n = 3$, $r_c = 65$) partition the parameter space into regimes with distinct linear trends and can be interpreted as thresholds beyond which changes in contact area, roughness, or strength begin to significantly modify peak shear strength. This explicit, piecewise-linear structure has two main implications. First, it defines a shear strength criterion in the same operational sense as classical equations. Given measured or computed morphology and mechanical properties, S_p and thus τ_p can be evaluated directly. Second, it provides interpretability, because each basis function corresponds to a physically meaningful regime (e.g., transition from adhesion-dominated behavior to asperity shearing at specific roughness or stress levels), in contrast to traditional black-box neural networks.

In addition to this interpretable MARS criterion, Fathipour-Azar [119] systematically compared several soft-computing models developed after 2015, including Gaussian process (GP), alternating model tree (AMT), Cubist, radial-basis-function (RBF) networks, and elastic-net regression, against conventional empirical criteria. These soft-computing models, particularly GP, AMT, and RBF, produced substantially tighter residual distributions and lower error variance than classical formulations over the calibrated domain, indicating that data-driven approaches can match or surpass the predictive performance of established shear strength criteria while offering flexible functional forms.

4.7.2. Hybrid Optimization–ANN Criteria

Hybrid optimization–artificial neural network (ANN) models represent a significant advancement in data-driven rock joint shear strength prediction, particularly through the integration of genetic algorithms (GAs) with back-propagation neural networks (BPNNs) [120,121]. These hybrid GA–BPNN models address key limitations of standalone BPNNs, notably their sensitivity to initial weight selection and tendency to become trapped in local optima during training, by exploiting the global search capability of GA to optimize the network parameters [120,122]. In rock mechanics, GA–BPNN frameworks have been widely applied in recent years to predict the peak shear strength τ_p of rock joints, using complex inputs such as surface roughness descriptors, normal stress, and joint size, which are difficult to accommodate within traditional empirical criteria like the Barton–Bandis model [121,123].

A typical GA–BPNN consists of an input layer, one or more hidden layers, and a single output neuron, mapping an input feature vector **x** to a predicted peak shear strength $\hat{\tau}_p$. For a single hidden layer with H neurons and d inputs, the forward propagation can be written as Equation (71):

$$\hat{\tau}_p = \sum_{j=1}^{H} v_j \, \phi \, (\sum_{i=1}^{d} w_{ji} x_i + b_j) + b_0 \tag{71}$$

where x_i are the input features (e.g., JRC, uniaxial compressive strength σ_c, normal stress σ_n, joint length L, and morphological parameters such as maximum potential contact area ratio A_0), w_{ji} and v_j are the weights between input–hidden and hidden–output layers, b_j and b_0 are biases, and $\phi(\cdot)$ is a nonlinear activation function (commonly sigmoid, $\phi(z) = 1/(1 + e^{-z})$ or ReLU, $\phi(z) = \max(0, z)$). Depending on the study, the network output may target τ_p directly or a normalized quantity such as $S_p = \tau_p/\sigma_n$ to promote generalization across different stress levels. Training seeks to minimize a loss function, typically the mean squared error (MSE), using gradient-based back-propagation to iteratively update the weights and biases via the chain rule.

The hybrid character arises from using a GA to optimize the initial weights $\mathrm{W} = \{w_{ji}, v_j\}$ and biases $\mathrm{b} = \{b_j, b_0\}$ before conventional back-propagation. In practice, a population of P candidate solutions is created, each chromosome being a real-valued vector of length M that encodes the flattened network parameters. For each chromosome, the BPNN is instantiated with the decoded weights and biases, trained for a limited number of epochs on the training set, and its fitness is evaluated, usually as the inverse of the validation MSE so that higher fitness implies lower prediction error. The GA then applies evolutionary operators. Selection schemes such as roulette-wheel or tournament selection preferentially retain high-fitness chromosomes. Crossover recombines pairs of parent chromosomes to produce offspring with a specified crossover probability p_c (commonly around 0.8). Mutation introduces random perturbations to selected chromosome components (for example, adding Gaussian noise with probability p_m of order 0.01) to maintain diversity and reduce the risk of premature convergence. This evolutionary cycle is iterated over G generations, typically between 50 and 200, until a stopping criterion such as stagnation of the best fitness or attainment of a prescribed maximum generation count is satisfied. The best chromosome at termination is then taken as providing near-optimal initial weights and biases, which are subsequently fine-tuned by standard gradient-based back-propagation. Hyperparameters such as population size, crossover and mutation rates and the number of generations are often tuned via grid search or additional meta-optimization. In rock joint applications, datasets usually comprise on the order of 100–500 direct shear test records, commonly partitioned into training, validation, and testing subsets (e.g., 70:15:15) with k-fold cross-validation employed to assess robustness.

Applications of GA–BPNN models in rock joint shear strength prediction have demonstrated their capability to capture strongly nonlinear interactions, including scale-dependent degradation of strength and the influence of detailed 3D roughness statistics. For example, studies such as Zhang et al. [124] developed GA–BPNN models using inputs like JRC, σ_n, σ_c and joint size L, and reported coefficients of determination R^2 exceeding 0.95 and root-mean-square errors below 0.5 MPa on test sets, clearly outperforming both standalone BPNN (with $R^2 \approx 0.85$) and empirical formulations such as Barton–Bandis (with $R^2 \approx 0.75$). The GA–BPNN framework can capture size dependence directly from the training data, avoiding the need for ad hoc scale-correction factors. In addition, GA–BPNN models have been trained using high-dimensional surface descriptors (e.g., multiscale or wavelet-based roughness features), yielding low prediction errors (e.g., mean absolute percentage errors below ~8%) and outperforming conventional support-vector regression in comparative studies. More recent hybrid workflows further couple GA–BPNN predictors with numerical

simulations (e.g., finite-element models) that account for stress-path effects and progressive asperity degradation, producing substantially lower residual variance than classical empirical criteria and improving robustness for heterogeneous conditions such as infilled or weathered joints [121]. Under such variability, GA-based initialization also reduces sensitivity to local minimum and can improve generalization by promoting diverse, well-distributed starting solutions in the network parameter space.

From a critical standpoint, GA–BPNN-based criteria offer operational utility comparable to conventional empirical equations in that once trained, they function as black-box predictors that can be embedded in design tools or numerical codes. Sensitivity analyses based on variance decomposition have shown that they can also reveal the relative importance of inputs, often highlighting normal stress as a dominant factor compared with compressive strength. However, GA–BPNN models remain implicit, and no closed-form analytical expression is available, so their physical interpretability is limited relative to explicit ML criteria such as MARS-based models. Moreover, the GA training phase can be computationally demanding and requires sufficiently rich and high-quality datasets to avoid spurious relationships, although the use of synthetic data from numerical simulations and transfer learning strategies has been proposed to alleviate data scarcity. In a review paper, GA–BPNN can thus be positioned as a central example of hybrid optimization–ML shear strength criteria, representing the evolution from early, purely data-driven ANN applications toward more sophisticated frameworks where global optimization, and in some cases, physics-based constraints, are integrated to improve both predictive performance and reliability.

4.7.3. Multi-Scale Decomposition

Complementary to the size- and rate-dependent formulation of Zhang et al. [124], Hong et al. [125] proposed a 3D morphology-based criterion that explicitly separates and quantifies the contributions of first-order waviness and second-order unevenness over a range of joint scales. Their central argument is that most existing 3D criteria (including Grasselli-type and Azinfar-type models) treat the joint surface as a single roughness entity, typically condensed into a parameter such as $\frac{\theta^*_{max}}{(C+1)}$, and therefore cannot distinguish between large-scale undulations and superimposed small-scale asperities when joint size changes.

The study focused on fresh, unfilled granite joints with pronounced two-order roughness. Three representative natural joint surfaces were selected following the ISRM recommendations, covering relatively smooth, strongly undulating, and stepped morphologies. Each natural surface was scanned using a high-resolution optical topography system and replicated at three specimen sizes (e.g., 50 × 50, 100 × 100, 200 × 200 mm) with constant measurement spacing, so that true geometrical scale (L) could be varied independently from sampling interval (l). Replica specimens were cast in a brittle cementitious material; standard laboratory tests provided uniaxial compressive strength, Brazilian tensile strength, and basic friction angle, which were later used in the shear criterion. Direct shear tests were then carried out under *CNL* over a practical range of normal stresses, giving peak shear strength, peak dilation, and post-peak response for each combination of surface, size, and σ_n.

To characterise roughness in a way consistent with this multi-scale design, Hong et al. [125] combined classical Grasselli-type descriptors with a wavelet-based decomposition. A three-dimensional scan of each surface was first processed to obtain Grasselli's apparent dip parameter $\frac{\theta^*_{max}}{(C+1)}$, together with standard altitude indices such as the root-mean-square height (*RMS*) and *CLA*. A discrete wavelet transform was then applied to decompose the surface into a long-wavelength component (primary waviness) and a short-wavelength component (secondary unevenness). The cut-off level was selected at the point where

the variance of wavelet coefficients changed slope, ensuring that first-order undulations (governing overall inclination and large steps) were separated from finer texture asperities. From these decomposed surfaces, the authors defined a set of first-order roughness parameters (based mainly on altitude and large-scale slope) and second-order parameters (based mainly on local slope and curvature) and examined how each family varies with specimen size.

The mechanical tests showed that peak shear strength and peak dilation increase systematically with both normal stress and the magnitude of first-order waviness, while the contribution of second-order unevenness is more subtle and becomes relatively more important at smaller scales. When joint size increases at fixed measurement spacing, classical scalar roughness measures fall, but the decomposed parameters reveal that much of this reduction is associated with smoothing of the large-scale waviness rather than complete loss of small-scale texture. On this basis, Hong et al. adopted a Mohr–Coulomb-type form in which peak shear strength is written as Equation (72):

$$\tau_p = \sigma_n \tan[\varphi_b + i(\sigma_n; R_1, R_2, L/l, \sigma_t/\sigma_n)] \quad (72)$$

where the peak dilation angle i(·) is explicitly modelled as a function of a first-order roughness measure R_1 (built from CLA, RMS and $\frac{\theta^*_{max}}{(C+1)}$), a second-order roughness measure R_2 (constructed from local gradient statistics of the unevenness component), the dimensionless size ratio L/l, and the stress ratio $\frac{\sigma_t}{\sigma_n}$. By expressing all additional strength beyond φ_b through i(·), the criterion remains compact while still embedding two-order roughness and scale effects.

The dilation model was constructed to satisfy standard physical limits. As $\sigma_n \to 0$, the peak dilation tends to an upper bound controlled mainly by the steepest first-order asperities, and as $\sigma_n \to \infty$, dilation tends to zero as all asperities are effectively crushed. Intermediate behaviour is described by a bounded rational-type function of $\frac{\sigma_t}{\sigma_n}$, in which the numerator is governed by a scale-dependent first-order roughness parameter and the denominator includes a stress- and roughness-dependent degradation term. Second-order roughness enters this denominator through a parameter that regulates how quickly dilation decays with increasing σ_n, so that joints with pronounced small-scale unevenness retain higher dilation at intermediate stress levels than geometrically similar but smoother joints. When this dilation function is substituted back into the Mohr–Coulomb form, the authors obtained a closed-form peak shear strength criterion that reduces to the basic friction law $\tau_p = \sigma_n \tan \varphi_b$ for smooth joints (vanishing R_1, R_2) and converges to earlier Grasselli-type expressions when second-order roughness and scale factors are neglected.

Validation against the full test matrix shows that the two-order criterion reproduces peak shear strengths across different joint sizes and morphologies with lower average error than previous 3D criteria based on a single morphology parameter. In particular, the model improves predictions for strongly stepped surfaces and for larger specimens, where earlier Grasselli- or Azinfar-type formulations tend to overestimate peak strength because they implicitly assume that all roughness scales contribute equally. At the same time, the parameter set remains accessible in practice: a single high-resolution scan provides the necessary roughness descriptors, and scale effects enter through simple dimensionless ratios. In the broader context of 3D morphology criteria, Hong et al.'s work therefore represents a move from single-index to multi-order descriptors, providing a bridge toward the degradation- and transitional-stress models discussed in the next section, where these roughness contributions are allowed to evolve with stress level and shear displacement.

A consolidated comparison of the reviewed rock-joint shear-strength criteria, including their equation mapping, derivation basis, required input parameters, and associated testing requirements, is provided in Appendix A (Table A1).

5. Romaine-IV Hydropower Case Study

5.1. Dataset and Specimen Characteristics

To assess the applicability of existing criteria for estimating shear strength, direct shear test results from the rock foundation of Hydro-Québec's Romaine-IV powerplant were analyzed. The objective was to conduct a comparative analysis using these criteria to predict joint shear strength. The analysis utilized test data from two series of rock specimens extracted via core drilling from the Romaine-IV excavation site. Specimens were tested separately at GTX Laboratory in 2017 (samples TF-BB-17-A, TF-BB-17-B, TF-BB-17-C, TF-LL-17-A, TF-MM-17-C, TF-MM-17-D, TF-MM-17-E, TF-NN-17-A, TF-PP-17-A, TF-PP-17-B, TF-PP-17-C, TF-1-A, TF-1-B, TF-1-C) and Université de Sherbrooke Laboratory in 2018 (samples CSD009, CSD0010, CSD0011, CSD0012). In total, 20 specimens underwent direct shear testing under constant load conditions following the ASTM D5607 standards, enhanced with methodological considerations recommended by ISRM [126]. Multi-stage shear testing was conducted at normal stress intervals ranging from 200 to 2500 kPa, both with and without repositioning the joints between stages.

The specimens tested by the two laboratories exhibited marked variability in geological and geometric characteristics, including sampling depth, joint aperture, degree of mineralogical alteration, and surface roughness. These differences reflect both natural heterogeneity and variations in sampling and preparation procedures. Surface roughness and joint geometry parameters were documented using laboratory reports and visual assessments, supplemented by high-resolution core photographs. Table 3 presents a comprehensive overview of these characteristics, enabling a comparison of key properties across all tested samples and highlighting the heterogeneity between the two laboratory batches.

It is important to acknowledge that the roughness characterization in this benchmark was based on visual core logging and photographic documentation available from the original site-investigation program, rather than on high-resolution optical methods such as LiDAR or SEM photogrammetry. The application of such advanced techniques would have enabled more precise and objective JRC estimation and likely improved the predictive performance of the Barton–Bandis criterion in particular. However, these measurements were not part of the original testing program, and the physical specimens were no longer available for additional scanning at the time of our study. This limitation should be considered when interpreting the comparative results, and it reinforces the broader conclusion of this review: that the practical applicability of shear strength criteria is often constrained by the quality and resolution of the input data that can be realistically obtained in engineering practice. When high-resolution surface characterization is not feasible, simpler criteria with fewer and more readily measurable parameters may offer more reliable predictions.

Table 3. Geological and structural characteristics of the tested rock joint samples.

Sample Code	Depth (m)	Joint Aperture (mm)	Joint Condition	Filling/Mineral Content	Weathering/ Alteration	JRC	Rock Type
TF-BB17-A (NAT)	12.80	42.1	Open	Oxides	Moderately weathered (Fe-oxide)	13	Anorthosite
TF-BB-17-B (NAT)	35.29	1.3	Open	Biotite	Fresh (no oxidation)	3	Anorthosite
TF-1-A (NAT)	27.85	2.0	Open	Hematite	Moderately weathered (Fe-oxide)	11	Anorthosite
TF-1-A (SAW CUT)	27.85	N/A *	Saw Cut	None	Fresh (cut surface)	1	Anorthosite
TF-1-B (NAT)	53.06	0.0	Partially Open	Biotite/Calcite	Unweathered	11	Anorthosite

Table 3. *Cont.*

Sample Code	Depth (m)	Joint Aperture (mm)	Joint Condition	Filling/Mineral Content	Weathering/ Alteration	JRC	Rock Type
TF-1-C (NAT)	56.63	0.0	Partially Open	Biotite	Fresh (no weathering)	9	Anorthosite
TF-PP-17-A (NAT)	22.17	0.0	Partially Open	Biotite/Chlorite	Slight alteration (chlorite)	5	Gabbroic Anorthosite
TF-PP-17-C (NAT)	32.58	0.0	Partially Open	Biotite	Fresh (no alteration)	9	Gabbroic Anorthosite
TF-MM-17-C (NAT)	40.46	11.6	Open	Biotite/Chlorite	Altered (chlorite-coated)	5	Anorthosite
TF-MM-17-D (NAT)	43.92	0.0	Partially Open	Chlorite/Carbonate	Altered (chlorite + calcite)	5	Anorthosite
TF-NN-17-A (NAT)	30.35	4.6	Open	Chlorite/Biotite	Altered (dike contact)	9	Anorthosite
TF-NN-17-A (SAW)	30.35	N/A	Saw Cut	None	Fresh (cut surface)	1	Anorthosite
TF-LL-17 A (NAT)	32.37	0.0	Partially Open	Biotite/Chlorite	Slight alteration (chlorite)	9	Pegmatite
TF-PP-17-B (NAT)	22.36	0.0	Partially Open	Chlorite/ Feldspar/Hematite	Moderately weathered (oxidized)	11	Gabbroic Anorthosite
TF-BB-17-C (NAT)	36.46	1.0	Open	Oxide	Moderately weathered (Fe-oxide)	9	Anorthosite
TF-PP-17-D (NAT)	32.95	5.2	Open	Biotite	Fresh (no weathering)	11	Gabbroic Anorthosite
CSD009	62.27	2.8	Open	Undetermined (grey/black)	Unknown (grey/black deposit)	5	Anorthosite
CSD010	30.12	0.0	Partially Open	Iron Oxide	Moderately weathered (Fe-oxide)	6	Anorthosite
CSD011	93.63	3.7	Open	Biotite/Chlorite/ Carbonate	Altered (chlorite +calcite)	6	Gabbroic Anorthosite
CSD012	33.10	0.0	Closed	Epidote/ Hematite/Calcite	Altered (oxidized epidote–calcite)	10	Gabbroic Anorthosite

* N/A: Not Available. A reference intact-rock UCS of 175 MPa was used for the initial Barton–Bandis calculations. This value should not be interpreted as a specimen-specific measurement of joint wall compressive strength.

5.2. Application of the Selected Criteria

Due to the practical constraints of the available site-investigation data, only three failure criteria were selected for the comparative benchmark: the Mohr–Coulomb, Patton, and Barton–Bandis criteria [109]. This selection was not arbitrary, but was guided by two primary considerations. First, these three criteria are the most widely used in engineering practice and collectively represent three widely used conceptual families among the seven families reviewed in Section 4: linear friction, asperity-based dilation, and empirical JRC–JCS formulations [127]. Second, and more importantly, all input parameters required by these models could be derived directly from the laboratory reports and core photographs available for the Romaine-IV project. In contrast, the more sophisticated 3D morphology-based and data-driven criteria reviewed earlier require high-resolution surface scans, directional roughness descriptors, or detailed contact-area measurements that were not part of the original testing program. Applying those models without such data would have required speculative assumptions, undermining the reproducibility and credibility of the comparison. The Mohr–Coulomb criterion is a well-established linear model known for its simplicity and broad applicability [128]. The Barton–Bandis criterion is widely used for its ability to incorporate roughness and wall strength under varying stress levels. The Patton criterion provides a bilinear envelope that captures dilation-dominated behavior at low normal

stress and asperity shearing at high stress. These three criteria thus offer a meaningful and practical basis for comparison, while remaining fully compatible with the actual data collected. The Mohr–Coulomb criterion defines two distinct linear failure envelopes: one corresponding to peak strength and another to residual strength. The cohesion and friction angle parameters are derived from shear stress measurements taken at peak and post-failure conditions. For the residual condition, cohesion is assumed to be zero, and the failure envelope is constrained to pass through the origin of the shear stress axis so that only the friction angle is determined. When joints are already open, cohesion is considered zero, and for curve-fitting purposes, the failure envelope is forced to pass through the point (0,0). The Romaine-IV dataset comprises 20 specimens tested under multiple normal-stress stages. Peak and post-peak responses are shown separately in the graphical comparison where relevant. For Patton's criterion, the basic friction angle is used (φ_b), measured on samples with fresh fracture surfaces. The inclination of the waviness plane was defined using the average slope angle, calculated from the ratio of vertical to horizontal displacement. In the post-failure phase, post-peak stress values were used, and a linear regression was performed without forcing the line to pass through the origin (0,0), which results in an apparent cohesion. This approach contrasts with the Mohr–Coulomb criterion, where the residual envelope is constrained to pass through the origin. In Patton's criterion, the intersection of the peak and post-peak envelopes defines the normal and shear stress values at which the failure mode transitions from peak to post-peak behavior. The transition constraint was defined by equating the Patton peak and residual expressions. The value of the transitional normal stress was calculated using Equation (73):

$$\sigma_n = \frac{c_a}{(\tan\varphi_b + i_0) - (\tan\varphi_r)} \tag{73}$$

Finally, for the Barton–Bandis failure criterion, the residual friction angle (φ_r) was considered in the formula, where again the data adjustment line crossed zero. The specimen-specific parameters used in the implementation of the Mohr–Coulomb, Patton, and Barton–Bandis criteria, including φ_b, φ_r, i_0, JRC, JCS, and the Mohr–Coulomb parameters, are provided in Supplementary Table S1. The results for all tests are presented in Figures 11–15.

$$\varphi_r + JRC * \log_{10}\frac{JCS_i}{\sigma_n} < 70° \tag{74}$$

5.3. Comparison

The comparison shows larger differences between the Barton–Bandis predictions and the project-specific Mohr–Coulomb and Patton envelopes, particularly at lower normal stresses. Because the criteria rely on different parameter-estimation procedures, these differences should be interpreted in relation to the characterization of the model inputs rather than as a direct ranking of criterion performance. The Patton criterion yields results very similar to those of the peak Mohr–Coulomb criterion. After transitioning from the peak to the residual state, the Patton criterion results closely align with those of the residual Mohr–Coulomb criterion in most tests.

To compare the results of several criteria, Equation (75) was used. The shear resistance of each criterion was compared with that of the Mohr–Coulomb criterion. For the Patton failure criterion, the difference before the transition stress was calculated using the Mohr–Coulomb peak criterion and after the transition stress using the Mohr–Coulomb residual criterion. In specific tests where the apparent cohesion is zero, the difference was determined using the residual strength of the Mohr–Coulomb criterion. Consequently, this difference

becomes zero because the Mohr–Coulomb residual failure criterion coincides with the Patton failure criterion.

$$Difference = \frac{(\tau_{Cri} - \tau_{M\&C})}{\tau_{M\&C}} * 100 \quad (75)$$

$_{M\&C}$: Mohr–Coulomb failure criterion;

$_{Cri}$: Barton–Bandis or Patton failure criterion.

The results, as shown in Figures 16–19, indicate that the difference is more pronounced for low normal stress levels and reduces as stress levels increase.

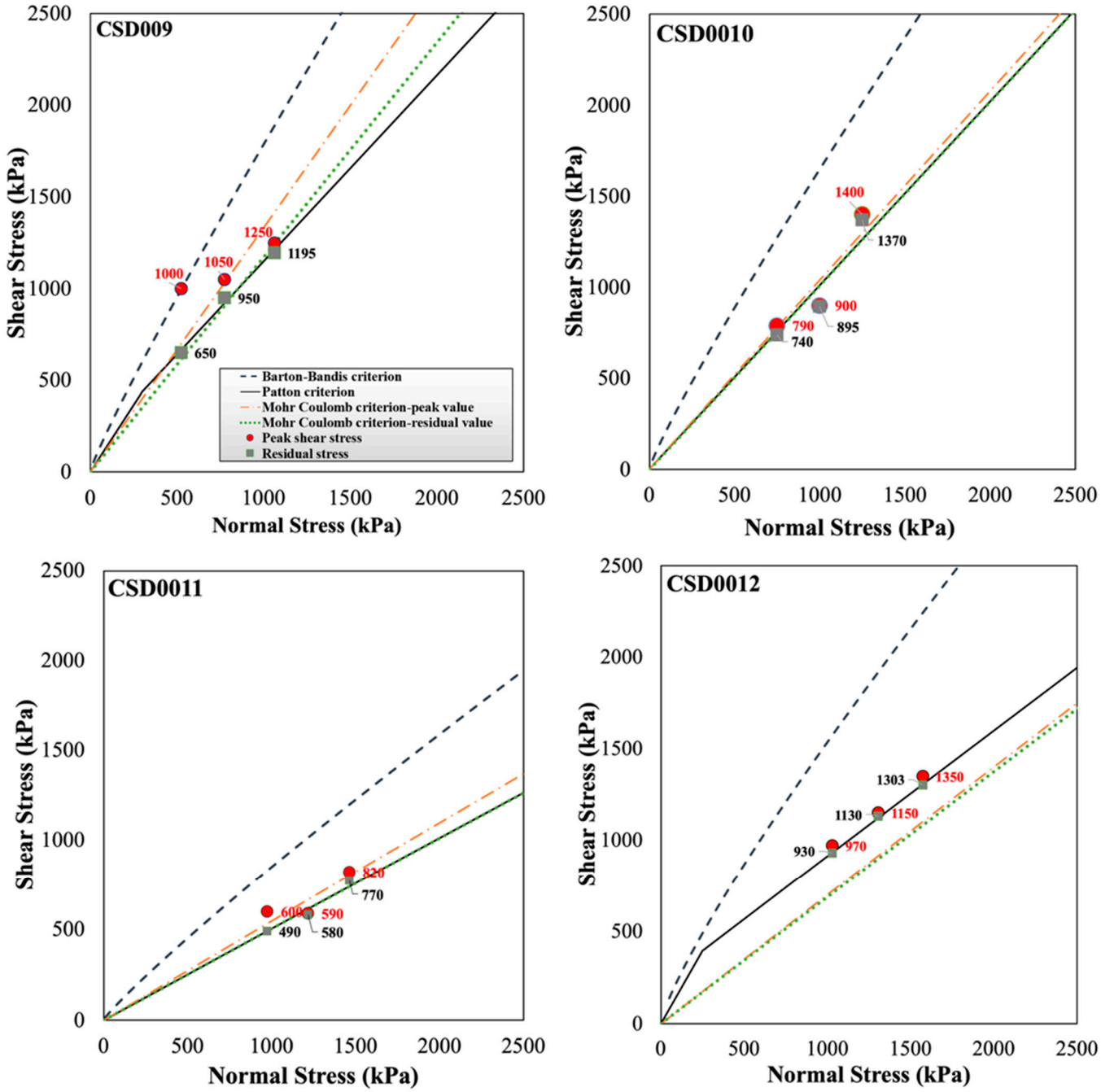

Figure 11. Comparison of the shear strength results for samples CSD009, CSD 0010, CSD0011, and CSD0012.

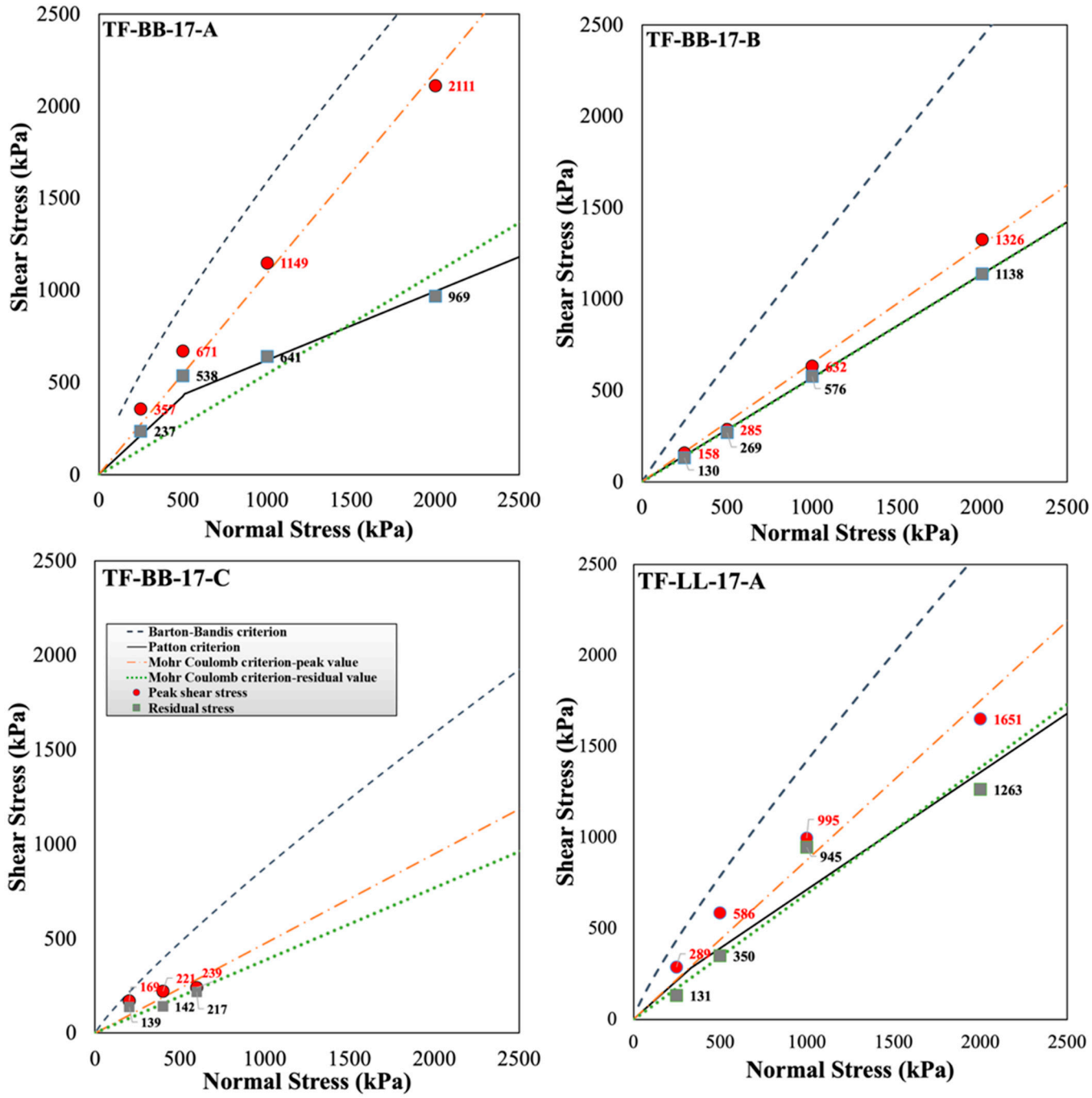

Figure 12. Comparison of the shear strength results for samples TF-BB-17-A, TF-BB-17-B, TF-BB-17-C, and TF-LL-17-A.

It is important to clarify that the Mohr–Coulomb and Patton criteria were fitted to the experimental data from each specimen, while the Barton–Bandis criterion was applied using independently estimated JRC and JCS values. This asymmetry reflects common engineering practice, where Mohr–Coulomb and Patton parameters are routinely derived from project specific shear tests, whereas Barton–Bandis is often applied using field estimated JRC and JCS without test specific calibration. For the Mohr–Coulomb criterion, the friction angle was estimated from the basic friction angle measured on saw-cut surfaces (φb) and cohesion was assumed to be zero. For the Patton criterion, the asperity inclination was estimated from visual profile descriptions rather than from the back calculation of dilation. For the Barton–Bandis criterion, the JRC values were estimated from visual comparison with

standard profiles, as in the original analysis. In this predictive mode, the Barton–Bandis criterion continued to show the largest errors, but the margin of overestimation was less pronounced than in the original analysis, and all three criteria exhibited larger errors than in the calibrated mode, as expected. These results confirm that the poor performance of the Barton–Bandis criterion in the primary benchmark is largely attributable to the difficulty of estimating JRC from visual core logging, rather than to an inherent flaw in the Barton–Bandis formulation.

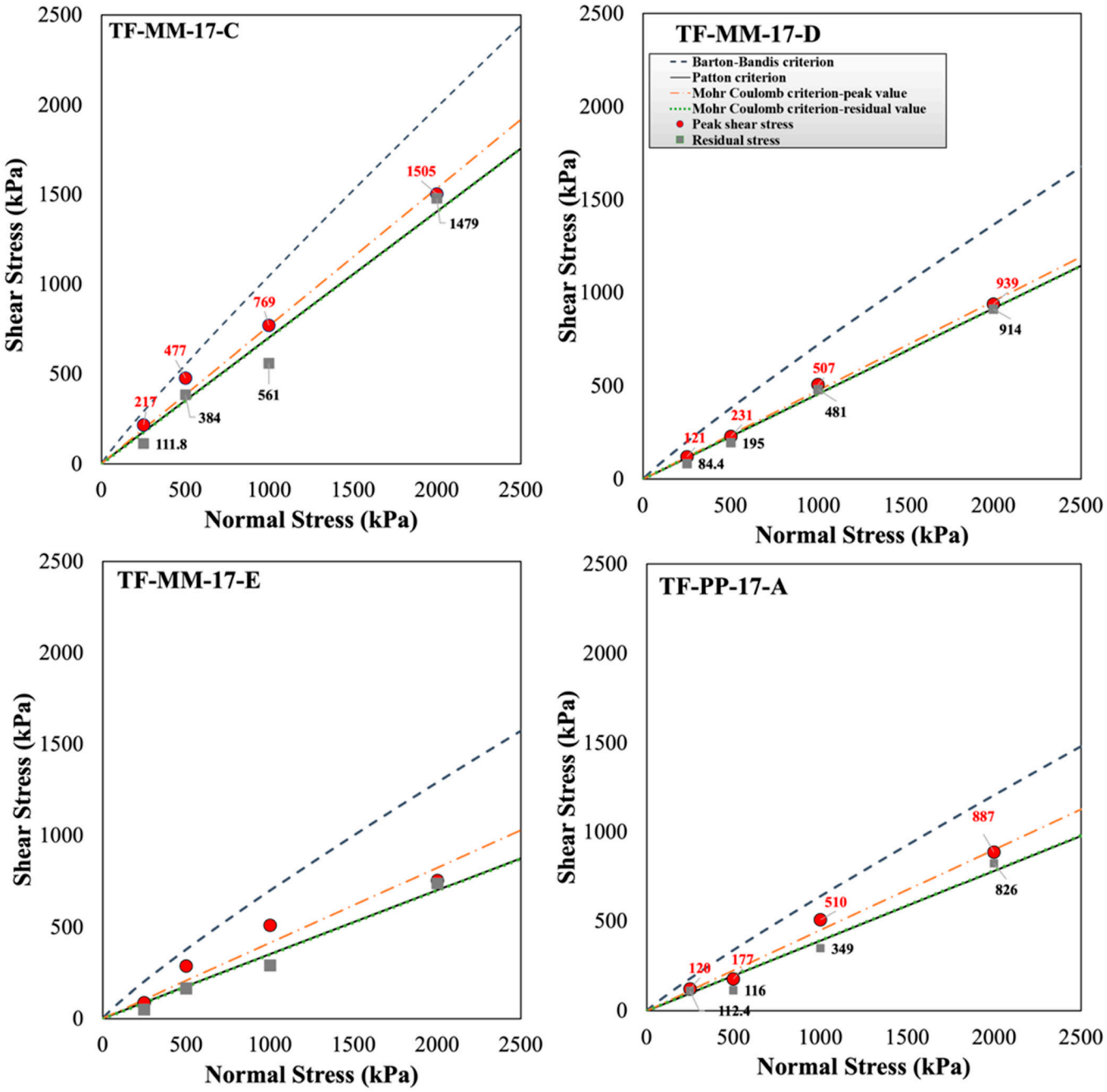

Figure 13. Comparison of the shear strength results for samples TF-MM-17-C, TF-MM-17-D, TF-MM-17-E, and TF-PP-17-A.

An intact-rock UCS of 175 MPa was used as the reference JCS value in the initial Barton–Bandis calculations. This value should not be interpreted as a specimen-specific measurement of joint wall compressive strength; the influence of lower JCS values was examined separately in the JCS sensitivity analysis. It should be noted that the three criteria

do not rely on identical parameter-estimation procedures in this case study. The Mohr–Coulomb and Patton parameters were derived from the available project-specific shear-test data, whereas the Barton–Bandis criterion was applied using independently estimated JRC and JCS inputs. The comparison should therefore be interpreted as a case-specific engineering assessment rather than as a formal ranking of the intrinsic predictive capability of the three criteria.

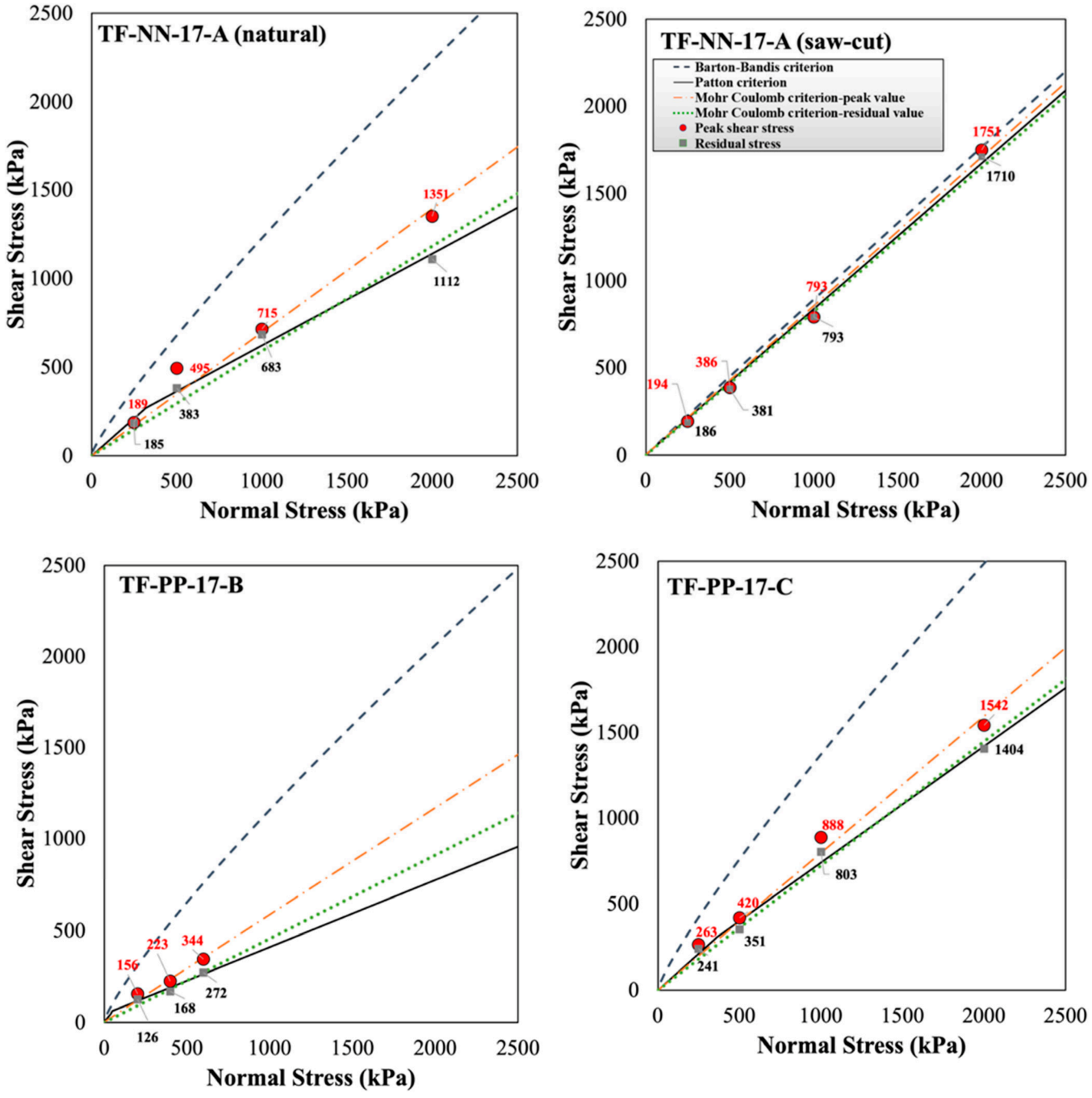

Figure 14. Comparison of the shear strength results for samples TF-NN-17-A (natural and saw-cut), TF-PP-17-B, TF-PP-17-C illustrating the performance of the Barton–Bandis, Patton, and Mohr–Coulomb criteria (peak and residual stress).

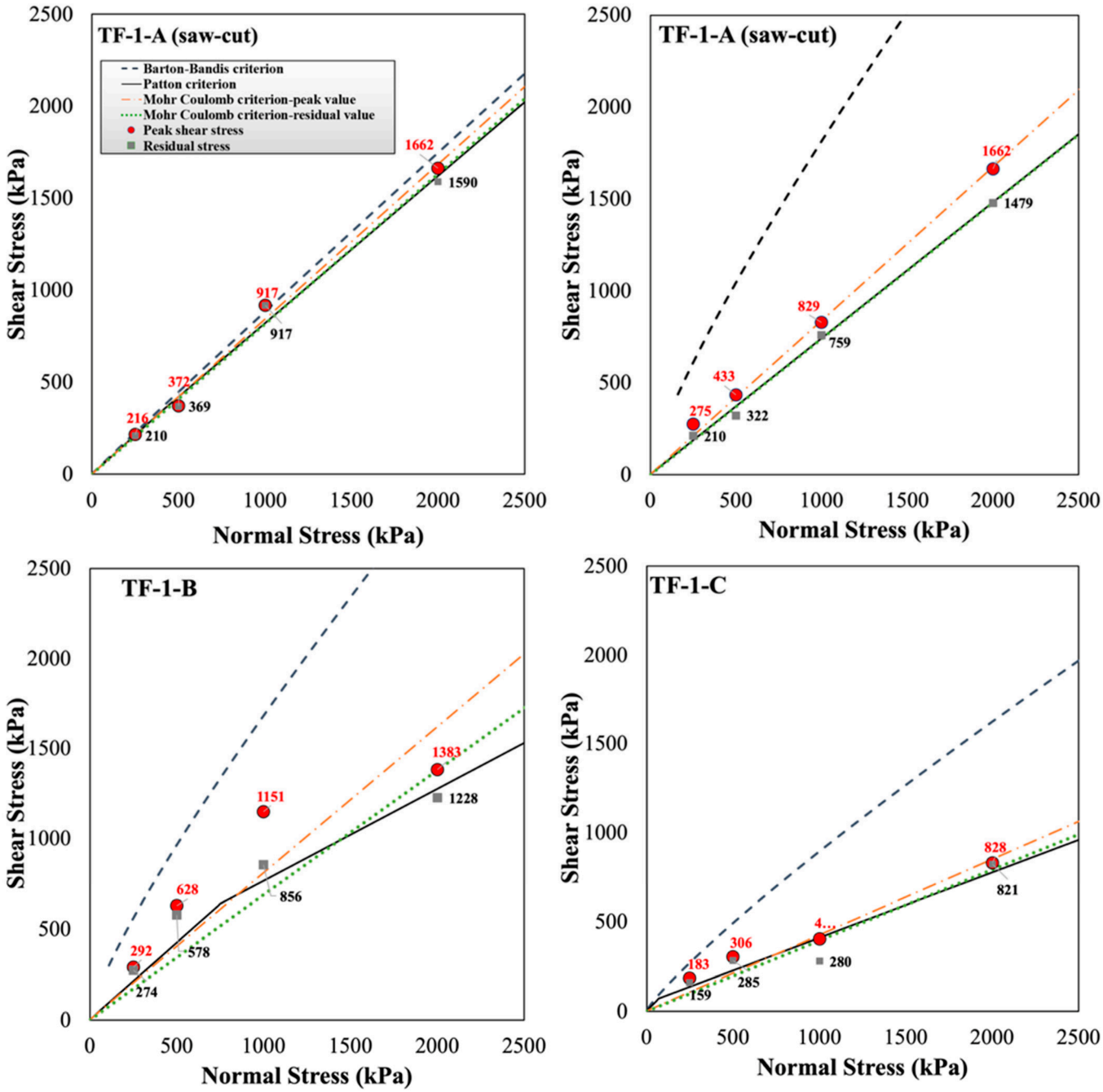

Figure 15. Comparison of the shear strength results for samples TF-1-A (natural and saw-cut), TF-1-B, TF-1-C illustrating the performance of the Barton–Bandis, Patton, and Mohr–Coulomb criteria (peak and residual stress).

5.4. Evaluation of the Effect of JCS on Shear Strength

Determination of the JCS is particularly challenging in practice, primarily because core samples from joint-filling materials are difficult to obtain. A Schmidt hammer test performed directly on the joint surface is often used as a practical means to estimate JCS; however, its reliability is relatively low, even when it is applied to estimate the uniaxial compressive strength (UCS) of intact rock. In engineering practice, JCS is frequently approximated by the UCS of the intact rock [129]. In some cases, a conservative estimate expressed as a percentage of the intact UCS is proposed as a lower bound for JCS. For instance, a value of JCS = 25%·UCS was suggested by Barton [130,131].

In the case of the Romaine-IV hydroelectric plant, where rock mass conditions display a range of weathering states and JRC values, the effect of JCS was accounted for in three selected roughness cases (JRC = 1, 9, and 11). For each JRC value, three JCS levels (i.e., 25%, 50%, and 100% of the UCS) were considered.

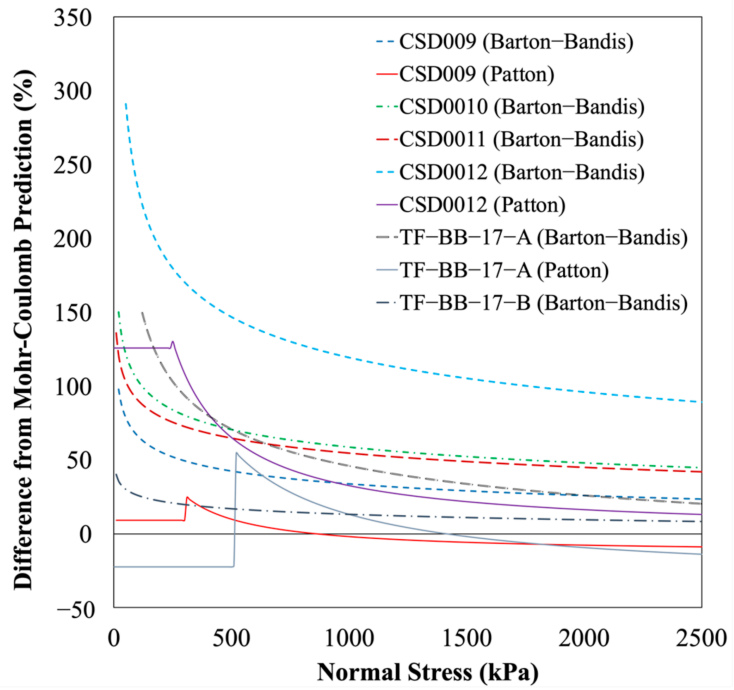

Figure 16. The difference between rupture criteria for samples CSD009, CSD 0010, CSD0011, CSD0012, TFBB-17-A, and TF-BB-17-B.

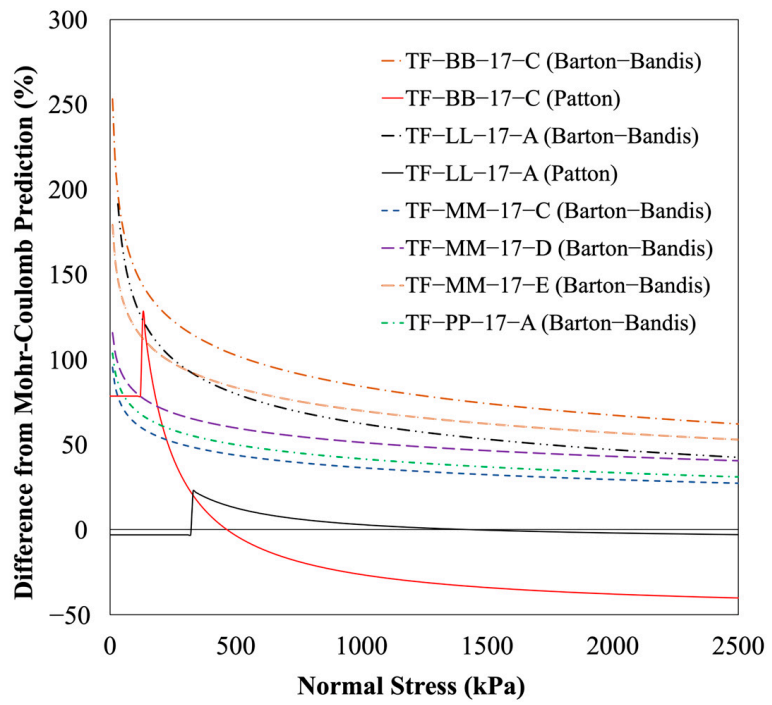

Figure 17. The difference between rupture criteria for samples TF-BB-17-C, TF-LL-17-A, TF-MM-17-C, TF-MM-17-D, TF-MM-17-E, and TF-PP-17-A.

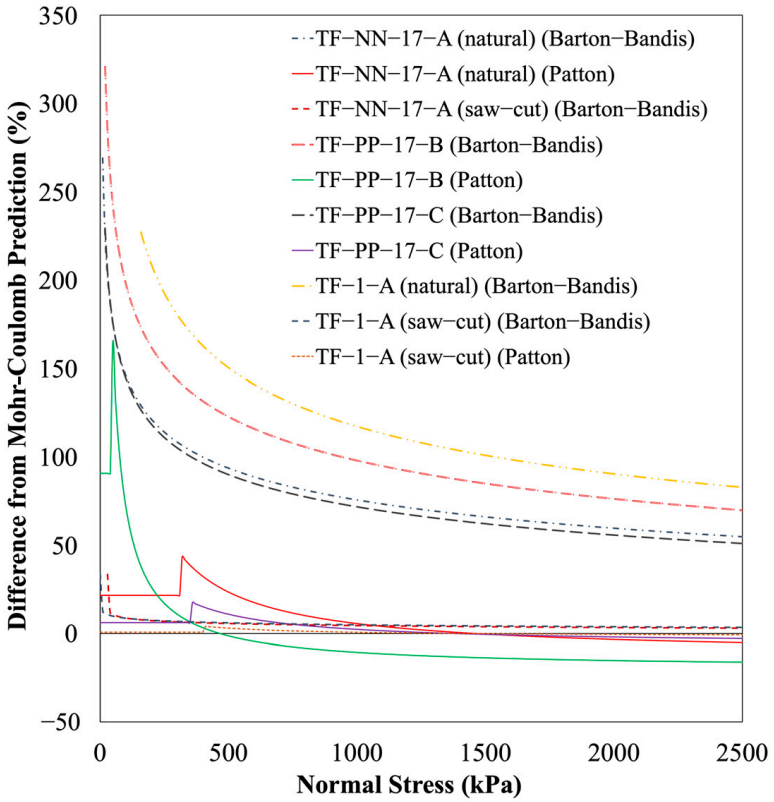

Figure 18. The difference between failure criteria for samples TF-NN-17-A (natural and saw-cut), TF-PP-17-B, TF-PP-17-C, and TF-1-A (saw-cut and natural).

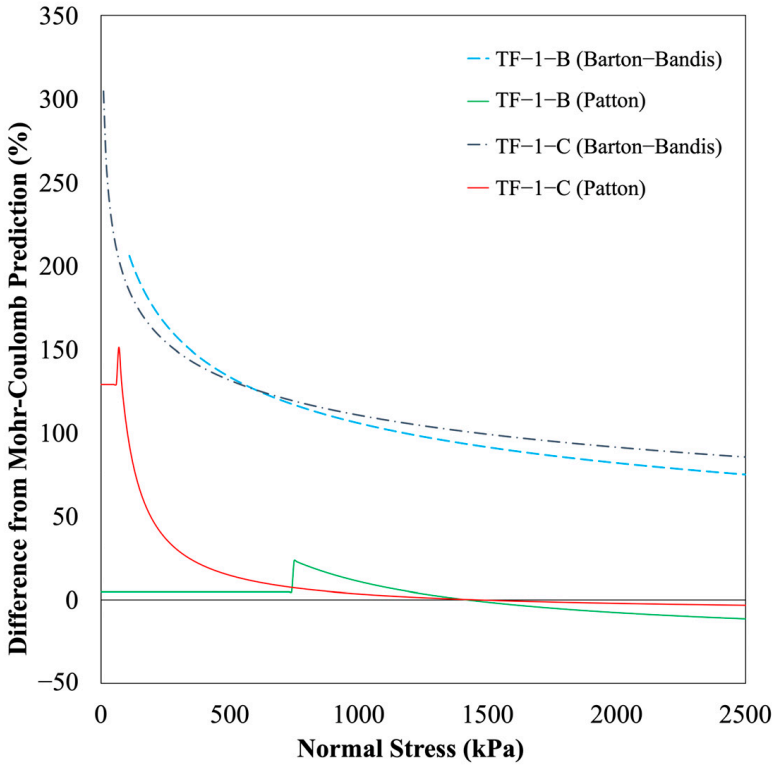

Figure 19. The difference between rupture criteria for samples TF-1-B and TF-1-C.

The sensitivity analysis shows that the assumed JCS has a systematic influence on the Barton–Bandis envelope, with increasing JCS shifting the predicted shear strength upward. The effect is particularly noticeable at lower normal stresses, emphasizing the importance of selecting JCS values that reflect the actual condition of the joint wall. Figure 20a presents the results for sample TF-LL-17-A (NAT) with JRC = 9, where Barton–Bandis envelopes for *JCS* = 25%, 50%, and 100% × *UCS* were compared against Mohr–Coulomb (peak/residual) and Patton criteria on axes of shear strength τ (kPa) versus normal stress σ_n (kPa). Increasing JCS shifts the Barton–Bandis envelope upward. Even at JCS = 25%, the *UCS* predictions exceeded those of Mohr–Coulomb and Patton across the plotted range. Figure 21a depicts the percentage difference in predicted shear strength relative to the Mohr–Coulomb reference (dotted line) for the same sample and JRC, evaluated at JCS = 25%, 50%, and 100% × *UCS*. Positive values indicate predictions over Mohr–Coulomb, with the largest magnitude at low σ_n diminishing as σ_n and/or assumed JCS increased. Figure 20b shows the same analysis as Figure 20a for TF-PP-17-B (natural) with JRC = 11, and Figure 21b provides the corresponding percentage-difference plot as in Figure 21a for that sample and JRC. Figure 20c repeats the envelope comparison for TF-NN-17-A (saw-cut) with JRC = 11, and Figure 21c presents the associated percentage-difference results analogous to Figure 21a,b.

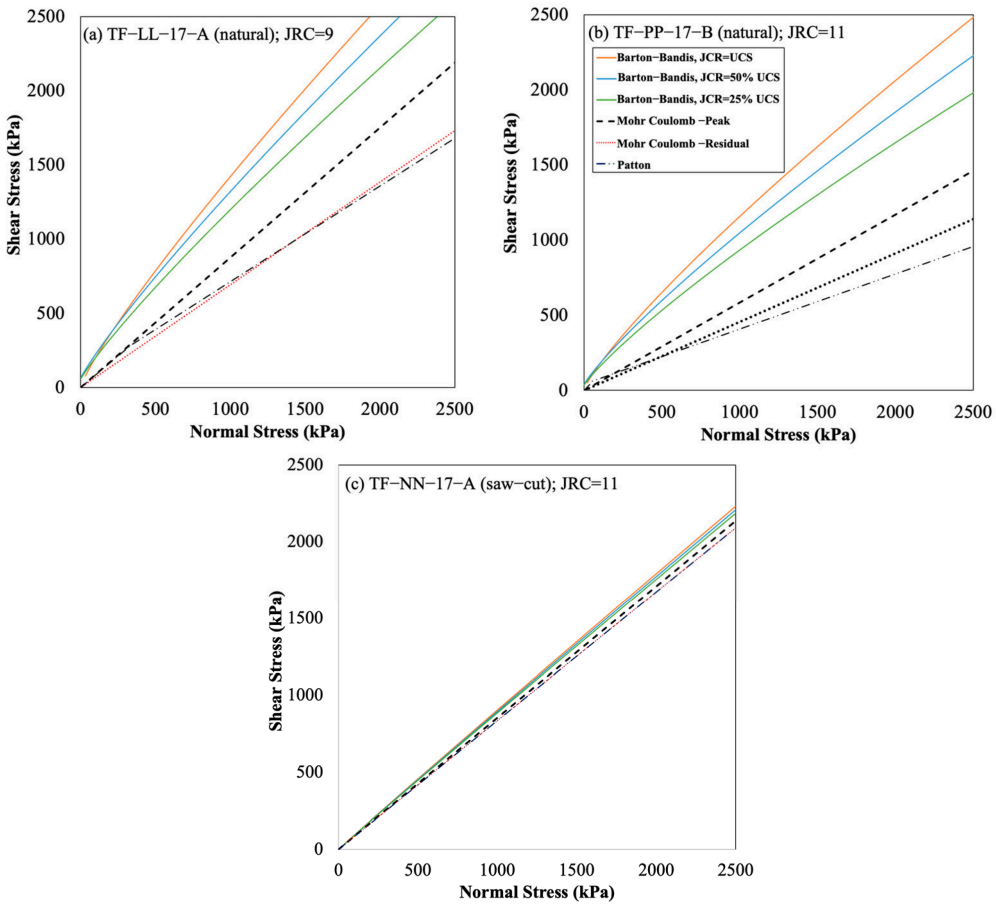

Figure 20. Effect of assumed joint wall compressive strength (JCS = 25%, 50%, and 100% of UCS) on the predicted peak shear stress versus normal stress for (**a**) TF-LL-17-A (natural), JRC = 9; (**b**) TF-PP-17-B (natural), JRC = 11; and (**c**) TF-NN-17-A (saw-cut), JRC = 11.

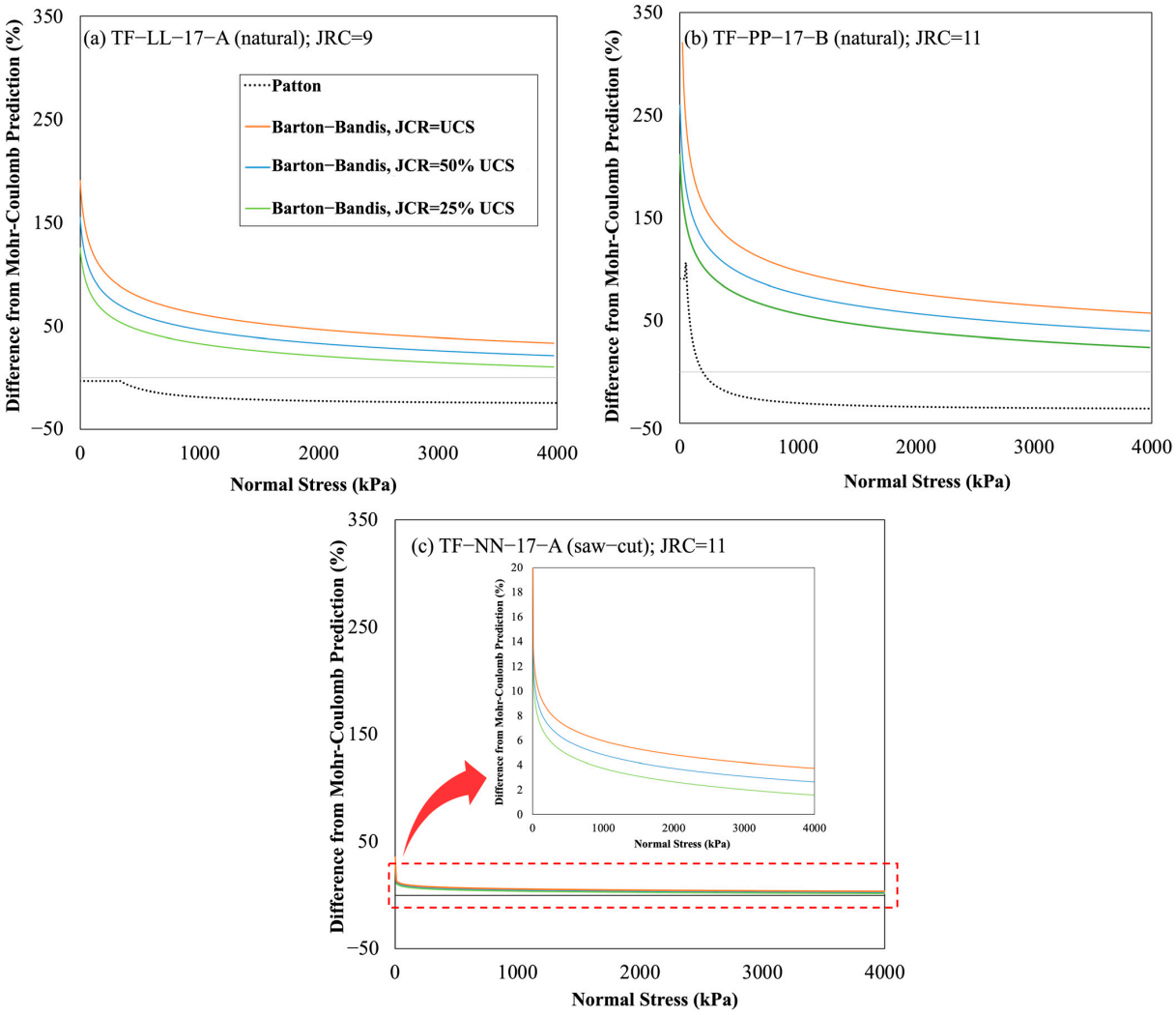

Figure 21. Percentage difference from the Mohr–Coulomb prediction, versus normal stress for (**a**) TF-LL-17-A (natural); (**b**) TF-PP-17-B (natural), JRC = 11; and (**c**) TF-NN-17-A (saw-cut), JRC = 11.

6. Discussion

This review shows that disagreements among shear-strength criteria are rarely model versus model. They are typically assumption versus assumption. Across most formulations, peak shear resistance can be interpreted as a frictional baseline governed by mineralogy and true contact, augmented by a morphology-controlled contribution from dilation and interlocking. This morphology term is stress-dependent (i.e., suppressed by confinement) and path-dependent (i.e., reduced by wear and asperity damage). Consequently, different criteria mostly diverge in three places. First, they offer how they encode morphology (profile-based indices, 3D asperity statistics, or multi-scale descriptors). Second, they differ in whether and how they represent progressive degradation, and third, they differ in which boundary condition they implicitly assume such as CNL, CNS, or stiffness-controlled intermediate paths. Framed this way, the practical question is not only which equation is more physical, but which set of assumptions matches the test or field scenario and can be supported by measurable inputs at the project scale.

There is a wealth of experimental data scattered in the literature. Efforts to compile large databases help in evaluating models. One challenge is standardizing roughness characterization. For example, if everyone reported θ^*_{max} and basic friction from scans, it would be easier to compare studies than using subjective JRC. The field is moving towards using

3D scanners and maybe even smartphone apps to measure joint roughness quickly [132]. As that becomes common, criteria like Grasselli's could see more routine use.

Insights from the Romaine-IV benchmark reinforce this interpretation. The comparative performance trends indicate that a simpler envelope may outperform a more "mechanistic" criterion when the latter depends on parameters that are difficult to estimate consistently across samples (e.g., JRC/JCS assignment, matching state, and damage evolution). This does not imply that complexity is unnecessary. Rather, it highlights that model fidelity is only useful when its inputs are observable and estimated under reproducible protocols. A defensible workflow therefore has two steps. The first step is to select a criterion whose inputs can be directly measured (or tightly bounded) for the relevant joint population, and the next one is to explicitly represent uncertainty in roughness, wall strength, matching, infill, hydraulic state, and boundary stiffness through ranges or probabilistic sampling instead of single best-guess values. This approach often reduces criterion selection to an evidence-based choice about data availability and uncertainty tolerance.

A key barrier to state-of-the-art practice is the lack of standardization in how joint morphology and test conditions are measured and reported. The field is transitioning from subjective profile-based indices toward 3D point-cloud acquisition (portable scanners, photogrammetry, LiDAR) and automated roughness descriptors. However, comparability remains limited unless acquisition resolution, filtering, window size, reference shear direction, and registration/matching procedures are disclosed. Without these details, the same roughness metric can represent different physical surfaces, and calibration becomes non-transferable. Table 4 proposes a minimal measurement/metadata package that links what is measured to what each model family requires, so that studies can be compared meaningfully and benchmarks can be reused. This package also supports reproducibility for the case-study component and provides a clear pathway for future shared databases.

Table 4. Minimum measurement and metadata package to connect joint characterization to model selection and reproducibility.

Element to Report	How It Is Measured	Key Reporting Details	Feeds Which Model Families	Why It Matters
Boundary condition	Shear test setup	CNL vs. CNS (stiffness), normal stress path, shear rate	All	Controls dilation mobilization and peak envelope curvature
Surface acquisition	3D scan/photogrammetry/LiDAR/profilometer	Resolution, filtering, window size, shear direction reference	3D/multi-scale & ML; also informs JRC	Roughness indices are not comparable without acquisition context
Matching/contact state	Registration of opposing surfaces; contact mapping	Initial offset/mismatch, contact ratio vs. σn, wear state	Barton-type, 3D morphology, damage models	Strong driver of scatter and bias across tests
Wall strength	UCS/Schmidt/point load; petrography	Test method, anisotropy, alteration, moisture	Barton–Bandis (JCS), damage/wear models	Sets asperity crushing threshold and degradation rate
Infill & aperture	Visual logging + lab tests on infill	Thickness, continuity, mineralogy, shear strength, saturation	Infilled-joint criteria; hydro-mechanical models	Controls transition from interlocking to gouge-dominated shear
Hydraulic state	Pore pressure/ saturation conditions	Effective σ_n, drainage, suction	Hydro-mechanical extensions	Peak strength can be effective-stress controlled
Cyclic/dynamic loading	Loading protocol	Amplitude, frequency, number of cycles, dwell times	Dynamic/cyclic criteria; constitutive laws	Ratcheting and wear can dominate long-term behavior

Recent advances point to three converging research directions. The first direction is multi-scale morphology. Modern 3D scans allow roughness to be represented as a spectrum from waviness to unevenness to micro-asperities, which aligns naturally with scale-dependent mobilization of dilation and asperity damage. The second direction is hybrid modelling. Physics-informed or constrained machine-learning surrogates can emulate

high-fidelity numerical shear simulations while enforcing physically admissible behavior (e.g., monotonicity with normal stress, bounded frictional response), enabling rapid uncertainty propagation for design. The third direction is coupled and time-dependent processes. Emerging formulations increasingly incorporate hydromechanical coupling including effective stress, seepage-driven changes, infill softening, as well as cyclic and dynamic loading effects such as amplitude and frequency effects, ratcheting, and progressive wear. These processes govern long-term performance but are poorly captured by single-stage peak envelopes.

These trends imply a roadmap that is both technical and practical (Table 5). Progress is likely to shift from proposing additional standalone criteria toward establishing shared benchmarks, standardized measurement pipelines, and reproducible calibration/validation protocols across laboratories and sites. This shift is essential for distinguishing genuine model improvement from dataset-specific tuning. In parallel, field-scale validation should become routine: advanced criteria gain credibility only when their added inputs and complexity improve decisions under realistic boundary stiffness and hydraulic conditions (and when the decision impact of the added complexity is quantified).

Table 5. Forward-looking research and practice roadmap for joint shear-strength prediction.

Theme	Near-Term (1–3 Years)	Mid-Term (3–7 Years)	Deliverables for Adoption	Main Risks/Barriers
Standardized morphology	Reporting template; inter-lab round-robin for roughness metrics	Reference standards linking 2D↔3D indices + uncertainty envelopes	Shared protocols + open roughness tools	Device heterogeneity; proprietary pipelines
Open datasets & benchmarks	FAIR datasets with raw scans + shear curves + metadata	Multi-site benchmarks spanning lithology/infill/weathering/CNS-CNL	Reproducible calibration scripts + leaderboards	Data ownership; project confidentiality
Hybrid physics–ML models	Constrained ML surrogates; uncertainty-aware prediction	Generalizable models + transfer learning with small site datasets	Interpretable tools with physical constraints	Overfitting; missing edge cases
Coupled processes (HM/THM)	Effective-stress + stiffness pathways added to peak prediction	Unified peak + post-peak with pore pressure, temperature, damage	Design guidance for water/temperature/cyclic cases	Parameter identifiability; costly testing
Scale bridging	Upscaling rules from lab to field populations	DFN-scale calibration with field mapping + monitoring	Methods translating scan metrics to design parameters	Non-representative sampling; anisotropy
Field-scale validation	Instrumented case histories + uncertainty back-analysis	Routine validation + monitoring-based updating	Demonstrated transferability and decision impact	Sparse monitoring; confounding processes

From an engineering perspective, the findings motivate a tiered application strategy. For preliminary design, use a robust baseline envelope calibrated to project-specific shear tests, and treat morphology-related corrections as uncertainty bands rather than deterministic increments. For detailed design and risk-critical scenarios (e.g., stiff confinement, seismic/cyclic loading, repeated drawdown, or persistent seepage), adopt criteria or constitutive laws that explicitly encode boundary stiffness, cyclic degradation, and hydraulic effects. However, this should only be carried out when the required inputs are measured at commensurate scale and resolution. In all cases, transparent reporting of input estimation methods, uncertainty bounds, and validation metrics is as important as the mathematical form of the criterion itself.

It is also important to acknowledge that the Romaine-IV benchmark presented in this study is based on data from a single project, a single lithological unit, and a single testing protocol. The quantitative findings and performance rankings reported in this benchmark should therefore be interpreted within the geological conditions, joint characteristics, testing procedures, and normal-stress range represented by this dataset. The comparison is intended as a case-specific engineering assessment and should not be interpreted as demonstrating the

general superiority of one shear-strength criterion over another. Broader generalization will require multi-site datasets and field-scale validation under a wider range of rock types, joint conditions, and boundary stiffness regimes.

7. Conclusions

This paper synthesizes the evolution of rock-joint shear-strength representation from frictional envelopes to morphology-aware and process-coupled formulations, and clarifies why predictions diverge. Criteria embed different assumptions about morphology mobilization, degradation, and boundary stiffness. The classification into seven conceptual families demonstrates that no single criterion is universally superior. Linear frictional models such as Mohr–Coulomb remain attractive for their simplicity and minimal data requirements, while 3D morphology-based and data-driven criteria offer higher fidelity at the cost of greater input complexity and calibration effort.

Using the Romaine-IV dataset as an applied case study, the comparison illustrates that the agreement between measured and predicted shear-strength envelopes is strongly influenced by the way criterion parameters are determined. The results should therefore be interpreted within the geological conditions, joint characteristics, testing procedures, parameter-estimation methods, and normal-stress range represented by this dataset, rather than as evidence of the general superiority of one criterion over another.

For practice, the selection of a shear-strength criterion should be guided by data availability and uncertainty tolerance. For preliminary design, a robust baseline envelope such as Mohr–Coulomb calibrated to project-specific shear tests is sufficient. For risk-critical scenarios involving stiff confinement, cyclic loading, or persistent seepage, criteria that explicitly encode boundary stiffness, degradation, and hydraulic effects should be adopted, but only when the required inputs are measured at commensurate scale and resolution.

To strengthen the forward-looking contribution, the review identifies a roadmap in which progress depends less on proposing additional peak envelopes and more on several key areas. Standardized 3D joint characterization with clearly reported acquisition and processing conventions is needed. Open and reproducible benchmarks that connect raw morphology to shear response should be established. Hybrid physics–ML surrogates suitable for design-level uncertainty propagation require further development. Extensions that explicitly incorporate hydromechanical coupling, cyclic and dynamic loading, and progressive wear are also necessary. Finally, it is emphasized that the review is a narrative critical synthesis rather than a formal meta-analysis. Broader generalization will require multi-site datasets and field-scale validation under a wider range of rock types, joint conditions, and boundary stiffness regimes.

Supplementary Materials: The following supporting information can be downloaded at: https://www.mdpi.com/article/10.3390/geotechnics6040113/s1, Table S1: Specimen-specific parameters used in the Romaine-IV criterion comparison; Supplementary File S1: Calculation workbook containing the experimental stress data, specimen-specific calculations, criterion comparison plots, and JCS sensitivity analyses for the Romaine-IV rock-joint specimens.

Author Contributions: Conceptualization, A.S.; methodology, M.M., A.S. and J.-F.N.; software, M.S. (Mahdiyeh Seifaddini) and M.M.; validation, M.M. and M.S. (Mahdiyeh Seifaddini); formal analysis, M.M., M.S. (Mahdiyeh Seifaddini), and A.S.; investigation, M.S. (Mahdiyeh Seifaddini) and M.M.; resources, A.S., M.S. (Mahdiyeh Seifaddini) and J.-F.N.; data curation, M.M. and M.S. (Mahdiyeh Seifaddini); writing—original draft preparation, M.M.; writing—review and editing, M.M., A.S., J.-F.N., M.S. (Mahdi Salimi) and M.P.; visualization, M.M., M.S. (Mahdiyeh Seifaddini) and M.S. (Mahdi Salimi); supervision, A.S. and J.-F.N.; project administration, A.S.; funding acquisition, A.S. and J.-F.N. All authors have read and agreed to the published version of the manuscript.

Funding: This work was financially supported by the Natural Sciences and Engineering Research Council of Canada (NSERC) (Grant Nos. RDCPJ 537350–18 and RGPIN-2019-06693), Mitacs Inc. (Grant No. IT22640), Hydro-Québec and Uniper.

Institutional Review Board Statement: Not applicable.

Informed Consent Statement: Not applicable.

Data Availability Statement: The experimental data and supporting calculation material used in the Romaine-IV case study are provided in the Supplementary Materials. Additional supporting information is available from the corresponding author upon reasonable request.

Conflicts of Interest: Author Jean-François Noël was employed by Hydro-Québec. The remaining authors declare that the research was conducted in the absence of any commercial or financial relationships that could be construed as a potential conflict of interest.

Nomenclature

Symbol	Definition	Symbol	Definition
τ	Shear stress (MPa)	σ_c	Uniaxial compressive strength (MPa)
σ_n	Normal stress (MPa)	P_N	Normal pressure factor
σ'_n	Effective normal stress	u	Pore pressure
φ_m	Mobilized friction angle	ACF	Auto Correlation Function
φ_b	Basic friction angle (degrees)	PSD	Power Spectral Density
φ_r	Residual friction angle (degrees)	*SRP*	Shear Resistance Parameter
i_0	Initial dilation angle (degrees)	B_1, B_2	Empirical fitting constants
c	Cohesion (MPa)	A_0	Roughness amplitude constant
a_s	Asperity sliding factor	C	Roughness or scale factor
ε	Shear displacement rate	θ^*_{max}	Maximum apparent dip angle (degrees)
φ_f	Final friction angle (degrees)	A_2	Empirical constant for surface roughness
JRC	Joint Roughness Coefficient	Z_2r	Root-mean-square of asperity angles
JCS	Joint Wall Compressive Strength (MPa)	C_m	Maximum contact coefficient
JMC	Joint Matching Coefficient	σ_t	Tensile strength (MPa)
CLA	Centerline Average of asperity heights	*RMS*	Root-mean-square of asperity height
L	Joint length in shear direction (m)	l	Measurement resolution (mm)
JRC_d	Dynamic JRC coefficient	f	Dynamic normal load frequency (Hz)
F_d	Dynamic normal load amplitude (MPa)	*OCR*	Over Consolidation Ratio
t	Infill thickness (mm)	a	Asperity height (mm)
λ	Wavelength of joint roughness	D	Fractal Dimension
R_P	Roughness Profile Index	*RS*	Surface Roughness Coefficient
r	Actual joint roughness at the sample scale	R	Reference roughness profile
k_1, k_2	Constants in empirical equations	e^K	Exponential coefficient in shear models

Appendix A

Table A1 provides a consolidated comparison of the shear-strength criteria reviewed above, organized by criterion family. For each model, the table reports the corresponding equation number in this manuscript, the derivation basis (e.g., laboratory direct shear calibration, empirical regression, or mechanics-based formulation), the newly introduced parameter(s), the minimum set of inputs required for calculation, and the typical laboratory/field equipment needed to obtain those inputs (e.g., direct shear system under CNL/CNS, roughness profiling/3D scanning, UCS/Brazilian tensile tests, Schmidt hammer, and contact/mismatch mapping). This summary is intended to help readers rapidly identify the most appropriate criterion for a given application and to make the data and testing requirements transparent before model selection and implementation.

Table A1. Summary of the rock-joint shear-strength criteria reviewed in Section 4, grouped by criterion family, with equation mapping and input/testing requirements.

Family	Criterion	Eq. No(s)	Test Basis	New Parameter(s) Introduced	Inputs Needed to Compute	Required Equipment/Measurements	Merits	Limitations
Linear friction	Mohr–Coulomb	(13)	Empirical friction envelope; used in design	φ (and c if included)	σ_n; φ ($\pm c$)	Direct shear on smooth/saw-cut or tilt test (φ); normal stress σ_n	Very simple; common baseline	No explicit roughness/dilation/scale
	Newland & Alley	(14)	Direct shear interpretation (displacement deviation effect)	δ (avg. deviation of shear displacement)	σ_n; φ; δ	Direct shear test with displacement tracking; smooth-joint φ	Adds kinematic effect to linear law	Still limited for natural rough joints; δ measurement-sensitive
2D asperity & dilation	Patton	(15)	Laboratory shear on sawtooth joints (low vs. high σ_n regimes)	i (asperity inclination)	σ_n; φ_b; i; σ_T	Direct shear box (CNL/CNS); sawtooth geometry or profile to estimate i; smooth-joint φ_b	Mechanistically intuitive bilinear concept	Abrupt transition; i hard to define for natural joints; no progressive degradation
	Schneider	(16) and (17)	Extension with normal-stress-dependent roughness degradation	k (degradation factor)	σ_n; φ_b; roughness index; $k(\sigma_n)$	Direct shear + roughness profiling; calibration to estimate k	Captures stress-dependent roughness loss	More parameters; k estimation uncertain
	Ladanyi–Archambault	(18) and (19)	Analytical partition of sliding vs. shearing; calibrated on tests	a_s (sheared-area ratio); dilation function	σ_n; φ_b; asperity geometry; $a_s(\sigma_n)$	Direct shear (often CNS preferred for dilation); surface geometry characterization	Explicitly represents dilation + asperity shearing	Parameterization complex; assumptions on asperity behavior
	Saeb	(20)–(23)	Mechanistic/empirical framework with scale and stress effects	transitional stress; sheared-area ratio	σ_n; φ_b; surface angle/roughness; σ_T	Direct shear + surface profiling; limited calibration for σ_T	Bridges bilinear concepts and progressive transition	Requires σT; still relies on simplified roughness scale

Table A1. *Cont.*

Family	Criterion	Eq. No(s)	Test Basis	New Parameter(s) Introduced	Inputs Needed to Compute	Required Equipment/Measurements	Merits	Limitations
JRC–JCS empirical	Barton (JRC–JCS)	(24)	Regression from many direct shear tests on natural joints	JRC; JCS; φ_r	σ_n; JRC; JCS; φ_r	JRC from profile/3D scan; JCS from UCS/Schmidt/point-load; φ_r from smooth shear/tilt	Widely used; includes roughness + strength scaling	No explicit matching/contact area; empirical limits
	Barton & Choubey (with residual friction)	(25) (+ residual φ_r relation)	Refinement of JRC–JCS database and parameter relations	updated φ_r relation	σ_n; JRC; JCS; φ_r	Same as Barton; plus lab/field friction for φ_r	Improved parameter interpretation; practical	Still empirical; input uncertainty (JRC/JCS)
	Lee et al. (roughness angle modification of Barton)		Barton-type with alternative roughness angle definition	roughness angle parameter	σ_n; roughness angle; JCS/strength terms; φ_r	Roughness profiling or 3D scan to derive roughness angle; JCS tests	Alternative parameterization to reduce JRC subjectivity	Still empirical; parameter definition depends on measurement method
	Zhao (JRC–JMC for mismatch)	(26)	Modification to account for joint mismatch	JMC (matching coefficient)	σ_n; JRC; JMC; JCS; φ_r	3D scan/matching analysis to estimate JMC; plus JRC/JCS tests	Better for mismatched joint halves	JMC can be subjective; adds complexity
	He et al. displacement-dependent Barton	(67)	Large CNL test database; JRC evolves with shear displacement	$JRC(u)$ degradation function	σ_n; *JCS*; initial *JRC*; displacement u; φ_r	Direct shear (CNL) with displacement control; roughness measurement; JCS tests	Captures peak-to-residual evolution under CNL	Empirical staging; needs calibration data

Table A1. *Cont.*

Family	Criterion	Eq. No(s)	Test Basis	New Parameter(s) Introduced	Inputs Needed to Compute	Required Equipment/Measurements	Merits	Limitations
Constitutive/state-variable	Plesha (displacement-based degradation)	(27)	Constitutive formulation for progressive dilation degradation	state variable(s) linked to shear displacement	σ_n; φ; dilation/roughness state variables; displacement	Shear tests with displacement history; calibration of evolution law	Suitable for numerical implementation; continuous degradation	Calibration-intensive; not a closed-form peak-only criterion
	Cundall & Hart (CYJ model)	(28) and (29)	Continuously yielding joint (mob. friction angle decays with plastic shear)	φ_m; R (characteristic displacement)	σ_n; φ_i; φ_r; R; plastic shear displacement	Shear tests to fit R, φ_j, φ_r; displacement measurement	Captures wear-driven strength loss	Needs full shear path; parameter fitting
	Gui et al. 3D morphology-based constitutive law	(62)	Couples morphology descriptors with evolving contact/damage state	damage/contact evolution terms	σ_n; morphology descriptors; damage state; displacement	3D scan + shear tests with monitoring of damage/contact (or calibration)	Represents multi-stage shear response; numerical-ready	High data demand; complex calibration
3D morphology-based (static peak)	Grasselli & Egger	(30)	Facet-based 3D morphology; apparent dip statistics	θ^*_{max}; A_0 (potential contact area)	σ_n; φ_b; θ^*_{max}; A_0	High-res 3D surface scan + facet analysis; smooth-joint φ_b	Directional 3D roughness + dilation link	3D data + processing required; calibration bias risk
	Cottrell et al.	(31)	3D morphology with tensile-strength-controlled asperity failure	tensile strength term; morphology factors	σ_n; φ_b; 3D morphology metrics; σ_t	3D scanning; Brazilian tensile test (σ_t); shear/tilt for φ_b	Improves prediction when tensile failure governs	Sensitive to resolution; parameter-heavy
	Tatone & Grasselli (resolution correction)	(32)	Shear tests + varying scan point spacing (0.044–4 mm)	resolution-dependent exponent	scan spacing; specimen length; Grasselli parameters	3D scan at multiple resolutions; direct shear tests for calibration	Accounts for sampling-resolution effect	Still inherits base-model issues; calibration dataset limited
	Tang et al. (MC-form with 3D roughness + σt)	(33)	Regression on compiled shear-test database (tensile & replica joints)	combined 3D descriptor; measurement spacing l	σ_n; φ_b; 3D descriptor; σ_t; l	3D scan + compute descriptor; Brazilian tensile; know sampling l	MC-form convenient for design	Reported overestimation for natural joints; no explicit joint-length scale

Table A1. *Cont.*

Family	Criterion	Eq. No(s)	Test Basis	New Parameter(s) Introduced	Inputs Needed to Compute	Required Equipment/Measurements	Merits	Limitations
3D morphology-based (static peak)	Xia et al. [70]	(34)–(36)	3D roughness-based dilatancy function embedded in MC form	θ_{max}; θ*rms+; Cmax; A0; σ_t	σ_n; φ_b; morphology metrics; σ_t	3D scan + facet metrics; Brazilian tensile; φ_b from smooth shear	Reduces JRC subjectivity; directional 3D roughness	Many inputs; sensitive to scale/measurement
	Jang & Jang	(37)–(40)	3D dilatancy model with strength & roughness coupling	3D roughness function; degradation terms	σ_n; φ_b; 3D roughness metrics; strength parameters	3D scanning; UCS/σt; direct shear for calibration	Improves non-linear $\tau - \sigma_n$ fit	Parameter-rich; calibration dependence
	Kumar & Verma	(41)–(43)	3D morphological parameterization for peak strength	morphology factors; scaling terms	σ_n; φ_b; 3D roughness parameters	3D scanning and roughness computation; smooth-joint φ_b	Detailed 3D representation	High sensitivity to morphology inputs
	Zhang et al. (anisotropy)	(44) and (45)	3D roughness anisotropy captured via shear-direction facet statistics	θ^{*+}_{rms}; C_{max}; A_0	σ_n; φ_b; θ^{*+}_{rms}; Cmax; A_0	3D scan; compute shear-direction anisotropy metrics	Direction-dependent prediction (anisotropy)	Requires high-quality 3D data; processing burden
	Tang & Wong (mismatch, JCC)	(51) and (52)	Explicit mismatch/contact correction in 3D criteria	JCC (contact coefficient)	σ_n; base 3D criterion inputs; JCC	3D scan of both halves; contact/matching analysis to get JCC	Addresses imperfect matching	JCC estimation & contact modelling uncertainty
	Tang et al. (hyperbolic envelope)	(53) and (54)	Hyperbolic τ–σn envelope fitted to test data	hyperbolic parameters → equivalent c, φ	σ_n; fitted parameters (or back-calculated c, φ)	Direct shear tests over σ_n range for fitting	Smooth non-linear envelope; easy fitting	Purely empirical; extrapolation risk

Table A1. *Cont.*

Family	Criterion	Eq. No(s)	Test Basis	New Parameter(s) Introduced	Inputs Needed to Compute	Required Equipment/Measurements	Merits	Limitations
3D morphology-based (static peak)	Ding & Li (dilation-evolution based 3D criterion)	(55)	Calibrated against laboratory direct shear on rough joints	stress-dependent dilation evolution terms	σ_n; φ_b; 3D roughness metrics; dilation-evolution parameters	Direct shear + dilation measurement; 3D scan; calibration	Bridges 3D morphology with degradation concepts	Scale/resolution effects not fully explicit
	Azinfar et al. (scale-dependent 3D MC)	(56)	Replica joints; multiple specimen sizes; 3D scans	composite roughness-scale function; L/l	σ_n; φ_b; θ*; RMS; CLA; σ_t; L; l	3D scan; Brazilian tensile; measure L and l; direct shear for calibration	Explicit scale + resolution; keeps MC form	Limited calibration dataset; needs broader validation
	Hong et al. (multi-scale wavelet)	(70)	Granite joints; 3 sizes; wavelet decomposition + direct shear	first-/second-order roughness parameters (wavelet-based)	σ_n; φ_b; decomposed roughness metrics; L; l; strength params	Optical/laser topography; wavelet processing; UCS/σ_t; direct shear	Separates waviness vs. unevenness across scales	Method complexity; needs high-quality surface data
Transitional stress/degradation	Li et al. (transitional-stress controlled Saeb	(63)–(66)	Mechanistic continuous transition from dilative to sliding regime	σ_c (transitional normal stress); smooth transition functions	σ_n; φ_b; cohesion/strength terms; initial asperity angle; σ_T	Tilt/smooth shear for φ_b; UCS/point-load for strength; 3D scan for asperity angle; limited calibration for σ_T	Continuous (no abrupt break); parameters largely measurable without rough-joint shear	Assumes single effective roughness scale & unique σT; environment not explicit
	Zheng et al. (rate + size Barton-type)	(50)	Direct shear under different shear rates & specimen sizes	rate exponent; size-adjusted JRC/JCS	σ_n; rate; size; modified JRC/JCS; φ_r	Servo-controlled shear apparatus (rate control); roughness & strength tests	Captures rate and size dependence	More parameters; needs broad calibration
	Wang et al. (environmental factors)	(61)	Empirical modification for moisture/temperature effects	environment factors (e.g., water content/temperature terms)	σ_n; roughness/strength terms; environmental state variables	Environmental control (humidity/temperature); shear tests; roughness/strength tests	Introduces environment sensitivity	Context-specific; limited generality
	Zhang et al. (dynamic normal load)	(46)	Seismic/vibratory conditions; variable load amplitude & frequency	load amplitude; frequency	σ_n(t); amplitude; frequency; roughness/strength terms	Dynamic/cyclic shear loading system; instrumentation for σ_n (t)	Targets vibratory/seismic relevance	Validation breadth needed; complex implementation

Table A1. *Cont.*

Family	Criterion	Eq. No(s)	Test Basis	New Parameter(s) Introduced	Inputs Needed to Compute	Required Equipment/Measurements	Merits	Limitations
Wall-strength contrast (DDJCS/DDJS)	Ghazvinian et al. (DDJCS; dilation law + Patton)	(57) and (58)	CNL shear on sawtooth DDJCS interfaces (hard–soft/concrete–mortar)	σ_c (soft); stress-normalised dilation function	σ_n; φ_b (soft); asperity angle; σ_c (soft); fitted a,b (and irregularity)	Direct shear (CNL); *UCS* of soft wall; geometry (i); calibration data	Physically motivated normalisation by weaker wall	Needs regression parameters; specific to DDJCS setup
	Ghazvinian et al. (DDJCS; tensile-normalised)	(59)	DDJCS tests + PFC3D insight (tensile cracking dominant)	σ_T (soft) normalisation; roughness coefficient	σ_n; σ_T (soft); fitted roughness coefficient	Brazilian tensile on soft wall; direct shear database for fitting	Better when tensile cracking governs asperity failure	Still empirical fitting; applicability boundaries
	Tang et al. (DDJS with JSC)	(60)	Matched 3D geometry replicas with different wall strengths; CNL shear	JSC (strength difference coefficient)	σ_n; σ_T (weaker); 3D roughness metric; JSC	3D scanning; tensile/UCS of both walls; direct shear CNL; matching control	Explicitly treats wall-strength contrast in 3D	Complex inputs; requires matched-geometry specimens
Data-driven/ML	Fathipour-Azar et al. (MARS)	(68) and (69)	Data-driven fit (hinge functions) to lab/ compiled datasets	hinge knots; fitted coefficients	Predictor set used in model (e.g., σ_n, *JRC*/*JCS* or morphology)	Training dataset; computational fitting; measurement of predictors	Flexible non-linear regression; interpretable basis functions	Data-hungry; extrapolation uncertainty
	GA–BPNN hybrid ANN	(70)	ML trained on experimental data; GA optimises weights/ initialisation	network weights/biases; GA operators	Chosen predictor features (roughness, σ_n, strength, etc.)	Dataset + compute; feature measurement (scan/tests)	High predictive power; handles complex interactions	Black-box tendency; requires large/high-quality data

References

1. Jaeger, J.C.; Cook, N.G.W.; Zimmerman, R.W. *Fundamentals of Rock Mechanics*; Blackwell: Malden, MA, USA, 2007.
2. Wyllie, D.C.; Mah, C. *Rock Slope Engineering*; CRC Press: Boca Raton, FL, USA, 2004.
3. Barton, N.; Bandis, S. Effects of block size on the shear behavior of jointed rock. In *ARMA US Rock Mechanics/Geomechanics Symposium*; ARMA-82; ARMA: Westminster, CO, USA, 1982.
4. Goodman, R.E. Block theory and its application. *Geotechnique* **1995**, *45*, 383–423. [CrossRef]
5. Bandis, S.; Lumsden, A.C.; Barton, N.R. Experimental studies of scale effects on the shear behaviour of rock joints. *Int. J. Rock Mech. Min. Sci. Geomech. Abstr.* **1981**, *18*, 1–21. [CrossRef]
6. Bahaaddini, M.; Hagan, P.C.; Mitra, R.; Hebblewhite, B.K. Scale effect on the shear behaviour of rock joints based on a numerical study. *Eng. Geol.* **2014**, *181*, 212–223. [CrossRef]
7. Barton, N.; Choubey, V. The shear strength of rock joints in theory and practice. *Rock Mech.* **1977**, *10*, 1–54. [CrossRef]
8. Barton, N.; Bandis, S.; Bakhtar, K. Strength, deformation and conductivity coupling of rock joints. *Int. J. Rock Mech. Min. Sci. Geomech. Abstr.* **1985**, *22*, 121–140. [CrossRef]
9. Tse, R.; Cruden, D.M. Estimating joint roughness coefficients. *Int. J. Rock Mech. Min. Sci. Geomech. Abstr.* **1979**, *16*, 303–307. [CrossRef]
10. Tatone, B.S.A.; Grasselli, G. A method to evaluate the three-dimensional roughness of fracture surfaces in brittle geomaterials. *Rev. Sci. Instrum.* **2009**, *80*, 125110. [CrossRef] [PubMed]
11. Grasselli, G. Shear Strength of Rock Joints Based on Quantified Surface Description. Ph.D. Thesis, École Polytechnique Fédérale de Lausanne (EPFL), Lausanne, Switzerland, 2001.
12. Li, Y.; Tang, C.; Li, D.; Wu, C. A new shear strength criterion of three-dimensional rock joints. *Rock Mech. Rock Eng.* **2020**, *53*, 1477–1483. [CrossRef]
13. Tang, Z.C.; Wong, L.N.Y. New criterion for evaluating the peak shear strength of rock joints under different contact states. *Rock Mech. Rock Eng.* **2016**, *49*, 1191–1199. [CrossRef]
14. Azinfar, M.J.; Ghazvinian, A.; Fatemi, S.A. A new peak shear strength criterion of three-dimensional rock joints considering the scale effects. *Arab. J. Geosci.* **2021**, *14*, 936. [CrossRef]
15. Zhai, T.; Zhu, J.; Zhou, C.; Yang, T. Experimental investigation of the effect of thermal treatment on shear characteristics of healed rock joints. *Int. J. Rock Mech. Min. Sci.* **2022**, *152*, 105074. [CrossRef]
16. Yin, X.; Zhou, T.; Zhou, C.; Xie, H.; Zhu, J. Rate- and Normal Stress-Dependent Mechanical Behavior of Rock Under Direct Shear Loading Based on a Bonded-Particle Model (BPM). *Rock Mech. Rock Eng.* **2023**, *56*, 7959–7979. [CrossRef]
17. Patton, F.D. Multiple modes of shear failure in rock. In *ISRM Congress*; ISRM-1CONGRESS; ISRM: Lisbon, Portugal, 1966.
18. Ladanyi, B.; Archambault, G. Simulation Of Shear Behavior Of A Jointed Rock Mass. In Proceedings of the 11th Symposium on Rock Mechanics, Berkeley, CA, USA, 16–19 June 1969; Volume 1.
19. Ladanyi, B.; Archambault, G. *Shear Strength and Deformability of Filled Indented Joints*; École Polytechnique de Montréal: Montréal, QC, Canada, 1975. Available online: https://publications.polymtl.ca/6079/ (accessed on 29 September 2026).
20. Zhang, Q.; Gu, Q.; Li, S.; Wang, H.; Han, G. A shear strength criterion of rock joints under dynamic normal load. *Int. J. Rock Mech. Min. Sci.* **2025**, *186*, 106002. [CrossRef]
21. Barton, N. Shear strength criteria for rock, rock joints, rockfill and rock masses: Problems and some solutions. *J. Rock Mech. Geotech. Eng.* **2013**, *5*, 249–261. [CrossRef]
22. Hencher, S.R.; Richards, L.R. Assessing the Shear Strength of Rock Discontinuities at Laboratory and Field Scales. *Rock Mech. Rock Eng.* **2015**, *48*, 883–905. [CrossRef]
23. Thirukumaran, S.; Indraratna, B. A review of shear strength models for rock joints subjected to constant normal stiffness. *J. Rock Mech. Geotech. Eng.* **2016**, *8*, 405–414. [CrossRef]
24. Tang, Z.C.; Jiao, Y.Y.; Wong, L.N.Y.; Wang, X.C. Choosing appropriate parameters for developing empirical shear strength criterion of rock joint: Review and new insights. *Rock Mech. Rock Eng.* **2016**, *49*, 4479–4490. [CrossRef]
25. Singh, H.K.; Basu, A. Evaluation of existing criteria in estimating shear strength of natural rock discontinuities. *Eng. Geol.* **2018**, *232*, 171–181. [CrossRef]
26. Behnia, M.; Nateghpour, B.; Tavakoli, J.; Sharifi Broujerdi, M. Comparison of experimental and empirical methods for estimating the shear strength of rock joints based on the statistical approach. *Environ. Earth Sci.* **2020**, *79*, 361. [CrossRef]
27. Magsipoc, E.; Zhao, Q.; Grasselli, G. 2D and 3D Roughness Characterization. *Rock Mech. Rock Eng.* **2020**, *53*, 1495–1519. [CrossRef]
28. MacDonald, N.; Packulak, T.; Day, J. A Critical Review of Current States of Practice in Direct Shear Testing of Unfilled Rock Fractures Focused on Multi-Stage and Boundary Conditions. *Geosciences* **2023**, *13*, 172. [CrossRef]
29. Berisavljević, D.; Berisavljević, Z.; Melentijević, S. The shear strength evaluation of rough and infilled joints and its indications for stability of rock cutting in schist rock mass. *Bull. Eng. Geol. Environ.* **2022**, *81*, 113. [CrossRef]
30. Ge, Y.; Wen, Z.; Kulatilake, P.H.S.W.; Liu, G.; Tang, H. A Peak Shear Strength Criterion of Rock Joints Based on Brightness Area Percentage. *Int. J. Geomech.* **2025**, *25*, 04025097. [CrossRef]

31. Xie, S.; Li, J.; Wang, S.; Li, X. Experimental Study on Dynamic Shear Properties of Infilled Joints Under Dynamic Shearing: Insights from Normal Stress and Shear Rate. *Rock Mech. Rock Eng.* **2026**. [CrossRef]
32. Zoorabadi, M.; Muralha, J. Shear Strength of Rock Discontinuities with Emphasis on the Basic Friction Angle Based on a Compiled Database. *Geotechnics* **2025**, *5*, 48. [CrossRef]
33. Lei, D.; Zhang, Y.; Lu, Z.; Lin, H.; Chen, Y. Hybrid Machine Learning Model for Predicting Shear Strength of Rock Joints. *Appl. Sci.* **2025**, *15*, 7097. [CrossRef]
34. Liu, D.; Chen, S.; Lin, H.; Chen, Y. Shear Behavior and Morphological Evolution of Rough Rock Joints under Non-uniform Loading. *J. Mater. Eng. Perform.* **2025**. [CrossRef]
35. Verma, A.K.; Ahmad, F.; Jaiswal, A.; Sabri, M.S.; Singh, T.N. Interpretable Evolutionary Optimized XGBoost Framework for Predicting Shear Strength Parameters of Rock. *Transp. Infrastruct. Geotechnol.* **2026**, *13*, 98. [CrossRef]
36. Liang, G.; Huang, L.; Cao, C. Analysis and Prediction of Grouting Reinforcement Performance of Broken Rock Considering Joint Morphology Characteristics. *Mathematics* **2025**, *13*, 264. [CrossRef]
37. Renaud, S.; Saichi, T.; Bouaanani, N.; Miquel, B.; Quirion, M.; Rivard, P. Roughness Effects on the Shear Strength of Concrete and Rock Joints in Dams Based on Experimental Data. *Rock Mech. Rock Eng.* **2019**, *52*, 3867–3888. [CrossRef]
38. Ban, L.; Du, W.; Jin, T.; Qi, C.; Li, X. A roughness parameter considering joint material properties and peak shear strength model for rock joints. *Int. J. Min. Sci. Technol.* **2021**, *31*, 413–420. [CrossRef]
39. Ban, L.; Qi, C.; Chen, H.; Yan, F.; Ji, C. A New Criterion for Peak Shear Strength of Rock Joints with a 3D Roughness Parameter. *Rock Mech. Rock Eng.* **2020**, *53*, 1755–1775. [CrossRef]
40. Kulatilake, P.; Um, J. Requirements for accurate quantification of self-affine roughness using the roughness–length method. *Int. J. Rock Mech. Min. Sci.* **1999**, *36*, 5–18. [CrossRef]
41. Grasselli, G.; Egger, P. Constitutive law for the shear strength of rock joints based on three-dimensional surface parameters. *Int. J. Rock Mech. Min. Sci.* **2003**, *40*, 25–40. [CrossRef]
42. Belem, T.; Homand-Etienne, F.; Souley, M. Quantitative Parameters for Rock Joint Surface Roughness. *Rock Mech. Rock Eng.* **2000**, *33*, 217–242. [CrossRef]
43. Zhao, J. Joint surface matching and shear strength part B: JRC-JMC shear strength criterion. *Int. J. Rock Mech. Min. Sci.* **1997**, *34*, 179–185. [CrossRef]
44. Maerz, N.H.; Franklin, J.A. Roughness scale effect and fractal dimension. In Proceedings of the 1st International Workshop on Scale Effects in Rock Masses, Loen, Norway, 7–8 June 1990.
45. Oh, J.; Cording, E.J.; Moon, T. A joint shear model incorporating small-scale and large-scale irregularities. *Int. J. Rock Mech. Min. Sci.* **2015**, *76*, 78–87. [CrossRef]
46. Indraratna, B.; Premadasa, W.; Brown, E.T.; Gens, A.; Heitor, A. Shear strength of rock joints influenced by compacted infill. *Int. J. Rock Mech. Min. Sci.* **2014**, *70*, 296–307. [CrossRef]
47. Jahanian, H.; Sadaghiani, M.H. Experimental study on the shear strength of sandy clay infilled regular rough rock joints. *Rock Mech. Rock Eng.* **2015**, *48*, 907–922. [CrossRef]
48. Wang, Y.; Nguyen, N.H.T. The effects of rock-infill interfacial properties on the compressive damage behaviour of flawed rocks: Results from a DEM study. *Theor. Appl. Fract. Mech.* **2022**, *117*, 103166. [CrossRef]
49. Papaliangas, T.; Hencher, S.R.; Lumsden, A.C.; Manolopoulou, S. The effect of frictional fill thickness on the shear strength of rock discontinuities. *Int. J. Rock Mech. Min. Sci. Geomech. Abstr.* **1993**, *30*, 81–91. [CrossRef]
50. Ram, B.K.; Basu, A. Shear Behavior of Unfilled-Planar Quartzitic Rock Joints with Reference to Weathering Grade of Joint Surfaces. *Rock Mech. Rock Eng.* **2019**, *52*, 4113–4121. [CrossRef]
51. Hoek, E.; Brown, E.T. Practical estimates of rock mass strength. *Int. J. Rock Mech. Min. Sci.* **1997**, *34*, 1165–1186. [CrossRef]
52. Tuğrul, A.; Zarif, I.H. Correlation of mineralogical and textural characteristics with engineering properties of selected granitic rocks from Turkey. *Eng. Geol.* **1999**, *51*, 303–317. [CrossRef]
53. Abbas, N.; Li, K.; Fissha, Y.; Gebrehiwot, Z.; Ikeda, H.; Ali, M.; Toriya, H.; Adachi, T.; Kawamura, Y. Influence of chemical composition and discontinuities on energy transformation and rock mass behaviour: Insights into geological dynamic. *J. Eng.* **2024**, *2024*, e12388. [CrossRef]
54. Isrm, B.E. Committee on standardization of laboratory and field tests. Suggested methods for the quantitative description of discontinuities in rock masses. *Int. J. Rock Mech. Min. Sci. Geomech. Abstr.* **1978**, *15*, 319–368.
55. Beer, A.J.; Stead, D.; Coggan, J.S. Technical note estimation of the joint roughness coefficient (JRC) by visual comparison. *Rock Mech. Rock Eng.* **2002**, *35*, 65–74. [CrossRef]
56. Lee, Y.-H.; Carr, J.R.; Barr, D.J.; Haas, C.J. The fractal dimension as a measure of the roughness of rock discontinuity profiles. *Int. J. Rock Mech. Min. Sci. Geomech. Abstr.* **1990**, *27*, 453–464. [CrossRef]
57. Alameda-Hernández, P.; Jiménez-Perálvarez, J.; Palenzuela, J.A.; El Hamdouni, R.; Irigaray, C.; Cabrerizo, M.A.; Chacón, J. Improvement of the JRC calculation using different parameters obtained through a new survey method applied to rock discontinuities. *Rock Mech. Rock Eng.* **2014**, *47*, 2047–2060. [CrossRef]

58. Stigsson, M.; Mas Ivars, D. A novel conceptual approach to objectively determine JRC using fractal dimension and asperity distribution of mapped fracture traces. *Rock Mech. Rock Eng.* **2019**, *52*, 1041–1054. [CrossRef]
59. Myers, N.O. Characterization of surface roughness. *Wear* **1962**, *5*, 182–189. [CrossRef]
60. Wu, T.H.; Ali, E.M. Statistical representation of joint roughness. *Int. J. Rock Mech. Min. Sci. Geomech. Abstr.* **1978**, *15*, 259–262. [CrossRef]
61. Riss, J.; Gentier, S.; Archambault, G.; Flamand, R. Sheared rock joints: Dependence of damage zones on morphological anisotropy. *Int. J. Rock Mech. Min. Sci.* **1997**, *34*, 258.e1–258.e14. [CrossRef]
62. Marache, A.; Riss, J.; Gentier, S.; Chilès, J. Characterization and reconstruction of a rock fracture surface by geostatistics. *Int. J. Numer. Anal. Methods Geomech.* **2002**, *26*, 873–896. [CrossRef]
63. Sayles, R.S.; Thomas, T.R. The spatial representation of surface roughness by means of the structure function: A practical alternative to correlation. *Wear* **1977**, *42*, 263–276. [CrossRef]
64. Kulatilake, P.H.S.W.; Balasingam, P.; Park, J.; Morgan, R. Natural rock joint roughness quantification through fractal techniques. *Geotech. Geol. Eng.* **2006**, *24*, 1181–1202. [CrossRef]
65. Grasselli, G.; Wirth, J.; Egger, P. Quantitative three-dimensional description of a rough surface and parameter evolution with shearing. *Int. J. Rock Mech. Min. Sci.* **2002**, *39*, 789–800. [CrossRef]
66. Jiang, Y.; Tanabashi, Y.; Li, B.; Xiao, J. Influence of geometrical distribution of rock joints on deformational behavior of underground opening. *Tunn. Undergr. Space Technol.* **2006**, *21*, 485–491. [CrossRef]
67. Ban, L.; Zhu, C.; Qi, C.; Tao, Z. New roughness parameters for 3D roughness of rock joints. *Bull. Eng. Geol. Environ.* **2019**, *78*, 4505–4517. [CrossRef]
68. El-Soudani, S.M. Profilometric analysis of fractures. *Metallography* **1978**, *11*, 247–336. [CrossRef]
69. Tatone, B.S.A.; Grasselli, G. An Investigation of Discontinuity Roughness Scale Dependency Using High-Resolution Surface Measurements. *Rock Mech. Rock Eng.* **2013**, *46*, 657–681. [CrossRef]
70. Xia, C.-C.; Tang, Z.-C.; Xiao, W.-M.; Song, Y.-L. New Peak Shear Strength Criterion of Rock Joints Based on Quantified Surface Description. *Rock Mech. Rock Eng.* **2014**, *47*, 387–400. [CrossRef]
71. Homand, F.; Belem, T.; Souley, M. Friction and degradation of rock joint surfaces under shear loads. *Int. J. Numer. Anal. Methods Geomech.* **2001**, *25*, 973–999. [CrossRef]
72. Um, J.-G. Accurate Quantification of Rock Joint Roughness and Development of a New Peak Shear Strength Criterion for Joints. Ph.D. Thesis, University of Arizona, Tucson, AZ, USA, 1997.
73. Kulatilake, P.; Um, J.; Pan, G. Requirements for accurate estimation of fractal parameters for self-affine roughness profiles using the line scaling method. *Rock Mech. Rock Eng.* **1997**, *30*, 181–206. [CrossRef]
74. Oh, J.; Kim, G.-W. Effect of opening on the shear behavior of a rock joint. *Bull. Eng. Geol. Environ.* **2010**, *69*, 389–395. [CrossRef]
75. Hong, E.; Lee, J.; Lee, I. Underestimation of roughness in rough rock joints. *Int. J. Numer. Anal. Methods Geomech.* **2008**, *32*, 1385–1403. [CrossRef]
76. Wang, G.; Liu, W.; Jiang, F.; He, P.; Huang, N.; Xiao, Z.; Zheng, C. Shear damage mechanisms of jointed rock mass: A macroscopic and mesoscopic study. *Sci. Rep.* **2024**, *14*, 8619. [CrossRef] [PubMed]
77. Anttilainen, A. Scale-Effect in the Shear Strength of Fresh Fractures in Kuru Granite. Master's Thesis, Aalto University, Espoo, Finland, 2025.
78. Li, Y.; Oh, J.; Mitra, R.; Canbulat, I. A Fractal Model for the Shear Behaviour of Large-Scale Opened Rock Joints. *Rock Mech. Rock Eng.* **2017**, *50*, 67–79. [CrossRef]
79. Zhang, L.; Einstein, H.H. Estimating the intensity of rock discontinuities. *Int. J. Rock Mech. Min. Sci.* **2000**, *37*, 819–837. [CrossRef]
80. Borri-Brunetto, M.; Carpinteri, A.; Chiaia, B. The Effect of Scale and Criticality in Rock Slope Stability. *Rock Mech. Rock Eng.* **2004**, *37*, 117–126. [CrossRef]
81. Fardin, N.; Stephansson, O.; Jing, L. The scale dependence of rock joint surface roughness. *Int. J. Rock Mech. Min. Sci.* **2001**, *38*, 659–669. [CrossRef]
82. Lee, H.S.; Park, Y.J.; Cho, T.F.; You, K.H. Influence of asperity degradation on the mechanical behavior of rough rock joints under cyclic shear loading. *Int. J. Rock Mech. Min. Sci.* **2001**, *38*, 967–980. [CrossRef]
83. Mouzannar, H.; Bost, M.; Leroux, M.; Virely, D. Experimental Study of the Shear Strength of Bonded Concrete–Rock Interfaces: Surface Morphology and Scale Effect. *Rock Mech. Rock Eng.* **2017**, *50*, 2601–2625. [CrossRef]
84. Witherspoon, P.A.; Wang, J.S.Y.; Iwai, K.; Gale, J.E. Validity of cubic law for fluid flow in a deformable rock fracture. *Water Resour. Res.* **1980**, *16*, 1016–1024. [CrossRef]
85. Goodman, R.E. *Introduction to Rock Mechanics*; John Wiley & Sons: Hoboken, NJ, USA, 1991.
86. Archambault, G.; Poirier, S.; Rouleau, A.; Gentier, S.; Riss, J. Pore Pressure Behavior In Undrained Triaxial Shear Tests On Joints. In *Proceedings of the 9th ISRM Congress, Paris, France, 25–28 August 1999*; ISRM-9CONGRESS-1999-151; ISRM: Lisbon, Portugal, 1999.
87. El Fil, H. Shear Response of Rock Discontinuities: Through the Lens of Geophysics. Ph.D. Thesis, Purdue University, West Lafayette, IN, USA, 2021.

88. Karakas, A. Practical rock engineering. *Environ. Eng. Geosci.* **2008**, *14*, 55–57. [CrossRef]
89. Indraratna, B.; Haque, A. *Shear Behaviour of Rock Joints*; A.A. Balkema: Rotterdam, The Netherlands, 2000.
90. Zhang, Z.-X. Chapter 3—Rock Fracture and Rock Strength. In *Rock Fracture and Blasting: Theory and Applications*; Butterworth-Heinemann: Oxford, UK, 2016; pp. 69–88. [CrossRef]
91. Skinas, C.A.; Bandis, S.C.; Demiris, C.A. Experimental investigations and modelling of rock joint behaviour under constant stiffness. In *International Symposium on Rock Joints*; Taylor & Francis: Abingdon, UK, 1990; pp. 301–308.
92. Indraratna, B.; Haque, A.; Aziz, N. Shear behaviour of idealized infilled joints under constant normal stiffness. *Geotechnique* **1999**, *49*, 331–355. [CrossRef]
93. Fathi, A.; Moradian, Z.; Rivard, P.; Ballivy, G.; Boyd, A.J. Geometric effect of asperities on shear mechanism of rock joints. *Rock Mech. Rock Eng.* **2016**, *49*, 801–820. [CrossRef]
94. Hoek, E. *Practical Rock Engineering—Chapter 11: Rock Mass Properties*; Rocscience: North Vancouver, BC, Canada, 2007.
95. Wyllie, D.C.; Norrish, N.I. Rock Strength Properties Amd Their Measurement. In *Landslides: Investigation and Mitigation*; Turner, A.K., Schuster, R.L., Eds.; Transportation Research Board, National Research Council: Washington, DC, USA, 1996; pp. 372–390.
96. Mohr, C.O. *Abhandlungen aus dem Gebiete der Technischen Mechanik*; Wilhelm Ernst & Sohn: Berlin, Germany, 1914.
97. Mohr, C.O. Über die Darstellung des Spannungszustandes und des Deformationszustandes eines Körperelementes und über die Anwendung derselben in der Festigkeitslehre. *Der Civil.* **1882**, *28*, 113–156.
98. Coulomb, C.A. Essai sur une application des regles de maximis et minimis a quelques problemes de statique relatifs a l'architecture. *Mem. Math. Phys. R. Acad. Sci.* **1776**, *7*, 343–387.
99. Newland, P.L.; Allely, B.H. Volume changes in drained taixial tests on granular materials. *Geotechnique* **1957**, *7*, 17–34. [CrossRef]
100. Schneider, H.J. The friction and deformation behaviour of rock joints. *Rock Mech.* **1976**, *8*, 169–184. [CrossRef]
101. Barton, N. The shear strength of rock and rock joints. *Int. J. Rock Mech. Min. Sci. Geomech. Abstr.* **1976**, *13*, 255–279. [CrossRef]
102. Kulatilake, P.H.S.W.; Shou, G.; Huang, T.H.; Morgan, R.M. New peak shear strength criteria for anisotropic rock joints. *Int. J. Rock Mech. Min. Sci. Geomech. Abstr.* **1995**, *32*, 673–697. [CrossRef]
103. Ghazvinian, A.H.; Taghichian, A.; Hashemi, M.; Mar'ashi, S.A. The Shear Behavior of Bedding Planes of Weakness Between Two Different Rock Types with High Strength Difference. *Rock Mech. Rock Eng.* **2010**, *43*, 69–87. [CrossRef]
104. Asadollahi, P.; Tonon, F. Constitutive model for rock fractures: Revisiting Barton's empirical model. *Eng. Geol.* **2010**, *113*, 11–32. [CrossRef]
105. Plesha, M.E. Constitutive models for rock discontinuities with dilatancy and surface degradation. *Int. J. Numer. Anal. Methods Geomech.* **1987**, *11*, 345–362. [CrossRef]
106. Cundall, P.A.; Hart, R.D. *Development of Generalized 2-D and 3-D Distinct Element Programs for Modeling Jointed Rock*; U.S. Army Engineer Waterways Experiment Station: Vicksburg, MS, USA, 1985.
107. Cottrell, B. Updates to the GG-Shear Strength Criterion. Master of Engineering Thesis, University of Toronto at Toronto, Toronto, ON, Canada, 2009.
108. Tang, H.; Ge, Y.; Wang, L.; Yuan, Y.; Huang, L.; Sun, M. Study on estimation method of rock mass discontinuity shear strength based on three-dimensional laser scanning and image technique. *J. Earth Sci.* **2012**, *23*, 908–913. [CrossRef]
109. Jang, H.-S.; Jang, B.-A. New Method for Shear Strength Determination of Unfilled, Unweathered Rock Joint. *Rock Mech. Rock Eng.* **2015**, *48*, 1515–1534. [CrossRef]
110. Kumar, R.; Verma, A.K. Anisotropic shear behavior of rock joint replicas. *Int. J. Rock Mech. Min. Sci.* **2016**, *90*, 62–73. [CrossRef]
111. Zhang, X.; Jiang, Q.; Chen, N.; Wei, W.; Feng, X. Laboratory Investigation on Shear Behavior of Rock Joints and a New Peak Shear Strength Criterion. *Rock Mech. Rock Eng.* **2016**, *49*, 3495–3512. [CrossRef]
112. Jing, L.; Nordlund, E.; Stephansson, O. An experimental study on the anisotropy and stress-dependency of the strength and deformability of rock joints. *Int. J. Rock Mech. Min. Sci. Geomech. Abstr.* **1992**, *29*, 535–542. [CrossRef]
113. Zheng, B.; Qi, S.; Huang, X.; Guo, S.; Wang, C.; Zhan, Z.; Luo, G. An Advanced Shear Strength Criterion for Rock Discontinuities Considering Size and Low Shear Rate. *Appl. Sci.* **2020**, *10*, 4095. [CrossRef]
114. Ding, L.; Li, G. Research on Peak Shear Strength Criterion of Rock Joints Based on the Evolution of Dilation Angle. *Geotech. Geol. Eng.* **2021**, *39*, 4887–4900. [CrossRef]
115. Ghazvinian, A.H.; Azinfar, M.J.; Geranmayeh Vaneghi, R. Importance of tensile strength on the shear behavior of discontinuities. *Rock Mech. Rock Eng.* **2012**, *45*, 349–359. [CrossRef]
116. Tang, Z.; Zhang, Z.; Jiao, Y.Y. Three-dimensional Criterion for Predicting Peak Shear Strength of Matched Discontinuities with Different Joint Wall Strengths. *Rock Mech. Rock Eng.* **2021**, *54*, 3291–3307. [CrossRef]
117. Gui, Y.; Xia, C.; Ding, W.; Qian, X.; Du, S. Modelling Shear Behaviour of Joint Based on Joint Surface Degradation During Shearing. *Rock Mech. Rock Eng.* **2019**, *52*, 107–131. [CrossRef]
118. He, L.; Zhao, Z.; Chen, J.; Liu, D. Empirical Shear Strength Criterion for Rock Joints Based on Joint Surface Degradation Characteristics During Shearing. *Rock Mech. Rock Eng.* **2020**, *53*, 3609–3624. [CrossRef]

119. Yu, H.; Taleghani, A.D.; Balushi, F.A.l.; Wang, H. Machine learning for rock mechanics problems; an insight. *Front. Mech. Eng.* **2022**, *8*, 1003170. [CrossRef]
120. Fathipour-Azar, H. New interpretable shear strength criterion for rock joints. *Acta Geotech.* **2022**, *17*, 1327–1341. [CrossRef]
121. Zhu, C.; Guo, B.; Zhang, Z.; Zhong, P.; Lu, H.; Sigama, A. Determining Rock Joint Peak Shear Strength Based on GA-BP Neural Network Method. *Appl. Sci.* **2024**, *14*, 9566. [CrossRef]
122. Montana, D.J.; Davis, L. Training feedforward neural networks using genetic algorithms. *IJCAI* **1989**, *89*, 762–767.
123. Huang, J.; Zhang, J.; Gao, Y. Intelligently Predict the Rock Joint Shear Strength Using the Support Vector Regression and Firefly Algorithm. *Lithosphere* **2021**, *2021*, 2467126. [CrossRef]
124. Zhang, Z.; Guo, B.; Zhu, C.; Zhong, P.; Rong, T. Experimental study on shear mechanical characteristics and its size effect of concrete joints based on BP neural network method. *Constr. Build. Mater.* **2024**, *442*, 137583. [CrossRef]
125. Hong, C.; Tao, Z.; Yang, S.; Wang, K.; Weng, H.; Huang, M. New peak shear strength criterion of rock joints based on two-order roughness. *J. Mt. Sci.* **2025**, *22*, 1859–1870. [CrossRef]
126. Muralha, J.; Grasselli, G.; Tatone, B.; Blümel, M.; Chryssanthakis, P.; Yujing, J. ISRM suggested method for laboratory determination of the shear strength of rock joints: Revised version. *Rock Mech. Rock Eng.* **2014**, *47*, 291–302. [CrossRef]
127. Dong, S.; Peng, Y.; Lu, Z.; Zhang, H.; Hou, W.; Su, A. Shear characteristics and shear strength model of rock mass structural planes. *Sci. Rep.* **2022**, *12*, 13637. [CrossRef] [PubMed]
128. Hackston, A.; Rutter, E. The Mohr-Coulomb criterion for intact rock strength and friction—A re-evaluation and consideration of failure under polyaxial stresses. *Solid Earth* **2016**, *7*, 493–508. [CrossRef]
129. Hoek, E. Strength of jointed rock masses. *Geotechnique* **1983**, *33*, 187–223. [CrossRef]
130. Barton, N. Review of a new shear-strength criterion for rock joints. *Eng. Geol.* **1973**, *7*, 287–332. [CrossRef]
131. Corkum, A.G.; Jeans, B.; Ivars, D.M. Leeb hardness test as a tool for joint wall compressive strength (JCS) evaluation. *Eng. Geol.* **2025**, *344*, 107851. [CrossRef]
132. An, P.; Fang, K.; Jiang, Q.; Zhang, H.; Zhang, Y. Measurement of rock joint surfaces by using smartphone structure from motion (SfM) photogrammetry. *Sensors* **2021**, *21*, 922. [CrossRef] [PubMed]

Disclaimer/Publisher's Note: The statements, opinions and data contained in all publications are solely those of the individual author(s) and contributor(s) and not of MDPI and/or the editor(s). MDPI and/or the editor(s) disclaim responsibility for any injury to people or property resulting from any ideas, methods, instructions or products referred to in the content.